**Gaining Insight into Electron Capture Dissociation Mass Spectrometry
of Peptides and Proteins**

Natalie J. Thompson

A dissertation submitted to the faculty of the University of North Carolina at Chapel Hill in
partial fulfillment of the requirements for the degree of Doctor of Philosophy in the
Department of Chemistry.

Chapel Hill

2010

Approved by:

Advisor: Professor Gary L. Glish

Professor Nikolay Dokholyan

Professor James Jorgenson

Professor Gary Pielak

Professor Mark Wightman

Abstract

Natalie J. Thompson

Gaining Insight into Electron Capture Dissociation Mass Spectrometry
of Peptides and Proteins
(Under the direction of Gary L. Glish)

The study of protein structure is crucial to the understanding of protein function as the

two are inter-dependent. Protein structure analysis is especially important as misfolded

proteins often result in fatal diseases. Gas-phase protein structure analysis provides a way to

study the forces the effects of solvent and involved in the determination of protein structure.

Mass spectrometry (MS) is a rapid and sensitive technique that can be used for the analysis

of gas-phase protein structure.

Electron capture dissociation (ECD) tandem mass spectrometry (MS/MS) has been

used in the analysis of primary, secondary, and tertiary gas-phase protein structure.

ECD-MS/MS has proved to be exceptionally applicable in the study of protein structure due

to the ability to cleave protein backbone bonds with the retention of noncovalent interactions

and small-molecule post-translational modifications. The work described in this dissertation

expands the use ECD and other electron capture techniques for protein structure analysis.

All of the experiments were performed using a unique and versatile hybrid linear ion

trap / time-of-flight (LIT/TOF) mass spectrometer capable of multiple ion activation

techniques, such as collision induced dissociation (CID), infrared multiphoton dissociation

(IRMPD), ECD, hot ECD (HECD), and activated-ion ECD (AI-ECD). IR activation in

conjunction with ECD (AI-ECD) to disrupt noncovalent interactions was used to enhance

primary structure analysis and monitor changes in tertiary structure via gas-phase protein unfolding. The structure of the z$^{\bullet}$-type product ions was probed using ion-molecule reactions, and the formation different structures was found to depend on the electron capture technique used to dissociate the parent ion.

The work described in this dissertation demonstrates the use of AI-ECD for analysis of gas-phase protein structure. Also, the first analysis of z$^{\bullet}$-ion structure from various electron capture techniques is presented. This work highlights the versatility and utility of the LIT-TOF for ECD-MS/MS as an alternative to the commercial Fourier transform ion cyclotron resonance (FTICR) mass spectrometers.

Acknowledgements

I would like to thank my parents for their unwavering support over the years. They provided a solid foundation in science and instilled in me a permanent sense of curiosity. Mom, thank you for continually giving me a sense of reality and reminding me that strength comes from within. Dad, thank you for letting me talk science with you and telling me that there is always another way to get that measurement.

I would like to thank Dr. Gary L. Glish for teaching me to be confident in my research and how to approach my research critically. I would also like to thank you for giving me a multitude of opportunities in scientific research and professional development.

I would like to thank Dr. Takashi Baba for unending patience and inexhaustible knowledge in teaching me.

I would like to thank the Glish group for sharing the lighter side of life with me through graduate school. Your friendship has made the tough times better and the good times great.

Table of Contents

List of Figures

List of Abbreviations and Symbols

^{13}C	carbon-13
A	alanine
A	ampere
A	area
A^-	reagent anion
ac	alternating current
Ag	silver
AI-ECD	activated-ion electron capture dissociation
Au	gold
BaF_2	barium fluoride
C	carbon
C	conductance
C_α	alpha carbon of polypeptide backbone
C(O)	carbonyl carbon of polypeptide backbone
CID	collision induced dissociation
cm	centimeter (1×10^{-2} m)
CO_2	carbon dioxide
°C	degree Celsius
D_2O	deuterated water
Da	dalton
dc	direct current
e^-	electron

ECD	electron capture dissociation
ECD$_{hi}$	electron capture dissociation at increased electron flux
ECD$_{LIT}$	linear ion trap in the NanoFrontier mass spectrometer where ECD is performed
ECD/IR	sequential AI-ECD; IR activation after ECD
ESI	electrospray ionization
ESI-MS	electrospray ionization mass spectrometry
ETD	electron transfer dissociation
eV	electron volt
f.l.	focal length
FAIMS	high field asymmetric ion mobility spectrometry
FTICR	Fourier transform ion cyclotron resonance
H	histidine
H/D	hydrogen-deuterium
HDX	hydrogen-deuterium exchange
HECD	hot electron capture dissociation
HXMS	hydrogen-deuterium exchange mass spectrometry
ICR	ion cyclotron resonance
IgG	immunoglobulin G
IMS	ion mobility spectrometry
IR	infrared
IR/ECD	sequential AI-ECD; IR activation prior to ECD
IRMPD	infrared multiphoton dissociation
K	lysine

kDa	kilodalton
LIT	linear ion rap
LIT_{CID}	linear ion trap in the NanoFrontier mass spectrometer in which parent ion isolation and accumulation occurs
LIT_{therm}	linear ion trap in the NanoFrontier mass spectrometer in which ions are stored prior to mass analysis by TOF
LIT-TOF	linear ion trap / time-of-flight
$[M+nH]^{n+}$	multiply charged parent ion
$[M+nH]^{(n-1)+\bullet}$	charge-reduced species of multiply charged parent ion
$[M*+nH]^{(n-1)+\bullet}$	vibrationally excited charge-reduced species of multiply charged parent ion
μm	micrometer (1×10^{-6} m)
μM	micromolar (1×10^{-6} M)
M	reactant in ion-molecule reaction to absorb excess energy
m	mass
MALDI	matrix-assisted laser desorption ionization
mbar	millibar
MCP	multi-channel plate
min	minute
mm	millimeter (1×10^{-3} m)
M_p^{n+}	parent ion
mRNA	messenger ribonucleic acid
ms	millisecond (1×10^{-3} s)
MS/MS	tandem mass spectrometry
mT	millitesla

N	nitrogen
nESI	nanoelectrospray ionization
ND_3	deuterated ammonia
NMR	nuclear magnetic resonance
O	oxygen
O_2	molecular oxygen
OCN	polypeptide backbone amide
P	pressure
P_1^{m+}, $P_2^{(n-m)+}$	product ions
ps	picosecond (1×10^{-12} s)
Q	mass flow rate
R	arginine
$R^{\bullet}$	alkyl radical
rf	radio frequency
$RO_2^{\bullet}$	alkylperoxy radical
S/N	signal-to-noise ratio
S-S	disulfide
sccm	standard cubic centimeters per minutes
$[subP]^{2+}$	+2 charge state ion of substance P
T	temperature
T	tesla
TOF	time-of-flight
TTL	transistor-transistor logic

Ub	ubiquitin
V	volt
v/v	volume-to-volume ratio
W	watt
Y	tyrosine
ZnSe	zinc selenide

Chapter 1

Introduction to Protein Analysis by Mass Spectrometry

1.1 Protein structure

The study of protein structure is essential because the three-dimensional structure determines the function of the protein in the cell. The sequence of amino acids, as determined by the cell genome, is unique for each protein and thus results in a unique structure for each protein. Out of the multitude of structures possible due to protein backbone flexibility, a single active conformation is formed, called the native state. The native state of a protein is generally a compact, energetically favorable structure that is formed largely due to collapse of hydrophobic residues to the core of the protein.

Folding of the native state conformation is crucial to the protein function in the cell. Misfolding of the protein structure has been shown to lead to many kinds of diseases [2, 3]. For example, cystic fibrosis results from the misfolding of a transport protein as a result of a genetic mutation [2, 4]. Another example of the importance of protein structure is the formation of amyloid fibrils in diseases such as Alzheimer's and Creutzfeldt-Jakob diseases [5]. In these diseases, normally soluble proteins undergo a structural change that forms amyloid plaques and fibrils in the brain. These fibrils are extremely stable structures that are toxic to the cells [2]. These examples highlight the influence of protein structure on function and provide motivation for the study of protein structure and the forces that influence it.

1.1.1 Hierarchy of protein structure

Protein structure is classified into a hierarchy with four tiers. The primary structure refers to the sequence of amino acids that comprise the protein. The individual residues are bound together via condensation to form an amide bond called the peptide bond. The protein backbone is a polymer composed of three types of covalent bonds: the N-C_α amine, C_α-C(O), and C(O)-N amide bonds (Figure 1.1). The flexibility of the protein backbone allows for many conformations to be adopted.

Figure 1.1 General schematic of protein backbone covalent bonds. There are three types of bonds: the N-C_α amine bond, the C_α-C(O) bond, and the C(O)-N amide (peptide) bond.

The three-dimensional organization of amino acids close in sequence is classified as the secondary structure. Secondary structure can be divided into three categories: alpha-helix, beta-sheet, and random coil. The alpha-helix and beta-sheet are rigid structures compared to the random coil constrained by hydrogen bonding between the carbonyl oxygen and the amide hydrogen on the protein backbone. The alpha-helix is a cylindrical structure with the amino acid side-chains radiating out from the cylinder. The alpha-helix is stabilized by hydrogen bonds between the carbonyl oxygen of one amino acid with the amide hydrogen of the amino acid four residues away in sequence. The hydrogen bonding in an alpha-helix is aligned parallel to the central axis of the helix. Beta-sheets are comprised of multiple beta-strands that align in either a parallel, anti-parallel, or mixed orientation. Beta-strands are short, elongated sections of the protein backbone with the side-chains perpendicular to

the backbone. Hydrogen bonding between carbonyl oxygen on one strand and amide hydrogen on the other stabilize the beta-sheet. The directionality of the strands with respect to each other is classified as parallel (same backbone directionality) or anti-parallel (opposite backbone directionality). The arrangement of beta-strands creates a flexible pleated sheet with the hydrogen bonding parallel to the surface. Random coils consist of unstructured regions that give the protein structure much of its flexibility.

Tertiary structure describes the three-dimensional conformation of the protein. The interaction of secondary structure elements creates domains that can be classified by structure, e.g., a proline-rich domain, or by function, e.g., the binding domain of an enzyme. Tertiary structure is characterized by the interactions of amino acid residues that are distant in sequence. The forces involved in the determination of tertiary structure include hydrophobic interactions, disulfide linkages, hydrogen bonding, and electrostatic interactions between charge sites. The driving force for protein folding in solution is dominated by the hydrophobic interactions. The interaction between hydrophobic amino acid residues and a polar solvent, most often water, is entropically unfavorable. Therefore, most protein tertiary structure has a hydrophobic core that has very little interaction with the solvent. The surface is often comprised of charged groups that can be solvated by the polar environment. Disulfide linkages occur between the thiol groups of cysteine amino acid residues and are used to provide rigidity to the protein tertiary structure. While less influential on tertiary structure than hydrophobic interactions and disulfide bonds, hydrogen bonding and electrostatic interactions are also used to stabilize the tertiary structure in solution.

Finally, quaternary structure defines the interactions between multiple proteins in a macromolecular complex. As the study of protein structure continues, quaternary structure is

3

becoming more important because few proteins act as individuals. Instead, most proteins form multi-subunit complexes that perform complicated cell functions, such as the transcription of DNA to messenger RNA (mRNA). Quaternary structure uses hydrogen bonding and electrostatic interactions between subunits to aggregate and interact. It has been suggested that quaternary structure increases the stability of the involved proteins from destructive forces such as thermal denaturation [6]. Secondary, tertiary, and quaternary structures comprise the higher-order structure of a protein, as shown in Figure 1.2.
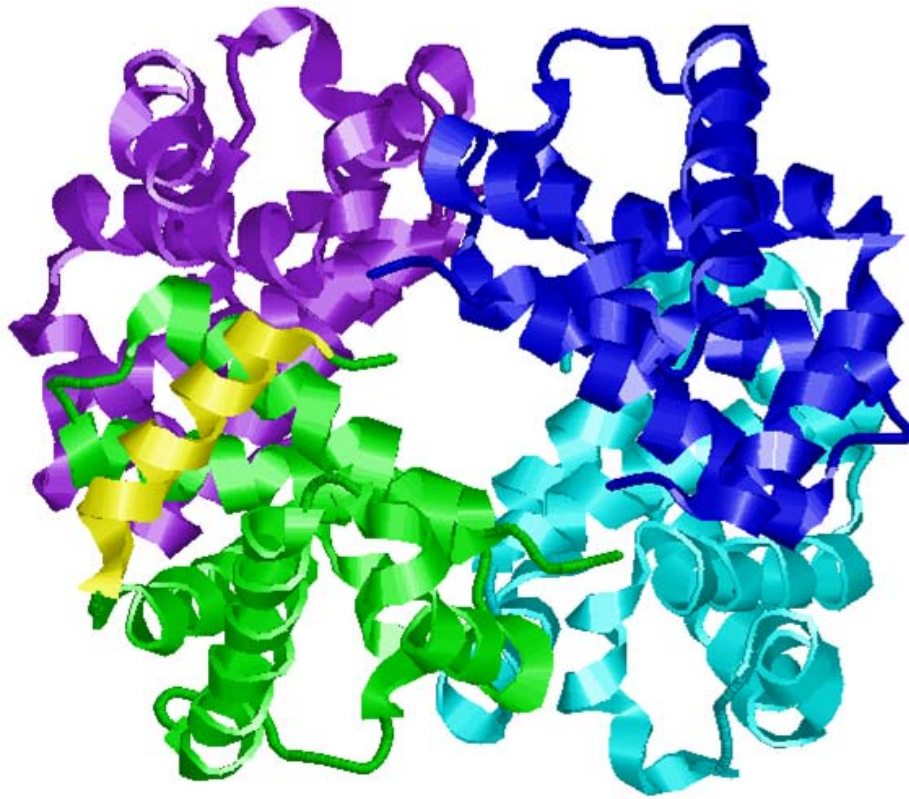
Figure 1.2 Cartoon representation of hemoglobin (PDB 1GZX) [1]. Hemoglobin contains four subunits (two α and two β) which are held together by the quaternary structure (interaction of green, cyan, blue, and purple). Each type of subunit has unique tertiary structure (green, cyan, blue, or purple) comprised mostly of alpha-helical secondary structure (yellow).

1.1.2 Gas-phase protein structure

Due to the difference in environment, gas-phase protein structure is often drastically different than solution-phase structure. In solution, the presence of a polar solvent results in efficient charge solvation and the collapse of hydrophobic regions. The hydrophobic collapse is not due to the van der Waals forces between the hydrophobic groups themselves but result from an entropic increase with the decreased interaction between hydrophobic groups and the polar solvent. The stability provided by charge solvation and hydrophobic interactions are absent in the gas-phase structure.

Due to the lack of solvent, vacuum can be considered a hydrophobic environment. It has been suggested that highly hydrophobic peptides, such as in melittin, have near-native conformations in the gas phase [7]. Due to the lack of charge solvation by polar solvent molecules, the importance of electrostatic interactions increases in the gas phase [8, 9]. The charge sites must now be stabilized within the molecule, as evident by the collapse of the charged side-chains upon desolvation [9, 10]. As a result of the increase in the force between electrostatic interactions in the gas phase, the distribution of charge sites along the protein backbone has great influence on the overall protein conformation. Coulombic repulsion between like charge sites is known to disrupt secondary structure and force elongation of the backbone to an extended gas-phase structure [11-13]. It has also been shown that due to the lack of strong stabilizing forces, such as hydrophobic interactions in solution, multiple protein conformations are observed in the gas phase [9, 11].

1.2 Mass spectrometry for protein analysis

There are a number of solution-phase methods for the structural analysis of proteins, such as nuclear magnetic resonance (NMR) spectroscopy and Edman degradation. Mass

spectrometry is a relatively recent but crucial addition to the protein scientist's tool box. Mass spectrometry provides high sensitivity, fast analysis times, and low limits of detection [14-16] and is especially appropriate for the analysis of proteins because of the capability to study large proteins and macromolecular complexes [6]. While mass spectrometry is not suited to study protein solution-phase structure because analysis is performed in the gas phase, the comparison between gas-phase and solution-phase structure can provide insight into the influence of water on structure [7].

1.2.1 Transfer of proteins to the gas phase

Mass spectrometric had limited utility in the analysis of proteins prior to the development of ionization techniques such as electrospray ionization (ESI) [17] and matrix-assisted laser desorption ionization (MALDI) [18]. ESI is referred to as a "soft" ionization technique in which analytes are transferred to the gas phase and ionized with little fragmentation. ESI was designed to sample molecules directly from solution making it amenable to common separation techniques such as liquid chromatography and capillary electrophoresis.

The transfer of large, nonvolatile molecules, like proteins, to the gas phase by ESI has been well studied [6, 10, 15, 19]. In ESI, a large potential on the order of two to four kilovolts is applied between a capillary containing the solution to be analyzed and the entrance to the mass spectrometer. The accumulation of charge at the surface of the solution due to the strong electric field produces a mist of small charged droplets. These droplets undergo evaporation through collisions with neutral gas molecules until the Rayleigh limit is reached. The Rayleigh limit occurs when the Coulombic repulsion in the charge is greater than the surface tension, and the droplet explodes into smaller droplets. The production of

bare gas-phase ions from these small droplets has been described by two models. In the ion evaporation model, small droplets release bare ions prior to removal of all the solvent by evaporation [20]. Small ions, such as salts, are generally formed by the ion evaporation model. Larger ions are proposed to form through the charge residue model [6, 20]. Solvent evaporation and droplet fission occur until a few solvent molecules remain. These last molecules evaporate leaving the excess charge from the droplet on the bare ion. The transfer of proteins and other large biomolecules to the gas phase is purported to occur by the charge residue model [6, 21].

The ability of ESI to transfer large noncovalent complexes to the gas phase [19] led to questions about the preservation of solution-phase structure in the gas phase. A model for the evolution of protein gas-phase structure from the final steps of ESI has recently been presented [10]. A study has shown that the last solvent molecules cluster around the charge sites thus transiently preserving solution-phase structure [22]. After the solvent molecules are fully evaporated, the charged side-chains collapse within approximately 10 ps, briefly stabilizing the solution-phase structure [10]. The change in environment results in the loss of hydrophobic interactions which results in the unfolding of the protein structure within milliseconds after side-chain collapse. Protein unfolding in the gas-phase is due to a reverse in the thermodynamic stability of the structure due to the removal of water [10]. Afterwards, the protein refolds into a stable gas-phase structure which is then studied using mass spectrometry.

ESI is especially useful for the analysis of proteins due to the formation of multiply charged ions. The addition of multiple charges reduces the mass-to-charge ratio of the protein into a range that is observable by common mass analyzers, such as the linear ion trap.

In the gas-phase structure, the basic sites are often protonated due to the increased proton affinity over other amino acid residues. Therefore, the maximum charge state observed for a protein ion is typically equal to the number of basic sites [21]. The charge state distribution of the protein ions are influenced by the solution-phase structure. More unfolded solution-phase structures results in higher charge state ions in the gas phase [20]. The correlation between protein solution-phase structure and the number of charges in the gas phase is attributed to the solvent accessibility of the basic residues during desolvation [6].

1.2.2 Tandem mass spectrometry in protein analysis

ESI-MS allows the analysis of large nonvolatile proteins but typically only provides the molecular mass of the protein. As the mass of a sample increases, the number of combinations of atoms that sum up to the total mass also increases thus making detailed analysis difficult. Tandem mass spectrometry (MS/MS) provides a way to study the connectivity of the atoms in proteins.

In a MS/MS experiment, an ion is isolated by the mass-to-charge ratio. The isolated ion, called the parent ion (M_p^{n+}), is activated to induce dissociation of the covalent bonds. The ions formed from the dissociation are called product ions (P_1^{m+}, $P_2^{(n-m)+}$) (Equation 1.1).

$$M_p^{n+} \rightarrow P_1^{m+} + P_2^{(n-m)+}$$ **Equation 1.1**
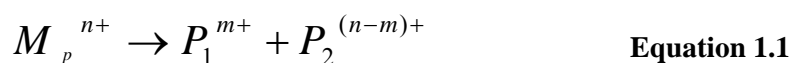
If the parent ion is singly charged, there will be one product ion and one neutral product. Multiple charging in the parent ion, as observed in ESI of proteins, results in the possibility of two charged product ions as a result of the distribution of charges in the parent ion.

Tandem mass spectrometry of proteins provides a wide variety of product ions. A common nomenclature was developed to describe the dissociation of the backbone in a generic manner without the reliance on adjacent amino acid side-chains [23] (Figure 1.3)
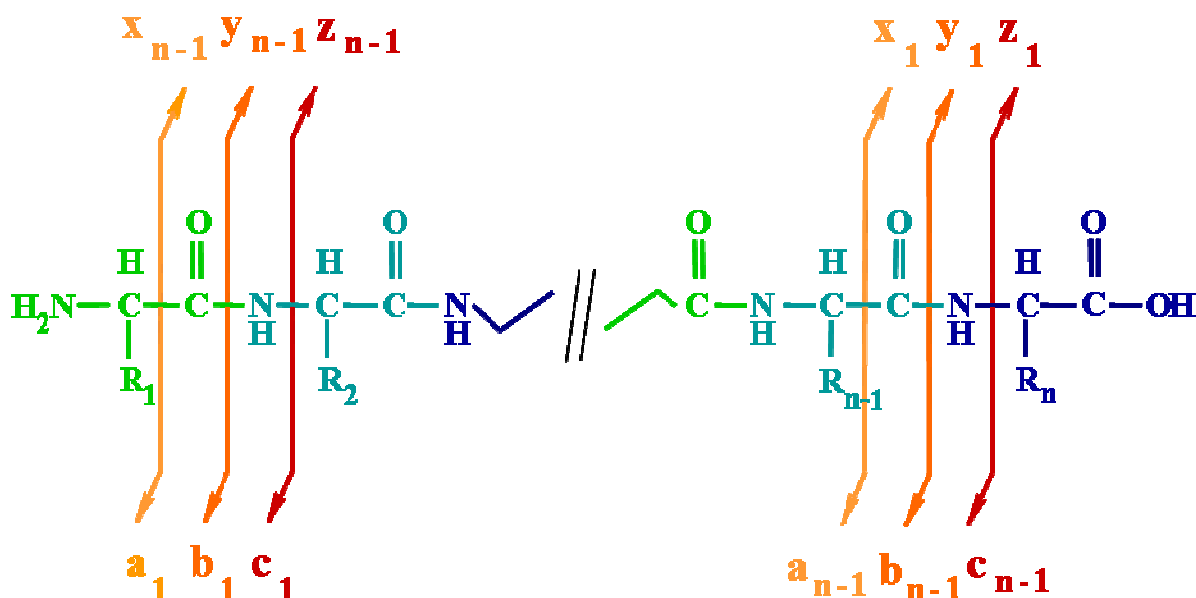
Figure 1.3 Generalized protein backbone showing protein product ion dissociation nomenclature. Product ions are classified by terminus, type of backbone bond broken, and number of residues in the product ion. The arrows represent the location of the charge after backbone dissociation.

With this nomenclature, the nature of the product ion, including the size and which type of

backbone bond was broken, is defined. Product ions are divided into three families

dependent on the type of backbone bond that is broken. For a peptide with k residues

cleavage of the C_α-C after the n-th residue leads to the formation of a_n- and x_{k-n}-ions;

cleavage of the peptide bond (C(O)-N) results in the formation of b_n- and y_{k-n}- ions; and

cleavage of the N-C_α aminebond forms c_n- and z_{k-n}-ions. The a-, b-, and c-type ions are

formed if charge is retained on the N-terminal product while the x-, y-, and z-ions are formed

if charge remains on the C-terminal product. For multiply charged proteins, both N- and C-

-terminal product ions are formed if that product ion contains a basic residue that can be

charged. Finally, the subscript number indicates the number of residues in the product ion.

Many MS/MS methods have been developed to study proteins, and each method is

typically distinguished by the method of parent ion activation and the types of product ions

formed. Multiple methods of tandem mass spectrometry are included in this dissertation and are described below.

1.2.2.1 Collision induced dissociation

Collision induced dissociation (CID) is used to describe the use of multiple low-energy collisions to increase ion internal energy which causes unimolecular dissociation. For CID in an ion trap, the ion is typically trapped in a high pressure environment (10^{-3} mbar). Activation is imparted through the acceleration of the ion using a resonant rf voltage specific to the mass-to-charge ratio of the parent ion. Ion acceleration results in increasingly energetic collisions between ions and bath gas molecules, and in these inelastic collisions, a fraction of the ion kinetic energy is converted to ion internal energy [24]. The increase in ion internal energy is then statistically redistributed throughout the vibrational modes of the parent ion [14] and results in a distribution of energies that resembles a Boltzmann distribution at elevated temperatures [24, 25]. Because CID uses multiple activation steps for ion dissociation, it is referred to as a "slow-heating" technique [24].

The increase in ion internal energy and subsequent redistribution of this energy leads to the dissociation of the weakest bonds [14]. In a protein, the weakest bonds are the noncovalent interactions followed by those that bind labile groups such as small-molecule post-translational modifications like phosphorylation. Therefore, the weak bonds are disrupted prior to backbone dissociation, resulting in a loss of higher-order structural information [26]. After noncovalent interactions and the bonds that hold labile groups, the weakest bonds in a protein are those between the protonated amide nitrogen and the carbonyl group, called the peptide bond. In solution structure, the peptide bond is stronger than other backbone bonds due to the resonance between the carbonyl group and the electron dense

nitrogen [27]. However, in the gas phase, the peptide bond is weakened by the presence of a proton hydrogen-bonded to the amide nitrogen thereby making the peptide bond the site for dissociation in CID [28]. As a result, b- and y-type product ions are typically observed in CID MS/MS spectra of protein ions.

1.2.2.2 Infrared multiphoton dissociation

Infrared multiphoton dissociation (IRMPD) utilizes the absorption of multiple IR photons to increase the internal energy of the parent ion [14]. For IRMPD, photons are typically provided a by continuous-wave CO_2 laser at a wavelength of 10.6 μm. The IR photons are absorbed by resonant bonds, such as the bonds along the protein backbone, which makes IRMPD a universal technique for the study of proteins and peptides. The absorption of a single photon does not impart enough energy to induce dissociation. The energy of the absorbed photon is redistributed over the vibrational modes of the protein ion [14, 25]. The absorption of multiple IR photons increases the ion internal energy above the dissociation threshold resulting in unimolecular dissociation, as in CID [24]. IRMPD also yields the formation of b- and y-type product ions as a result of peptide bond dissociation. Thus, IRMPD, like CID, is a "slow-heating" technique.

1.2.2.3 Electron capture dissociation

Electron capture dissociation (ECD) is a complementary alternative to CID and IRMPD as it provides a mechanism for protein backbone dissociation that does not rely on the increase of ion internal energy to dissociate the protein backbone. ECD results from the interaction of low energy electrons (< 1eV) with multiply charged cations (Equation 1.2)

$$\left[M + nH \right]^{n+} + e^{-}{}_{<1\,\mathrm{eV}} \rightarrow \left[M + nH \right]^{(n-1)+\bullet} \rightarrow \mathrm{product\ ions} \qquad \textbf{Equation 1.2}$$
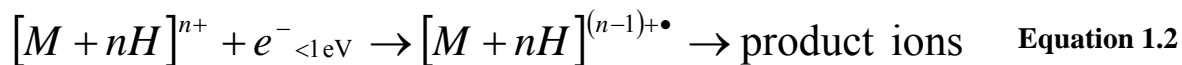
The multiply charged parent ion captures a low energy electron forming the charge-reduced species ($[M+nH]^{(n-1)+\bullet}$) for which the mass remains the same, but the number of charges is decreased. Recombination energy is released upon the capture of the electron, and the amount of energy released depends on the proton affinity and hydrogen atom affinity of the charge-reduced species [29]. The recombination energy is redistributed through the ion with only a minor increase in overall ion internal energy. The charge-reduced species undergoes radical-driven backbone dissociation resulting in cleavage of disulfide bonds and N-C_α bonds. Radical-driven dissociation of the N-C_α bond results in the formation of c'- and z•-ions (Scheme 1), and, through a minor dissociation pathway, cleavage of the C_α-C(O) bond results in the formation of a•- and y'-ions (Scheme 2) [30]. The prime notation indicates the presence of the neutralized proton on that product ion.
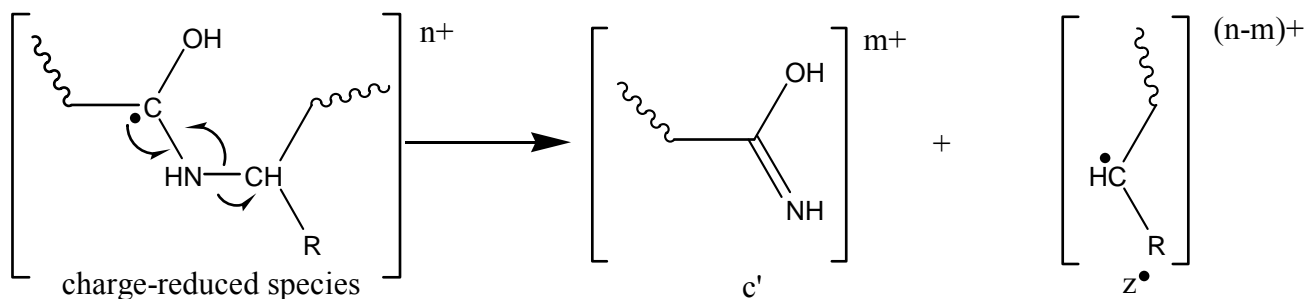
Scheme 1
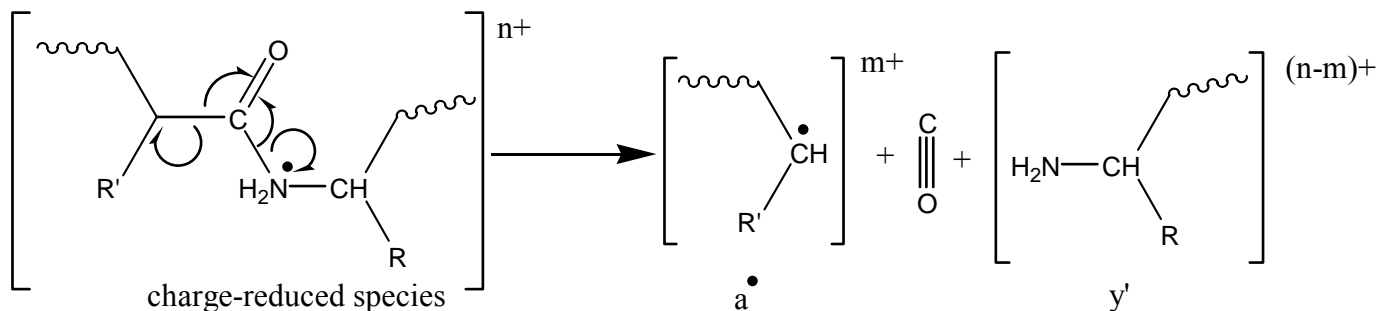
Scheme 2

The mechanism of ECD is currently under debate, particularly the location of the electron following capture by the multiply charged cation. It was initially proposed that electron capture occurred at a charge site and formed a radical hydrogen atom in the hot hydrogen model [31]. In this model, the hydrogen atom is released from the charge site and can be captured by locations of high hydrogen affinity, such as a disulfide bond or backbone carbonyl group [30, 32]. The capture of the hydrogen atom then initiated dissociation forming the product ions typical to ECD. The release and re-capture of the hydrogen radical was disputed when preferential disulfide bond cleavage was observed in a peptide dimer with charge sites distant from the disulfide linkage [33]. It was unlikely that a hydrogen atom released from the terminal charge site would travel across an alpha-helix to the disulfide bond, so it was concluded that mobile hydrogen atoms did not initiate backbone cleavage in ECD.

More recently, another model for ECD, the Coulomb stabilization postulate, has been proposed [33, 34]. The Coulomb stabilization postulate combines the electron capture process of the hot hydrogen model with the experimental results of disulfide and N-C_α bond cleavage. This postulate proposes that electron capture initially occurs in a high-n Rydberg orbital of a charge site, but electron transfer to the backbone dissociation site occurs before electron capture is complete [33]. The final location for the radical is proposed to be the S-S σ* or OCN π* orbital to initiate covalent bond dissociation observed in experiments [33, 34]. Calculations have shown that transfer from an excited Rydberg state to the S-S σ* or OCN π* orbital is an endothermic process and therefore impossible for low energy electrons to accomplish. However, Coulomb stabilization of the S-S σ* and OCN π* through interactions with nearby positively charged groups lowers the energy of these orbitals making electron

transfer energetically favorable [33, 34]. In summary, the Coulomb stabilization postulate proposes electron capture initially occurs at charge sites followed by electron transfer to the S-S $\sigma*$ or OCN $\pi*$ orbital where the electron initiates dissociation to the experimentally observed ECD product ions.

While the mechanism of ECD is not resolved, the experimental results show that ECD yields extensive backbone dissociation to form predominantly c'- and $z^{\bullet}$-ions [35]. Backbone dissociation in ECD shows no cleavage preference based on neighboring amino acid except for the limitation of cleavage on the N-terminal side of proline. Single covalent bond dissociation of the cyclic amino acid proline leaves one bond intact preventing separation of the product ions. ECD initiates backbone dissociation without the disruption of more labile groups, such as small-molecule post-translational modifications or noncovalent interactions [29]. As a result of the retention of noncovalent interactions, ECD can be used to study higher-order protein structure, which is impossible with CID and IRMPD [26].

To implement ECD, the parent ion must be multiply charged because the electron capture by a singly charged cation results in neutralization. The requirement of multiply charged parent ions makes the pairing of ECD with ESI practical. An advantage of using multiply charged parent ions is that the electron capture cross-section of an ion is proportional to the square of the charge [31, 36]. Therefore, higher charge ions have increased probability of electron capture to initiate backbone dissociation. Also, increased charge on a protein increases the formation of product ions. Product ion separation after backbone dissociation occurs through Coulombic repulsion between the positively charged N- and C-terminal products. The higher charge on each product ion ensures separation and detection [37].

14

Electron transfer dissociation (ETD), though not used in this work, is similar to ECD. Instead of the capture of a free electron as in ECD, an electron is donated to the multiply charged cation by a reagent anion with low electron affinity in the gas phase [38] (Equation 1.3).

$$[M + nH]^{n+} + A^{-\bullet} \rightarrow [M + nH]^{(n-1)+\bullet} + A \rightarrow \text{product ions} \qquad \textbf{Equation 1.3}$$
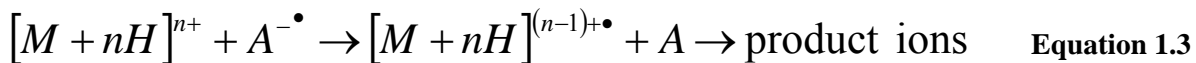
The recombination energy released during electron transfer is proposed to be less than what is released in ECD due to the electron affinity of the anion [33, 39, 40]. Similar dissociation patterns are observed for ETD MS/MS spectra with primary product ions arising from the dissociation of the N-C_α bond [38].

1.2.2.4 Hot electron capture dissociation

In the initial studies characterizing ECD, it was noticed that there was a second maximum in electron capture cross-section at electron energies around 10 eV [30, 41, 42]. In this hot electron capture dissociation (HECD), interactions between higher energy electrons (3-13 eV) and multiply charged cations produced similar product ions as observed in ECD [25, 42] (Equation 1.4).

$$[M + nH]^{n+} + e^{-}{}_{3\text{-}13\,\text{eV}} \rightarrow [M^* + nH]^{(n-1)+\bullet} \rightarrow \text{product ions} \qquad \textbf{Equation 1.4}$$
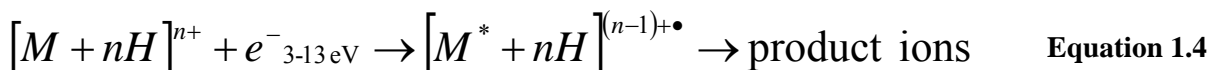
In addition to the formation of c′- and z•-ions from N-C_α bond cleavage, C_α-C bond cleavage led to increased formation of a•- and y′-ions along with the appearance of side-chain losses [41]. Secondary fragmentation was explained by increased parent ion internal energy. The transfer of electron kinetic energy to ion internal energy results in parent ion excitation prior to electron capture [41]. The excess internal energy is partitioned to the product ion upon backbone dissociation [43]. The increase in ion internal energy results in a higher percentage

of ions dissociating by the minor channel to form a$^{\bullet}$- and y$'$-type product ions [29]. As seen in Scheme 2, the neutralized hydrogen is located on the backbone amide nitrogen to induce dissociation of the C$_\alpha$-C(O) bond. To form this charge-reduced structure, the protonation site must be solvated by the backbone amide nitrogen. Charge solvation by the amide nitrogen is observed for CID and IRMPD in which the parent ion internal energy is increased prior to backbone dissociation. The increased ion internal energy can also result in radical migration within the z$^{\bullet}$-ions to induce the loss of side-chain moieties [41]. Secondary fragmentation in HECD differentiates leucine and isoleucine through characteristic side-chain losses, which is impossible in ECD [41]. HECD uses high kinetic energy electrons to increase the parent ion internal energy prior to dissociation yielding more extensive backbone dissociation than ECD.

1.2.2.5 Activated-ion electron capture dissociation

As mentioned previously, ECD results in the cleavage of backbone covalent bonds without disruption of noncovalent interactions. The retention of noncovalent interactions is useful for the study of higher-order structure but detrimental for the determination of the protein sequence. Intact noncovalent interactions can prevent the separation of product ions and thus decrease the sequence coverage for highly structured proteins [44]. The incorporation of vibrational excitation with ECD was found to increase the appearance of product ions for these large proteins via disruption of noncovalent interactions [45]. This technique, termed activated-ion ECD (AI-ECD), was initially applied to proteins with masses greater than 42 kDa [45] but found application for compact highly structured proteins as well [46]. AI-ECD techniques have incorporated collisional, IR, and thermal activation to induce unfolding of the gas-phase structure [44].

1.2.3 MS analysis of protein structure

1.2.3.1 Protein sequencing

Protein sequencing using mass spectrometry often incorporates enzymatic digestion prior to mass analysis to improve sequence coverage and identification. Commonly, the enzyme trypsin is used to cleave the protein as it cleaves on the C-terminal side of the basic residues arginine and lysine. Peptides cleaved by trypsin typically form di-cations in the gas phase due to protonation of the C-terminal basic residue and the N-terminus. The peptides produced from protein digestion are analyzed by mass spectrometry to determine accurate molecular masses or dissociated using MS/MS, with the most common technique being CID [14, 47]. Charges located at both termini ensure detection of complementary product ions when using CID for protein sequencing. CID is often used in ion traps which requires the application of a single frequency rf voltage to induce dissociation of an ion with a particular mass-to-charge ratio. Because of the commonality of CID, most sequencing programs were designed for the interpretation of CID MS/MS spectra.

ECD is a newer technique and therefore not as widespread as CID in protein sequence analysis. ECD cannot be performed in most instruments due to the difficulty producing and controlling low kinetic energy electrons which has contributed to the limited application for protein sequence analysis. ECD has been shown to provide much more extensive sequence coverage than CID increasing the probability of identification [29]. The extent of unbiased (except N-terminal of proline) backbone cleavage makes ECD advantageous for the analysis of peptides and proteins. Another advantage of ECD over CID is the retention of small-molecule post-translational modifications after backbone dissociation. However, ECD

is limited in the analysis of intact proteins due to the retention of noncovalent interactions which can prevent the separation of product ions [45].

1.2.3.2 Determination of local structure

Tandem mass spectrometry can also be used in the determination of protein secondary structure in a protein. MS/MS is often combined with solution-phase hydrogen/deuterium exchange (HDX) and liquid chromatography. In solution-phase HDX, a protein is dissolved in a solution containing a deuterated solvent, most often D_2O. Exchangeable hydrogens are divided into two categories based on exchange rate. Hydrogens located on the side-chains exchange rapidly and are not detected by solution-phase HDX due to equally rapid back-exchange. Amide hydrogens located on the backbone exchange more slowly and are detected with solution-phase HDX [48]. The use of amide hydrogens is advantageous as each amino acid except proline has an associated amide hydrogen thus creating the possibility for single-residue resolution. Comparison of amide hydrogen exchange rates is indicative of the environment. Amide hydrogens that are protected by hydrogen bonding, as in secondary structures, have decreased exchange rates from those amide hydrogens that are not involved in hydrogen bonding networks [48]. For the analysis of secondary structure, the protein must be digested into smaller peptides for detailed localization of hydrogen-deuterium exchange. Digestion of the deuterated protein with pepsin forms peptides with minimal scrambling of hydrogen and deuterium sites. These peptides can be separated by liquid chromatography and mass analyzed to determine deuterium uptake, but single-residue resolution is rare due to the size of the peptides formed during digestion with pepsin [37].

Single-residue resolution can be attained with the combination of tandem mass spectrometry with solution-phase HDX. Careful choice of the dissociation method is necessary to limit scrambling between hydrogen and deuterium sites. It has been shown that CID of deuterated peptides results in high H/D scrambling thereby eliminating the information of original deuterated sites [37]. H/D scrambling during CID stems from the increases in vibrational energy prior to backbone dissociation increasing hydrogen migration. ECD MS/MS has been combined with solution-phase HDX, and the combination of these techniques results in minimal scrambling of deuterated sites [37, 49]. The observed scrambling with ECD was attributed to increases in ion energy during the desolvation and parent ion isolation processes and the possibility for exchange between product ions before separation [37]. Currently, HDX cannot differentiate between secondary structural elements, but single-residue resolution reveals the location of secondary structure.

1.2.3.3 Protein conformation analysis

Mass spectrometry has provided new methods to study protein tertiary structure. Various techniques, including ion mobility spectrometry (IMS) and solution- and gas-phase HDX, have been used to study conformational changes. IMS makes use of frictional forces from collisions between ions and neutral gas molecules to separate ions based on the shape-to-charge ratio and to calculate a cross-section based on the drift time of the ion [50]. It has been shown by IMS that proteins adopt multiple conformations for a given charge state in the gas phase [11, 51]. Solution-phase HDX has been used to monitor protein unfolding using the changes in deuterium uptake at various time points followed by mass spectrometry of peptides from enzymatic digestion to determine which regions are changing conformation [48]. Also, the amount of deuterium incorporated into a protein is indicative of overall

structure with denatured proteins exchanging higher numbers of amide hydrogens for deuteriums. Gas-phase HDX exchanges side-chain hydrogens for deuterium due to more a basic deuterium source (ND_3) and shorter reaction times. The study of ubiquitin by gas-phase HDX revealed a positive correlation between ion charge state and extent of deuterium incorporation [52]. The increase in the number of deuterium atoms indicates a more unfolded structure as the charge state of the ion increases, a trend that has also been shown in IMS [11, 53].

ECD has also been used to probe tertiary structure of gas-phase proteins. Because ECD results in the cleavage of the peptide backbone without the disruption of noncovalent interactions, the gas-phase higher-order structure is not disturbed by backbone dissociation. The extensive nature of backbone cleavage from ECD often results in formation of product ions between each residue (except N-terminal of proline), and the absence of product ions would indicate structural protection. It has been shown that ECD can reveal protein unfolding resulting from increased protein ion charge state [54]. Various charge state ions of the helical bundle protein KIX were dissociated using ECD [55]. It was noticed that as the charge state was increased, the extent and abundance of product ions increased in three different regions. It was concluded that the product ion distribution from ECD revealed the unraveling of the three helices that comprise the KIX protein.

1.2.3.4 MS of macromolecular complexes

The analysis of quaternary protein structure was the domain of solution-phase techniques before the development of ESI. ESI provides a method for the transfer of intact noncovalent complexes to the gas phase for analysis by mass spectrometry. To maintain intact gas-phase complex, ESI is typically performed using aqueous ammonium acetate

20

buffer at physiological pH [6, 19]. Accurate molecular mass measurements can be used to determine stoichiometric ratios of the individual proteins in the complex. CID can be used to confirm the stoichiometry of a complex through the dissociation of the complex into the individual proteins [6, 19].

ECD has not yet been applied to the study of quaternary protein structure, but ETD has been used in the analysis of immunoglobulin G (IgG) [56]. It was found that ETD of the intact IgG ion resulted in multiple electron transfer events without observed c'- and $z^{\bullet}$-ions. The lack in the formation of the c'- and $z^{\bullet}$-type product ions was due to the abundance of disulfide linkages in IgG which are preferential dissociation sites in ETD and ECD [56]. Reduction of the disulfide bonds followed by ETD resulted in extensive backbone cleavage and product ion formation but limited quaternary structure information.

1.3 Summary

In this chapter, protein structure and the techniques to study protein structure were introduced. Mass spectrometry is a powerful technique with many variations to study each level of protein structure. Protein sequencing is aided by a dissociation technique that is rapid and provides extensive cleavage of the backbone, as observed with ECD. ECD is also aptly suited for the study of higher-order protein structure by tandem mass spectrometry because of extensive backbone cleavage and the retention of the noncovalent interactions that define protein structure. The work presented in this dissertation highlights the uses of ECD and improvements using IR activation in the analysis of proteins and peptides.

Chapter 2 describes the implementation of ECD in a linear ion trap (LIT) compared to the traditional use in a FTICR mass spectrometer. The modifications added to a hybrid LIT mass spectrometer to incorporate multiple modes of ion activation are described.

Chapter 3 highlights the benefits of the incorporation of IR activation with ECD in the sequencing of peptides and proteins, using melittin and ubiquitin as examples. The addition of IR activation sequentially to and simultaneously with ECD increases of the formation of c'- and $z^{\bullet}$-ions thereby increasing the sequence coverage. The data show that simultaneous application of IR activation with ECD yields the greatest increase in sequence coverage. The implications of a collinear photon and electron beam are evaluated and discussed.

Chapter 4 explains the observations of increased product ion formation during AI-ECD through IR-induced structural unfolding. The data show that IR activation increases the prevalence of C-terminal product ions indicating unfolding of the C-terminus of ubiquitin ions. Also, the product ion distribution from simultaneous AI-ECD is used to determine protonation sites in multiple charge state ions of ubiquitin. The data show that analysis of the same product ion distribution can also be used to predict the sites of electron capture.

Chapter 5 describes the use of the ion-molecule reaction between radical cations and molecular oxygen to probe radical reactivity. The $z^{\bullet}$-type product ions from ECD, AI-ECD, and HECD are studied and shown to have different reactivities. The data conclude that product ion internal energy influences the reactivity of the $z^{\bullet}$-ion, and it is hypothesized that increased internal energy results in radical migration away from the N-terminal alpha-carbon to more stable, and therefore less reactive, location along the peptide backbone.

The results from the application of AI-ECD to the study of protein structure are summarized in Chapter 6. The methods used are analyzed and critiqued, and future experiments to confirm the results presented in this dissertation are proposed.

1.4 References

1.   Paoli, M., R. Liddington, J. Tame, A. Wilkinson, and G. Dodson Crystal structure of T state haemoglobin with oxygen bound at all four haems. *Journal of Molecular Biology*. **1996,** *256,* 775-792.

2.   Thomas, P.J., B.H. Qu, and P.L. Pedersen Defective Protein-Folding as a Basis of Human-Disease. *Trends in Biochemical Sciences*. **1995,** *20,* 456-459.

3.   Dobson, C.M. Protein folding and misfolding. *Nature*. **2003,** *426,* 884-890.

4.   Dobson, C.M. Protein misfolding, evolution and disease. *Trends in Biochemical Sciences*. **1999,** *24,* 329-332.

5.   Dobson, C.M. Protein-misfolding diseases: Getting out of shape. *Nature*. **2002,** *418,* 729-730.

6.   Heck, A.J.R. and R.H.H. van den Heuvel Investigation of intact protein complexes by mass spectrometry. *Mass Spectrometry Reviews*. **2004,** *23,* 368-389.

7.   Kjeldsen, F., M.M. Savitski, C.M. Adams, and R.A. Zubarev Determination of the location of positive charges in gas-phase polypeptide polycations by tandem mass spectrometry. *Int. J. Mass Spectrom.* **2006,** *252,* 204-212.

8.   Oh, H., K. Breuker, S.K. Sze, Y. Ge, B.K. Carpenter, and F.W. McLafferty Secondary and tertiary structures of gaseous protein ions characterized by electron capture dissociation mass spectrometry and photofragment spectroscopy. *PNAS*. **2002,** *99,* 15863-15868.

9.   Freitas, M.A., C.L. Hendrickson, M.R. Emmett, and A.G. Marshall Gas-phase bovine ubiquitin cation conformations resolved by gas-phase hydrogen/deuterium exchange rate and extent. *Int. J. Mass Spectrom.* **1999,** *185/186/187,* 565-575.

10.   Breuker, K. and F.W. McLafferty Stepwise evolution of protein native structure with electrospray into the gas phase, 10(-12) to 10(2) S. *PNAS*. **2008,** *105,* 18145-18152.

11.   Myung, S., E. Badman, Y. Lee, and D. Clemmer Structural transitions of electrosprayed ubiquitin ions stored in an ion trap over similar to 10 ms to 30 s. *J. Phys. Chem. A*. **2002,** *106,* 9976-9982.

12.   Ly, T. and R.R. Julian Elucidating the Tertiary Structure of Protein Ions in Vacuo with Site Specific Photoinitiated Radical Reactions. *J. Am. Chem. Soc.* **2010,** *132,* 8602-8609.

13.   Budnik, B.A., M.L. Nielsen, J.V. Olsen, K.F. Haselmann, P. Horth, W. Haehnel, and R.A. Zubarev Can relative cleavage frequencies in peptides provide additional sequence information? *Int. J. Mass Spectrom.* **2002,** *219,* 283-294.

14.   Hoffmann, E.d. and V. Stroobant, *Mass Spectrometry: Principles and Applications, 2 ed*. 2002, New York: John Wiley & Sons. 407.

15.   van den Heuvel, R.H. and A.J.R. Heck Native protein mass spectrometry: from intact oligomers to functional machineries. *Current Opinion in Chemical Biology*. **2004,** *8,* 519-526.

16.   Cai, X.M. and C. Dass Conformational analysis of proteins and peptides. *Current Organic Chemistry*. **2003,** *7,* 1841-1854.

17.   Fenn, J.B., M. Mann, C.K. Meng, S.F. Wong, and C.M. Whitehouse Electrospray Ionization for Mass Spectrometry of Large Biomolecules. *Science*. **1989,** *246,* 64-71.

18.   Tanaka, K., H. Waki, Y. Ido, S. Akita, Y. Yoshida, and T. Yoshida Protein and Polymer Analyses up to m/z 100000 by Laser Ionization Time-of-flight Mass Spectrometry. *Rapid Commun. Mass Spectrom.* **1988,** *2,* 151-153.

19.   Benesch, J.L. and C.V. Robinson Mass spectrometry of macromolecular assemblies: preservation and dissociation. *Current Opinion in Structural Biology*. **2006,** *16,* 245-251.

20.   Kebarle, P. and M. Peschke On the mechanisms by which the charged droplets produced by electrospray lead to gas phase ions. *Analytica Chimica Acta*. **2000,** *406,* 11-35.

21.   Schnier, P.D., D.S. Gross, and E.R. Williams On the Maximum Charge-State and Proton-Transfer Reactivity of Peptide and Protein Ions Formed by Electrospray-Ionization. *J. Am. Soc. Mass Spectrom.* **1995,** *6,* 1086-1097.

22.   Steinberg, M.Z., K. Breuker, R. Elber, and R.B. Gerber The dynamics of water evaporation from partially solvated cytochrome c in the gas phase. *Phys. Chem. Chem. Phys.* **2007,** *9,* 4690-4697.

23.   Roepstorff, P. Proposal for a Common Nomenclature for Sequence Ions in Mass Spectra of Peptides. *Biomedical Mass Spectrometry*. **1984,** *11,* 601.

24.   McLuckey, S.A. and D.E. Goeringer Slow heating methods in tandem mass spectrometry. *Journal of Mass Spectrometry*. **1997,** *32,* 461-474.

25.   Sleno, L. and D.A. Volmer Ion activation methods for tandem mass spectrometry. *Journal of Mass Spectrometry*. **2004,** *39,* 1091-1112.

26.   Badman, E.R., C.S. Hoaglund-Hyzer, and D.E. Clemmer Dissociation of Different Conformations of Ubiquitin Ions. *J. Am. Soc. Mass Spectrom.* **2002,** *13,* 719 - 723.

27.   Haschemeyer, R.H. and A.E.V. Haschemeyer, *Proteins: A Guide to Study by Physical and Chemical Methods*. 1973, New York: John Wiley & Sons.

28. McCormack, A.L., A. Somogyi, A.R. Dongré, and V.H. Wysocki Fragmentation of Protonated Peptides: Surface-Induced Dissociation in Conjunction with a Quantum Mechanical Approach. *Anal. Chem.* **1993,** *65,* 2859-2872.

29. Zubarev, R.A., K.F. Haselmann, B. Budnik, F. Kjeldsen, and F. Jensen Towards an Understanding of the Mechanism of Electron-Capture Dissociation: A Historical Perspective and Modern Ideas. *European Journal of Mass Spectrometry.* **2002,** *8,* 337-349.

30. Zubarev, R.A. Reactions of Polypeptide Ions with Electrons in the Gas Phase. *Mass Spectrometry Reviews.* **2003,** *22,* 57 - 77.

31. Zubarev, R.A., D.M. Horn, E.K. Fridriksson, N.L. Kelleher, N.A. Kruger, M.A. Lewis, B.K. Carpenter, and F.W. McLafferty Electron Capture Dissociation for Stuctural Characterization of Multiply Charged Protein Cations. *Anal. Chem.* **2000,** *72,* 563-573.

32. Zubarev, R.A., N.A. Kruger, E.K. Fridriksson, M.A. Lewis, D.M. Horn, B.K. Carpenter, and F.W. McLafferty Electron Capture Dissociation of Gaseous Multiply-charged Proteins is Favored at Disulfide Bonds and Other Sites of High Hydrogen Atom Affinity. *J. Am. Chem. Soc.* **1999,** *121,* 2857-2862.

33. Simons, J. Mechanisms for S-S and N-C-alpha bond cleavage in peptide ECD and ETD mass spectrometry. *Chem. Phys. Lett.* **2010,** *484,* 81-95.

34. Neff, D. and J. Simons Analytical and Computational Studies of Intramolecular Electron Transfer Pertinent to Electron Transfer and Electron Capture Dissociation Mass Spectrometry. *J. Phys. Chem. A.* **2010,** *114,* 1309-1323.

35. Zubarev, R.A., N.L. Kelleher, and F.W. McLafferty Electron Capture Dissociation of Multiply Charged Protein Cations. A Nonergodic Process. *J. Am. Chem. Soc.* **1998,** *120,* 3265-3266.

36. Robinson, E.W., R.D. Leib, and E.R. Williams The Role of Conformation on Electron Capture Dissociation of Ubiquitin. *J. Am. Soc. Mass Spectrom.* **2006,** *17,* 1470 - 1480.

37. Rand, K.D., C.M. Adams, R.A. Zubarev, and T.J.D. Jorgensen Electron Capture Dissociation Proceeds with a Low Degree of Intramolecular Migration of Peptide Amide Hydrogens. *J. Am. Chem. Soc.* **2008,** *130,* 1341 - 1349.

38. Syka, J.E.P., J.J. Coon, M.J. Schroeder, J. Shabanowitz, and D.F. Hunt Peptide and protein sequence analysis by electron transfer dissociation mass spectrometry. *PNAS.* **2004,** *101,* 9528-9533.

39. Sohn, C.H., C.K. Chung, S. Yin, P. Ramachandran, J.A. Loo, and J.L. Beauchamp Probing the Mechanism of Electron Capture and Electron Transfer Dissociation Using Tags with Variable Electron Affinity. *J. Am. Chem. Soc.* **2009,** *131,* 5444-5459.

40.   Li, X.J., C. Lin, L. Han, C.E. Costello, and P.B. O'Connor Charge Remote Fragmentation in Electron Capture and Electron Transfer Dissociation. *J. Am. Soc. Mass Spectrom.* **2010,** *21,* 646-656.

41.   Kjeldsen, F., K.F. Haselmann, B.A. Budnik, F. Jensen, and R.A. Zubarev Dissociative capture of hot (3-13 eV) electrons by polypeptide polycations: an efficient process accompanied by secondary fragmentation. *Chem. Phys. Lett.* **2002,** *356,* 201-206.

42.   Cooper, H.J., K. Hakansson, and A.G. Marshall The Role of Electron Capture Dissociation in Biomolecular Analysis. *Mass Spectrometry Reviews.* **2005,** *24,* 201 - 222.

43.   Cooks, R.G., J.H. Beynon, R.M. Caprioli, and G.R. Lester, *Metastable Ions.* 1973, Amsterdam: Elsevier Scientific Publishing Company.

44.   Horn, D.M., K. Breuker, A.J. Frank, and F.W. McLafferty Kinetic Intermediates in the Folding of Gaseous Protein Ions Characterized by Electron Capture Dissociation Mass Spectrometry. *J. Am. Chem. Soc.* **2001,** *123,* 9792-9799.

45.   Horn, D.M., Y. Ge, and F.W. McLafferty Activated Ion Electron Capture Dissociation for Mass Spectral Sequencing of Larger (42 kDa) Proteins. *Anal. Chem.* **2000,** *72,* 4778-4784.

46.   Cooper, H.J., M.A. Case, G.L. McLendon, and A.G. Marshall Electrospray ionization Fourier transform ion cyclotron resonance mass spectrometric analysis of metal-ion selected dynamic protein libraries. *J. Am. Chem. Soc.* **2003,** *125,* 5331-5339.

47.   Howard, G.C. and W.E. Brown, eds. *Modern Protein Chemistry: Practical Aspects.* 2002, CRC Press: Boca Raton. 257.

48.   Marcsisin, S.R. and J.R. Engen Hydrogen exchange mass spectrometry: what is it and what can it tell us? *Analytical and Bioanalytical Chemistry.* **2010,** *397,* 967-972.

49.   Pan, J., J. Han, C.H. Borchers, and L. Konermann Electron Capture Dissociation of Electrosprayed Protein Ions for Spatially Resolved Hydrogen Exchange Measurements. *J. Am. Chem. Soc.* **2008,** *130,* 11574-11575.

50.   Bohrer, B.C., S.I. Mererbloom, S.L. Koeniger, A.E. Hilderbrand, and D.E. Clemmer Biomolecule Analysis by Ion Mobility Spectrometry. *Annual Review of Analytical Chemistry.* **2008,** *1,* 293-327.

51.   Shelimov, K.B., D.E. Clemmer, R.R. Hudgins, and M.F. Jarrold Protein Structure *in Vacuo*: Gas-Phase Conformations of BPTI and Cytochrome c. *J. Am. Chem. Soc.* **1997,** *119,* 2240-2248.

52. Rand, K.D., S.D. Pringle, J.P. Murphy, K.E. Fadgen, J. Brown, and J.R. Engen Gas-Phase Hydrogen/Deuterium Exchange in a Traveling Wave Ion Guide for the Examination of Protein Conformations. *Anal. Chem.* **2009,** *81,* 10019-10028.

53. Badman, E.R.H.-H., C. S.; Clemmer, D. E. Monitoring Structural Changes of Proteins in an Ion Trap over 10 - 200 ms: Unfolding Transitions in Cytochrome *c* Ions. *Anal. Chem.* **2001,** *73,* 6000-6007.

54. Breuker, K., H. Oh, D.M. Horn, B.A. Cerda, and F.W. McLafferty Detailed Unfolding and Folding of Gaseous Ubiquitin Ions Characterized by Electron Capture Dissociation. *J. Am. Chem. Soc.* **2002,** *124,* 6407-6420.

55. Breuker, K. and M. Tollinger. *Gas-Phase Structures of the Three Helix Bundle Protein KIX Probed by Electron Capture Dissociation.* in *The 58th ASMS Conference on Mass Spectrometry and Allied Topics.* 2010. Salt Lake City, UT.

56. Tsybin, Y., H.B. Hamidane, M. Groessl, P. Dyson, J. Simicevic, B. Deplancke, S. Nallet, F. Wurm, C. Stoermer, and R. Hartmer. *Top-Down Structural Analysis of 60-150 kDa Proteins with ETD-Based Tandem Mass Spectrometry.* in *The 58th Conference on Mass Spectrometry and Allied Topics.* 2010. Salt Lake City, UT.

Chapter 2

Instrumentation and Experimental Design

for Activated-Ion Electron Capture Dissociation Mass Spectrometry

2.1 Instruments for electron capture dissociation mass spectrometry

Electron capture dissociation (ECD) mass spectrometry was developed using Fourier transform ion cyclotron resonance (FTICR) mass spectrometers [1]. To date, most electron capture experiments are performed in these instruments [2]. As an alternative to a FTICR, linear ion traps (LIT) have been modified to perform ECD [3]. The research presented in this dissertation utilizes ECD in a hybrid linear ion trap / time-of-flight (LIT-TOF) instrument.

There are several differences between a FTICR and a LIT mass spectrometer to consider when comparing the use of ECD in each instrument. The first difference to consider between these two instruments is the trapping, manipulation, and detection of ions. In a FTICR, the ions are trapped through the combination of electrostatic and magnetic fields [4, 5]. The magnetic field induces an ion cyclotron resonance frequency specific to the mass-to-charge ratio of the ion, and the combination of the magnetic and electrostatic fields imposes a magnetron motion on the injected ion packets [5]. The magnetron motion results in a disperse ion cloud often about a centimeter in diameter [6, 7]. In a FTICR, ion manipulation occurs through the application of a radio frequency (rf) voltage that is specific to the cyclotron frequency of ions of a particular mass-to-charge ratio. Detection is performed by applying a broadband rf voltage that excites all of the ions thereby increasing the cyclotron radius for all ions. The increase in ion cyclotron radius results in ion detection

by the measurement of the current induced by the ions on detecting plates. In a LIT, the ions are radially confined along the central axis by a two-dimensional quadrupolar field and axially confined by electrostatic dc potentials [3, 4, 8]. The ion motion is controlled by the rf voltage applied to the rods of the LIT, and the electrostatic lenses gate the ions into and out of the LIT. When a LIT is used for ECD, it has been paired with a separate mass analyzer, commonly a time-of-flight (TOF) analyzer, for more sensitive analysis [3]. Mass analysis by a TOF followed by ion detection using a microchannel plate detector (MCP) increases the rate of data acquisition. Ion detection in a FTICR takes approximately one spectrum per second where a single spectrum is collected in microseconds using a TOF for mass analysis [4, 5, 9].

Due to the differences in ion trapping and analysis, the gas pressure in a FTICR and LIT is drastically different. The ions in an ICR must remain in a coherent packet for detection so any collisions between ions and neutral molecules decrease accuracy and sensitivity via the disruption of ion packet coherence [4, 10]. To reduce the probability of collisions, the ICR cell is kept under ultrahigh vacuum with a cell pressure around 10^{-10} mbar. In contrast, ion traps benefit from higher pressures as the bath gas aids in the radial confinement of the ions through collisional damping [4, 8]. Typically, the operating pressure of a LIT is on the order of 10^{-2} mbar which is eight orders of magnitude higher than a FTICR. To reach these high pressures in a LIT, a bath gas, typically helium, is leaked into the instrument.

Aside from fundamental differences in the operation of these two instruments, the electron sources used in a FTICR and in a LIT are different in shape and electron beam cross-section but operate under the same principle of thermionic electron emission. One of

the reasons that ECD was developed in a FTICR was the trouble associated with the generation of low kinetic energy electrons in other mass analyzers such as three-dimensional ion traps. The rf voltages required to trap the ions in a three-dimensional ion trap also resulted in electron acceleration into a range of energies that was not useful for ECD [11, 12]. A FTICR does not use rf voltages for ion trapping, so electron heating is not an issue in these instruments [3]. The FTICR commonly uses an indirectly heated disk electrode to provide a column of low kinetic energy electrons [13]. To ensure ion-electron overlap, the electron beam must be wide enough to irradiate all of the ions simultaneously, often requiring beam diameters on the order of a centimeter. The electron beam must also be centered through the ICR to ensure sufficient overlap of ions and electrons [14]. In contrast to the disk electrode used in a FTICR, the LIT uses an edged filament as the electron source [3, 8]. The filament produces a beam of electrons approximately one millimeter in diameter aligned along the central axis of the LIT with a narrow range of electron energies [8]. Because the ions are radially confined along the central axis of the LIT, a narrower electron beam can be used.

The overlap of the ions and the electrons is crucial to the efficiency of ECD because the overlap affects the activation time required for a given experiment. Another aspect of the electron source that affects the activation time required is the density of the electron beam. Both an indirectly heated disk electrode and an electron filament release similar amounts of electron current [8], but the area of the electron beam produced by the filament is much smaller than that produced by the disk electrode. The difference in electron beam cross-section results in a higher electron density produced by the filament, approximately 200 times greater than what is produced by the disk electrodes used in a FTICR [8]. The increase in electron beam density produced by the filament results in shorter activation times

for ECD in a LIT due to the increased probability of electron capture [8]. Ion activation in a FTICR can take hundreds of milliseconds while the LIT requires only tens of milliseconds [6, 8].

2.2 Peptide and protein analysis using the LIT-TOF

2.2.1 General function and data analysis

The instrument used in this research is a prototype NanoFrontier hybrid LIT-TOF mass spectrometer from the Hitachi Corporation (Hitachi High Technologies). A schematic of the LIT-TOF is shown in Figure 2.1, and the LIT-TOF was modified to incorporate multiple ion activation modes, as explained below.

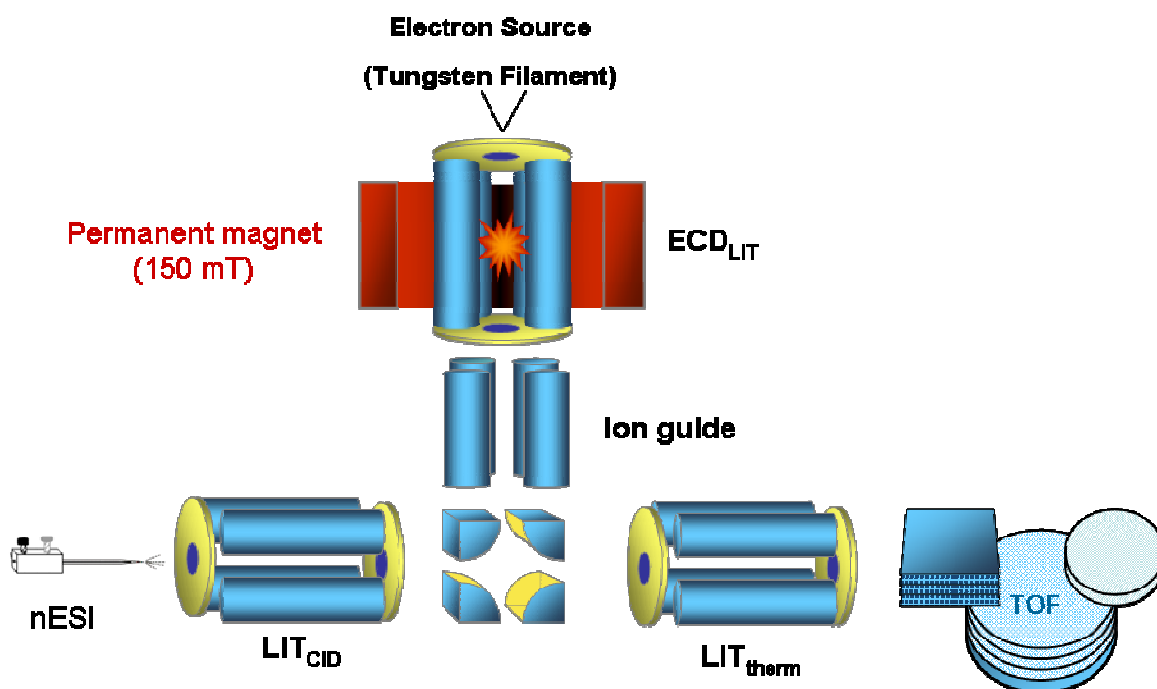**Figure 2.1** Schematic of the prototype NanoFrontier LIT-TOF provided by the Hitachi Corporation (Hitachi High Technologies).

This mass spectrometer consists of three LITs arranged in a T-configuration followed by a TOF mass analyzer. Ions are generated using nano-electrospray ionization (nESI) and are accumulated in the first LIT (LIT_{CID}) where parent ion isolation is performed. Collision

31

induced dissociation (CID) can also be implemented in this LIT. The ions are then

transferred through a quadrupole deflector to a second LIT (ECD$_{LIT}$) where ion activation

occurred in these experiments. Activation times were kept to less than 75 ms. Ion

transmission into and out of the ECD$_{LIT}$ is aided by a quadrupolar ion guide. After ion

activation, product ions are transferred to the third LIT (LIT$_{therm}$) where they are stored prior

to TOF mass analysis. In the LIT$_{therm}$, collisions between the ions and the bath gas are used

to disperse the ion packets injected from the ECD$_{LIT}$ into a continuous ion beam. Energy

focusing the ions into a continuous beam prior to TOF analysis was shown to improve ion

transmission into the TOF and mass resolution [9, 15].

Data analysis is performed using software developed in-house by Dr. Takashi Baba

written with LabView code (National Instruments). The program identifies product ion

peaks via comparison of experimental mass-to-charge ratios to a list of theoretical

mass-to-charge ratios. The list of theoretical mass-to-charge ratios is developed from an

amino acid sequence and the parent ion charge state. The program selects product ion peaks

by an abundance threshold and mass tolerance. A peak intensity error associated with the

deviation of the experimental isotopic distribution from the theoretical distribution is also

provided by the program. The isotopic distribution is crucial for ion identification because

the distribution is specific to the chemical composition of the ion. The error in peak intensity

is used as a criterion of ion identification as it represents the accuracy of ion chemical

composition. All types of product ions, a-, b-, c-, x-, y-, and z-type ions, are searched

simultaneously. The program-identified peaks are then confirmed manually to be the

appropriate mass and charge state as well as having a sufficient signal-to-noise ratio (S/N >

3).

The program is limited to select product ions with charge states less than or equal to five, so analysis of highly charged ions (n > 10) is limited but not impossible. Highly charged ions have decreased the overlap of complementary product ions as the larger product ions are too highly charged for accurate identification. In these experiments, the lack of identification for highly charged ions decreased the summed product ion abundance and the number of product ions observed for a specific technique. The sequence coverage effected by dissociation was not decreased as inter-residue cleavage that yielded highly charged product ions also yielded complementary low charge product ions that were accurately identified. The most highly charged ion used in this study was the +12 charge state of ubiquitin. Electron capture by the +12 charge state ion produced the +11 ion. Product ions from the dissociation of the +11 ion with charge states higher than five had complementary product ions that had less than or equal to five charges which were easily identified.

2.2.2 Pressure and temperature in the ECD$_{LIT}$

In the analysis of peptides and proteins, the pressure and temperature in the ECD$_{LIT}$ are important variables for understanding the effects of collisional cooling and IR activation. Helium gas is leaked into the ECD$_{LIT}$ using a mass flow controller and can be varied from 0.25 to 4.00 sccm. Under standard conditions, the flow rate was set to 2.00 sccm. The pressure of the ECD$_{LIT}$ was calculated using the conductance through the ECD$_{LIT}$ and the flow rate of helium into the ECD$_{LIT}$. The flow limiting aperture between the ECD$_{LIT}$ and the vacuum pumps is a 3 mm circular hole located between the ECD$_{LIT}$ and the ion guide. To calculate the conductance through the ECD$_{LIT}$, the thin aperture equation was used (Equation 2.1) [16].

$$\text{Conductance} = 3.7 \times \left(\frac{T}{m}\right)^{1/2} \times A \qquad \textbf{Equation 2.1}$$

In the conductance equation, T is the temperature in the ECD_{LIT}, m is the mass of the bath

gas, i.e., 4 dalton for helium, and A is the area of the conductance limit, i.e., $\pi \times (0.15\ cm)^2$.

The calculated conductance was then used in the gas flow equation (Equation 2.2) [16].

$$Q = C\left(P_1 - P_2\right) \qquad \textbf{Equation 2.2}$$

In this equation, Q is the flow through the chamber, which is regulated by the mass flow

controller, C is the conductance calculated from Equation 2.1, and P_1 and P_2 are the pressures

in and out of the ECD_{LIT}, respectively. The temperature was initially assumed to be 20°C,

which led to a calculated pressure of 0.055 mbar for a flow rate of 2.00 sccm. However, the

assumed temperature was most likely incorrect because radiative heating from the electron

filament was not considered.

The temperature in the ECD_{LIT} was measured over a time span of seven hours using a

thermocouple placed close to the center of the ECD_{LIT}. The filament power supply was set to

a standard operating current of 1.00 A, and the temperature was monitored as the bath gas

was heated (Figure 2.2.a)
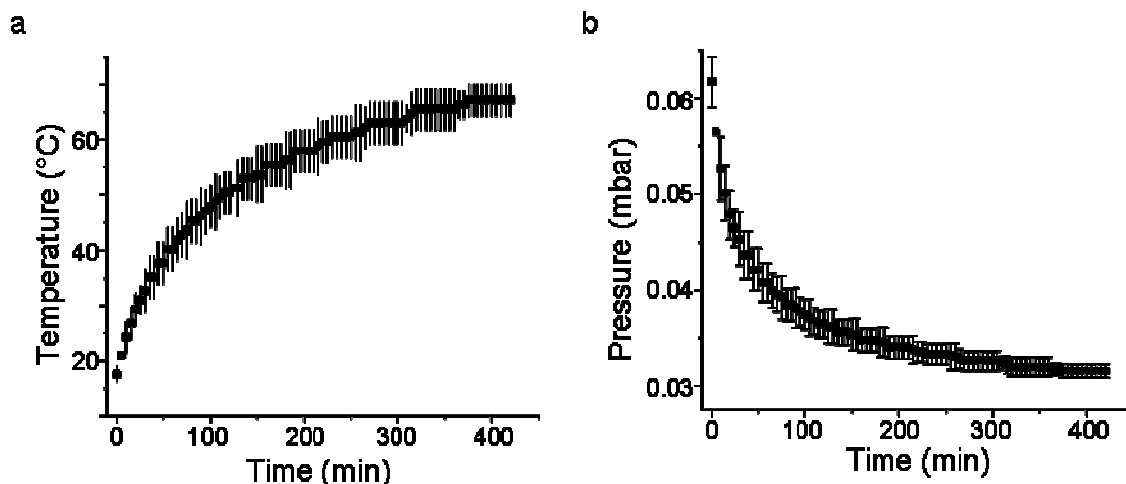
Figure 2.2 a) Temperature in the ECD_{LIT} as a function of filament heating. b) Pressure in the ECD_{LIT} as a function of filament heating. The measured temperature was used to calculate the conductance through the ECD_{LIT} which was then used to calculate the pressure. Temperature measurements were taken every five minutes over seven hours and averaged over three runs.

It was observed that the temperature of the ECD_{LIT} increased rapidly over the first two hours followed by slow increments of approximately one degree per hour to a maximum of 67°C. The increases in temperature resulted increased conductance through the ECD_{LIT} (Equation 2.1). The increased conductance at higher temperatures resulted in a decrease in pressure in the ECD_{LIT} (Figure 2.2.b). The temperature and pressure curves were fit using exponential functions, and it was found that steady-state conditions in the ECD_{LIT} were 65°C and 0.032 mbar.

2.3 Ion activation in the ECD_{LIT}

To perform the variety of experiments required of this instrument, several modifications were made to the prototype NanoFrontier mass spectrometer. These modifications consisted of additions to increase the number of methods available for ion activation. Electron kinetic energy was controlled by a dc bias between the electron filament and the rods of the ECD_{LIT}. For IR activation and infrared multiphoton dissociation (IRMPD), a CO_2 laser was added and aligned collinearly with the electron beam through the

35

ECD$_{LIT}$. Supplemental ac activation was applied to the one pair of the quadrupolar rods of the ECD$_{LIT}$ for collisional activation (Figure 2.3).
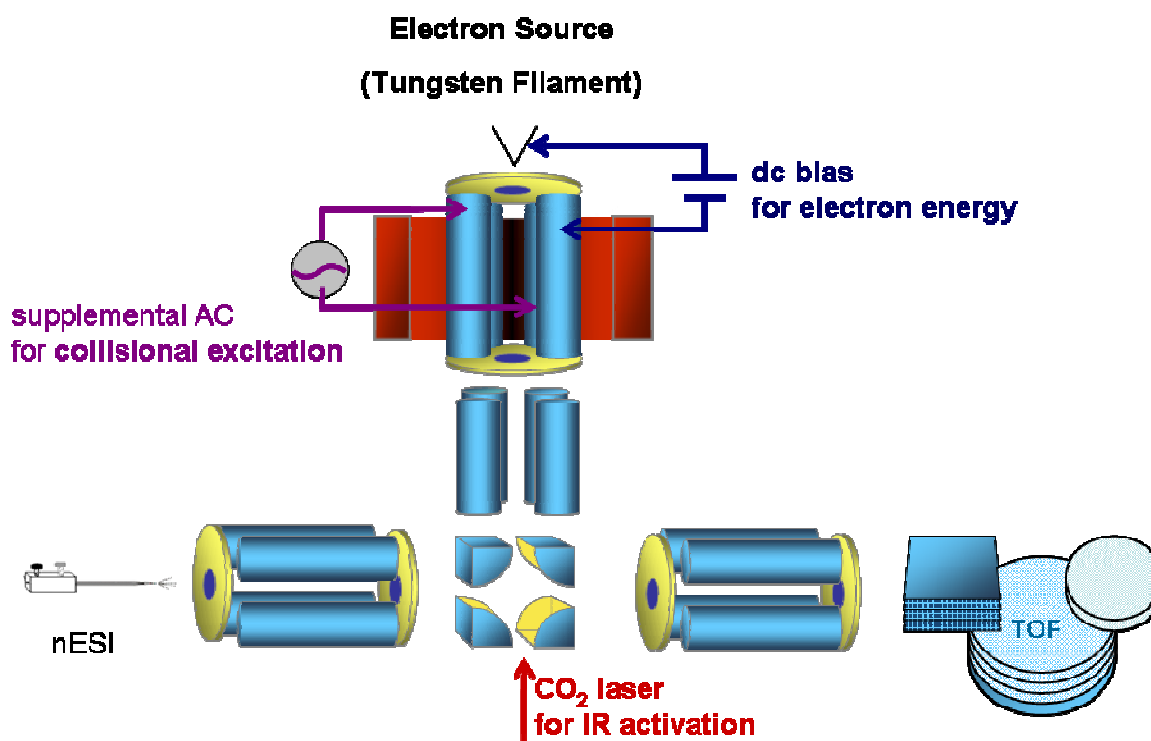
Figure 2.3 Schematic highlighting the controls for different ion activation methods in the LIT-TOF. Modifications to the NanoFrontier include the addition of supplemental ac voltage applied to the rods of the ECD$_{LIT}$ and the addition of a CO_2 laser aligned collinearly with electron beam.

2.3.1 Electron capture methods

The ECD$_{LIT}$ consists of a quadrupole LIT surrounded by a neodymium permanent magnet. The ions are focused along the central axis of the LIT by the quadrupolar field, and radial confinement is aided by collisions of the ions with the helium bath gas. The amplitude of the rf voltage applied to the rods of the ECD$_{LIT}$ can be varied to set the potential well-depth and control radial confinement of the ions. Bath gas pressure is regulated by a mass flow controller that determines the flow of helium bath gas into the ECD$_{LIT}$. The pressure was calculated using the thin aperture conductance formula for the molecular flow

regime [16], flow rate into the ECD_{LIT}, and the temperature of the LIT when the electron filament was powered (see above).

Electrons are generated from the point of a bent thoriated tungsten filament located at the end of the ECD_{LIT} opposite to the ion entrance. In the initial configuration, the ions and electrons entered the ECD_{LIT} from the same end, but this configuration resulted in low transmission for both ions and electrons [3]. In design of the next generation instrument, ions and electrons followed different paths to the ECD_{LIT} and the electron source was moved much closer to the ECD_{LIT} resulting in increased transmission of both [8]. To generate low kinetic energy electrons, a current on the order of 1 A is passed through this filament, and electrons are thermally emitted. Electron kinetic energy is controlled by the dc bias between the filament and the rods of the ECD_{LIT} which accelerates the electrons prior to entering the LIT. The previous problems of electron heating were eliminated with the use of a LIT because the two-dimensional rf field is applied to the rods, only affecting the x- and y-directions. The electrons are injected along the z-axis where there is no rf field [3]. For an ECD experiment, a potential of 20.0 V was applied to the filament (filament offset), and a potential of 19.5 V was applied to the rods of the ECD_{LIT} (ECD offset). The potential difference between the filament and the rods of the ECD_{LIT} must be corrected for the difference in work function between the tungsten filament and the stainless steel rods of the ECD_{LIT} [17]. The work function is the minimum amount of energy required to transfer an electron from the Fermi level to vacuum. The work functions of the filament and rods had to be considered because the electron kinetic energy is defined as the difference surface potential [17]. The electron kinetic energy is calculated as the dc bias (ECD offset – filament offset) + 1.75, which is the difference in work functions between the filament and the rods.

The electron kinetic energy is manipulated by varying the trap offset and maintaining a constant filament offset. The electron kinetic energy was set to 1.25 eV for ECD experiments and 7 eV for HECD experiments.

An increase in electron flux from the filament at higher electron energies results in a decrease in activation time required for parent ion depletion when using HECD. The electron flux is monitored via measurement of the electron current through the ECD_{LIT}. Current measurements are performed by applying a positive dc potential to the rods of the ion guide and measuring the current as the electrons collided with the ion guide.

The electrons are pulsed into the ECD_{LIT} by a dc potential applied to a lens between the filament and ECD_{LIT}. This lens, called the electron gate, is typically held at a negative potential to prevent electrons from entering except during the set activation period, during which it is held at a positive potential. Electron transmission through the ECD_{LIT} is aided by the 150 mT neodymium permanent magnet surrounding the LIT, as shown in Figure 2.4. The magnetic field is aligned along the central axis and radially confines the electrons in tight helices, creating efficient overlap between ions and electrons.
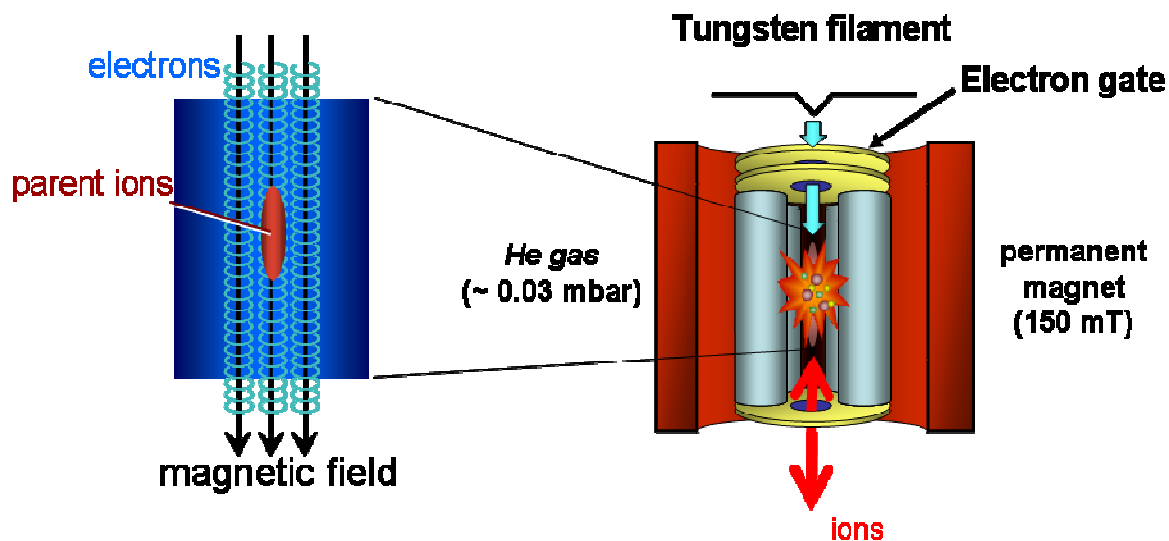
Figure 2.4 Schematic of ECD$_{LIT}$ specifying magnetic field orientation along the central axis and the electron path through the ECD$_{LIT}$.

2.3.2 IR activation and AI-ECD methods

To perform activated-ion ECD (AI-ECD), IR photons are used to activate the ions in the ECD$_{LIT}$. To effect ion activation, ion-photon overlap is crucial. To this end, the IR laser is focused along the central axis of the ECD$_{LIT}$, collinear with the electron beam. IR photons are provided by an unattenuated Synrad 25W CO$_2$ laser that is reflected off of two 90° gold mirrors and focused through a ZnSe lens prior to entering the vacuum housing through a BaF$_2$ window, shown in Figure 2.5. The lens is positioned such that the focal point coincided with the center of the ECD$_{LIT}$.
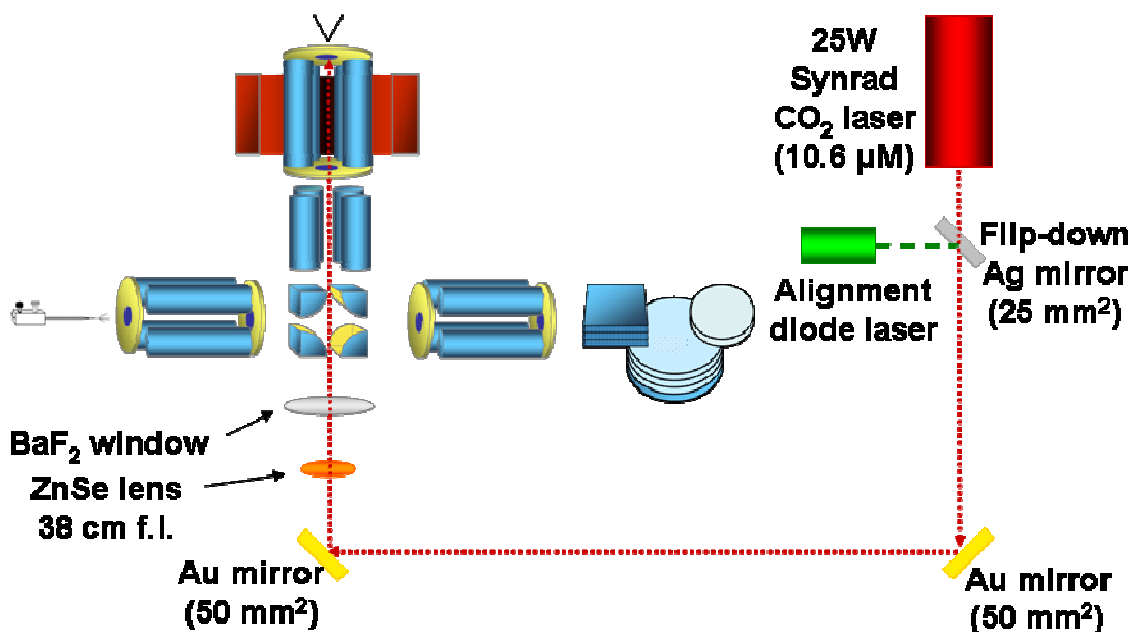
Figure 2.5 Orientation of CO_2 laser with respect to LIT-TOF

Alignment outside the vacuum housing is achieved using a green diode laser aligned collinearly with the CO_2 laser via a 90° silver flip-down mirror. Inside the vacuum housing, infrared multiphoton dissociation (IRMPD) of the peptide leucine enkephalin (YGGFL) is used to confirm laser alignment. In order to achieve efficient IRMPD, the bath gas pressure is reduced to ~0.005 mbar to limit collisional cooling of the ions via energy transfer to the bath gas. Because of the loss of collisional damping due to reduced bath gas pressure, the rf voltage is increased to radially confine the ion cloud closer to the center of the ECD_{LIT}. A second confirmation of laser alignment is an increase in measured electron current from the filament when the laser was on. The increase in electron flux with centered laser alignment is due to the increase in temperature of the filament which increases the number of thermionic electrons emitted. The laser is controlled by a TTL pulse from the ECD_{LIT} control computer which determined the length of the laser pulse.

For AI-ECD experiments, the IR activation was used either sequentially to or simultaneously with electron irradiation. For sequential AI-ECD, the laser pulse is applied before (IR/ECD) or after (ECD/IR) electron irradiation with no delay between the two activation steps. These two methods activate the parent and product ions, respectively. The IR activation was varied from 5 to 50 ms for an electron irradiation time of 5 ms. For simultaneous activation (ECD+IR), the ions are irradiated with electrons and photons during the same period thereby activating both the parent and product ions. Simultaneous activation was applied for a maximum time of 50 ms. IR activation resulted in the dissociation of only noncovalent interactions.

2.3.3 Collisional activation in the ECD_{LIT}

The ECD_{LIT} was modified to allow collisional activation of the trapped ions. A supplemental ac voltage is applied to one pair of rods of the quadrupole to create a dipolar field, as shown in Figure 2.3. Ion isolation is achieved by scanning the frequency of the supplemental ac voltage to eject ions out of the ECD_{LIT}. To selectively activate a single ion, a supplemental rf voltage resonant to the ion frequency is applied [18]. The rf voltage is also used to gently excite the ions with low kinetic energy collisions.

2.4 Ion-molecule reaction: radical peptides with oxygen

Reactions between radical ions and molecular oxygen were used to probe radical reactivity. These ion-molecule reactions took place in the LIT_{therm} after ion activation. In the initial experiments, oxygen gas was leaked into the LIT_{therm} to increase the partial pressure oxygen for the reaction [19]. However, the presence of high concentrations of oxygen severely shortened the lifetime of the tungsten filament making this configuration not practical. It was noticed that there was enough oxygen in the ambient air within the

instrument from the nESI source to effect the ion-molecule reaction if the ions were trapped for a period of time in the LIT_{therm}.
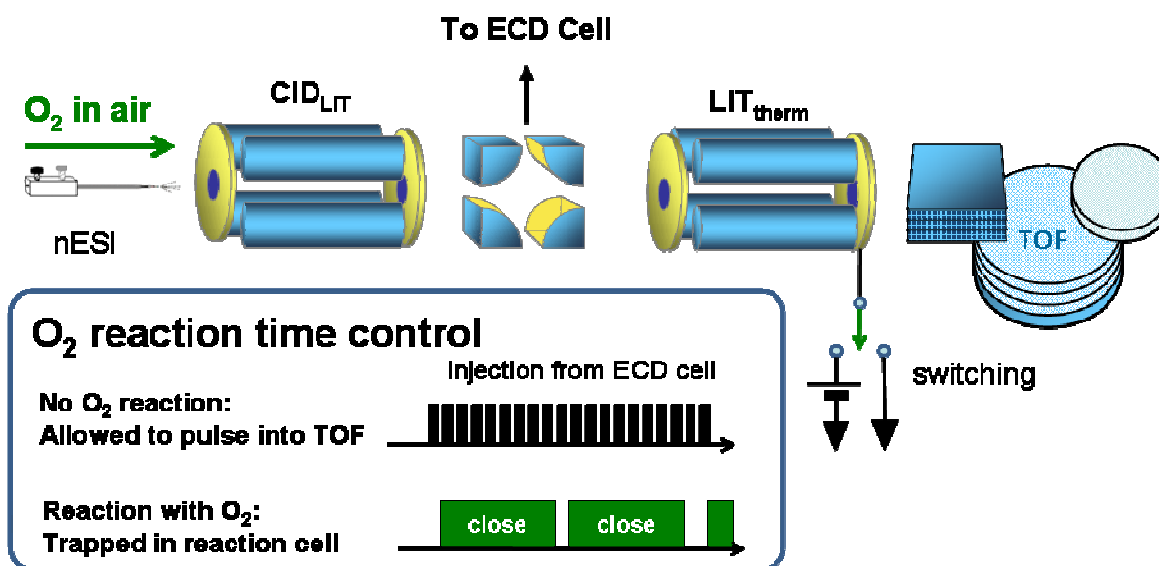
Figure 2.6 Ion-molecule reaction in LIT_{therm}. The potential applied to the back lens of the LIT_{therm} to trap the ions is lengthened to allow reaction time with ambient oxygen from the nESI source.

The LIT-TOF was modified so that the potential applied to the back lens of the LIT_{therm} could be lengthened to trap the ions for reaction with oxygen (Figure 2.6). Under conditions where no reaction with oxygen is desired, the LIT_{therm} acted under standard operating conditions with the back lens pulsing the beam of ions into the orthogonal TOF where they are again pulsed for mass analysis. When the ion-molecule reaction is desired, the time that the dc potential is applied to the back lens is lengthened to prevent the ions from being pulsed into the TOF analyzer. The potential on the back lens of the LIT_{therm} is applied as a number of ion packets pulsed into the LIT_{therm} from the ECD_{LIT} before the ions are allowed into the TOF for mass analysis. For ion-molecule reactions between radicals and oxygen, the ions were trapped in the LIT_{therm} for ten ion packet injections. Due to multiple injections of ion packets into the LIT_{therm}, a defined reaction time cannot be determined since the entire population did not have the same reaction time.

2.5 Summary

The prototype Nanofrontier LIT-TOF with the modifications discussed provides a unique instrument capable of multiple types of ion activation. The LIT-TOF is capable of performing ECD, HECD, AI-ECD, IRMPD, and CID within a single LIT. Other types of experiments not used in this work include electron detachment dissociation, which studies the interactions of anions with low kinetic energy electrons, and electron ionization dissociation, which uses high kinetic energy electrons to induce dissociation in cations. The custom software to run the ECD_{LIT} provides precise control over the ion manipulation and activation. This LIT-TOF is a unique and powerful tool for the analysis of peptides and proteins.

2.6 References

1.   Zubarev, R.A., N.L. Kelleher, and F.W. McLafferty Electron Capture Dissociation of Multiply Charged Protein Cations. A Nonergodic Process. *J. Am. Chem. Soc.* **1998,** *120,* 3265-3266.

2.   Cooper, H.J., K. Hakansson, and A.G. Marshall The Role of Electron Capture Dissociation in Biomolecular Analysis. *Mass Spectrometry Reviews.* **2005,** *24,* 201 - 222.

3.   Baba, T., Y. Hashimoto, H. Hasegawa, A. Hirabayashi, and I. Waki Electron Capture Dissociation in a Radio Frequency Ion Trap. *Anal. Chem.* **2004,** *76,* 4263-4266.

4.   Hoffmann, E.d. and V. Stroobant, *Mass Spectrometry: Principles and Applications, 2 ed*. 2002, New York: John Wiley & Sons. 407.

5.   Marshall, A.G., C.L. Hendrickson, and G.S. Jackson Fourier Transform Ion Cyclotron Resonance Mass Spectrometry: A Primer. *Mass Spectrometry Reviews.* **1998,** *17,* 1-35.

6.   Senko, M.W. and F.W. McLafferty Mass-Spectrometry of Macromolecules - Has Its Time Now Come. *Annu. Rev. Biophys. Biomolec. Struct.* **1994,** *23,* 763-785.

7.   Dunbar, R.C., J.H. Chen, and J.D. Hays Magnetron Motion of Ions in the Cubical Icr Cell. *International Journal of Mass Spectrometry and Ion Processes.* **1984,** *57,* 39-56.

8.   Satake, H., H. Hasegawa, A. Hirabayashi, Y. Hashimoto, and T. Baba Fast Multiple Electron Capture Dissociation in a Linear Radio Frequency Quadrupole Ion Trap. *Anal. Chem.* **2007,** *79,* 8755-8761.

9.   Hashimoto, Y., H. Hasegawa, and I. Waki Dual linear ion trap/orthogonal acceleration time-of-flight mass spectrometer with improved precursor ion selectivity. *Rapid Commun. Mass Spectrom.* **2005,** *19,* 1485-1491.

10.   Siuzdak, G., *The Expanding Role of Mass Spectrometry in Biotechnology*. 2003, San Diego: MRC Press.

11.   Silivra, O.A., F. Kjeldsen, I.A. Ivonin, and A.R. Zubarev Electron Capture Dissociation of Polypeptides in a Three-Dimensional Quadrupole Ion Trap: Implementation and First Results. *J. Am. Soc. Mass Spectrom.* **2005,** *16,* 22 - 27.

12.   Zubarev, R.A. Electron-Capture Dissociation Tandem Mass Spectrometry. *Current Opinion in Biotechnology.* **2004,** *15,* 12 - 16.

13.   Tsybin, Y.O., J.P. Quinn, O.Y. Tsybin, C.L. Hendrickson, and A.G. Marshall Electron Capture Dissociation Implementation Progress in Fourier Transform Ion Cyclotron Resonance Mass Spectrometry. *J. Am. Soc. Mass Spectrom.* **2008,** *19,* 762 - 771.

14.   Tsybin, Y.O., C.L. Hendrickson, S.C. Beu, and A.G. Marshall Impact of Ion Magnetron Motion on Elecron Capture Dissociation Fourier Transform Ion Cyclotron Resonance Mass Spectrometry. *Int. J. Mass Spectrom.* **2006,** *255-256,* 144-149.

15.   Hashimoto, Y., I. Waki, K. Yoshinari, T. Shishika, and Y. Terui Orthogonal trap time-of-flight mass spectrometer using a collisional damping chamber. *Rapid Commun. Mass Spectrom.* **2005,** *19,* 221-226.

16.   Moore, J.H., C.C. Davis, and M.A. Coplan, *Building Scientific Apparatus, 4 ed*, ed. A.B. Progam. 2009, Boulder, Co: Westview Press.

17.   Bushey, J.M., *Improvements in Electrospray Ionization Source Design and Advances in Tandem Mass Spectrometry*, in *Chemistry*. 2008, University of North Carolina: Chapel Hill. p. 186.

18.   Bushey, J.M., T. Baba, and G.L. Glish Simultaneous Collision Induced Dissociation of the Charge Reduced Parent Ion during Electron Capture Dissociation. *Anal. Chem.* **2009,** *81,* 6156-6164.

19.   Baba, T., T. Greene, and G.L. Glish. *Electron Capture Dissociation de novo sequencing by C- and Z- terminal fragment discrimination using neutral-radical reaction*. in *57th ASMS Conference on Mass Spectrometry and Allied Topics*. 2009. Philadelphia, Pa.

Chapter 3

Simultaneous and Sequential Activated-Ion Electron Capture Dissociation

3.1 Introduction

Electron capture dissociation (ECD) tandem mass spectrometry (MS/MS) is

commonly used for protein identification because ECD results in extensive backbone

cleavage with the retention of labile groups such as small-molecule post-translational

modifications [1-5]. Noncovalent interactions also remain intact during ECD, and the

retention of these interactions limits the application of ECD for the analysis of large proteins

[6]. Intact noncovalent interactions prevent the separation of product ions after backbone

cleavage resulting in a complex of the product ions [7-9]. The product ion complex appears

as the charge-reduced species ($[M+nH]^{(n-1)+\bullet}$) in the MS/MS spectrum where electron capture

reduces the charge, but the mass stays the same. The charge-reduced species is often the

most abundant product ion formed during ECD, which can be problematic because the

charge-reduced species provides no additional information about the parent ion [2, 3, 10, 11].

The charge-reduced species can capture additional electrons, further reducing the charge with

no change in the mass of the ion. Multiple electron capture by the charge-reduced species

followed by product ion separation results in c'-/$z^\bullet$-type product ions that vary by shifts of

one dalton from the expected mass-to-charge ratio. These shifts in mass are due to the

presence of neutralized hydrogen atoms from multiple electron capture by the dissociating

species [12, 13]. The mass of the c'-/$z^\bullet$-type product ions can also be shifted by one dalton

due to hydrogen atom transfer from the c'-ion to the $z^\bullet$-ion in the product ion complex to

form the c•- and z′-ions [5, 14, 15]. The shift in the product ion mass by a dalton creates

overlap in the isotopic distribution of the ions, e.g., the monoisotopic peak of the heavier ion

occurs at the same mass-to-charge ratio as the peak for the ^{13}C isotope of the lighter ion. The

shift in the masses of the c′-/z•-type product ions increases the complexity of the spectrum

and can reduce product ion identification due to the overlap in isotopic distributions.

Because of the possibility of multiple electron capture and the subsequent spectral

complication, a highly abundant charge-reduced species is undesirable in protein

identification.

To increase the applicability of ECD for intact protein analysis, activated-ion ECD

(AI-ECD) was developed in which a vibrational excitation technique is used in conjunction

with ECD to disrupt the intramolecular noncovalent interactions [6]. Activation of the parent

ions prior to ECD induces structural unfolding so that when backbone cleavage occurs, the

product ions immediately separate instead of being held together in a product ion complex.

Detection of all product ions formed during ECD can be achieved by activation of the ions

after backbone cleavage. Simultaneous vibrational activation with ECD disrupts the

noncovalent interactions of both the parent and product ions.

The vibrational excitation techniques used for AI-ECD have ranged from collisional

activation of the parent ions prior to ECD [6, 16, 17] to increasing the temperature of the

reaction chamber for thermal denaturation of the parent ions [10, 18, 19] and also IR

activation of the parent ions sequentially to or simultaneously with ECD [7, 14, 20-23]. Each

of these techniques has led to increased product ion formation and reduction of the

abundance of the charge-reduced species [2].   To date, AI-ECD techniques have mostly been

carried out in Fourier transform ion cyclotron resonance (FTICR) mass spectrometers [8]. A

single exception is the performance of simultaneous ECD and collision induced dissociation (CID) in a linear ion trap (LIT) in which targeted collisional activation was used to disrupt noncovalent interactions in the charge-reduced species [12]. Application of vibrational excitation for AI-ECD experiments has proved to be challenging in a FTICR. To activate the ions with collisions, a bath gas is typically leaked into the system and must be removed prior to analysis [24, 25]. Thermal denaturation of the ions is difficult as the heating and cooling of the ICR cell takes minutes to hours thereby lengthening the experiment time. IR activation is the simplest activation technique to implement on a FTICR mass spectrometer and is therefore the most widely used of the vibrational activation techniques for AI-ECD.

The incorporation of an IR laser into a FTICR system has its own difficulties, mostly in the alignment of the laser beam through the ICR cell to ensure sufficient ion-electron-photon overlap. Prior to the application of the hollow cathode electron source for ECD, either the laser or the electron beam had to be aligned off-axis through the ICR cell [22, 26, 27]. It has been shown that in this configuration, the laser and electron beams do not overlap with the ions at the same point in the magnetron motion path of the ions [28], so truly simultaneous AI-ECD is impossible. The incorporation of the hollow cathode electron source into the FTICR allowed the IR and electron beams to be aligned along the same central axis through the ICR cell [29]. In the initial configuration, the electron beam maintained the ring-shaped electron distribution through the ICR cell resulting in limited overlap between the ions and electrons. The ion-electron overlap can be improved with off-resonance excitation, but this excitation resulted in a subsequent reduction in ion-photon overlap [9]. By placing the hollow cathode dispenser in the magnetic fringe field, the electron beam could be compressed in the middle of the ICR cell resulting in overlap of ions,

electrons, and photons. However, this setup posed difficulties such as remote mounting of the electron source and the high power requirements [27]. Each of the previous instrumental configurations have the laser and the electron source on the same side of the ICR cell, and each has associated difficulties in the achievement of ion-electron-photon overlap. The overlap of ions, electrons, and photons was achieved with the laser and electron beams entering the ICR cell from opposite ends, but this configuration required the complicated set up incorporating a mirror mounted on a pneumatic probe to focus the IR laser through the ion-optical elements into the ICR cell [9]. In general, AI-ECD experiments using a FTICR have required long activation times (100-800 ms) due to inefficient overlap of ions, photons, and electrons [9, 28].

As described in Chapter 2, an alternative to performing ECD in a FTICR uses a LIT as the reaction chamber [30]. This LIT has been incorporated into a hybrid linear ion trap / time-of-flight (LIT-TOF) mass spectrometer and has been modified to incorporate IR laser activation of the ions resulting in efficient AI-ECD. The effects of simultaneous and sequential IR activation on the c'-/$z^{\bullet}$-type product ion abundances and sequence coverage in ECD MS/MS are demonstrated using ubiquitin and melittin.

3.2 Experimental

3.2.1 Samples and methods

The peptide leucine enkephalin (YGGFL), the peptide substance P (RPKPQQFFGLM), the amidated peptide melittin (GIGAVLKVLTTGLPALISWIKRKRQQ-NH$_2$), and the protein bovine ubiquitin were purchased from Sigma-Aldrich, Inc. (St. Louis, MO) and used without further purification. Solutions were prepared at a concentration of 5 μM in 50/50 v/v acetonitrile:water with 1%

acetic acid added to aid in the electrospray process. Melittin and ubiquitin were used to study the effects of IR activation sequentially to and simultaneously with ECD. Details of laser alignment and AI-ECD methods were described in Chapter 2.

3.2.2 Data analysis

Product ions were identified and confirmed using the program described in Chapter 2. To test the effects of IR activation, the product ion formation, product ion abundance, and sequence coverage were monitored. The analysis program output the data for product ion formation and abundance. Sequence coverage was used to represent the extent of backbone cleavage and was defined as the percentage of inter-residue cleavages observed. To calculate the sequence coverage, the number of inter-residue cleavages observed was divided by the number of possible inter-residue cleavages. For example, a hypothetical pentapeptide with two charges is shown in Figure 3.1. If ECD of this pentapeptide yields the c_1^+, c_2^+, c_3^+, and $z_3^{+\bullet}$ product ions, the sequence coverage is calculated to be 75% because backbone cleavage occurred at three of the four inter-residue locations to form product ions. No further information is gained in the comparison of the c_2^+ and a $z_3^{+\bullet}$ product ions of this pentapeptide because both ions arise from the dissociation of the same backbone bond (between residues B and C). Therefore, the presence of overlapping product ions, such as the c_2^+ and $z_3^{+\bullet}$ ions in this example, counted as a single inter-residue cleavage in the determination of sequence coverage.

Figure 3.1 ECD of example peptide ABCDE yielding the c_1, c_2, c_3, and z_3 product ions.

3.3 Results and Discussion

3.3.1 Overlap of ions, electrons, and photons

ECD was performed on the +2 charge state ion of substance P yielding a series of

c'-type and $a^{\bullet}$-type product ions, as shown in Figure 3.2.a. The dissociation efficiency for

ECD of $[sub\ P]^{2+}$ was calculated to be 19% which is greater than what was previously

reported [12] and still within the range of conversion efficiency reported for FTICR-MS [2].

Efficient ECD of substance P confirms overlap between electrons and ions in the ECD_{LIT}.

Infrared multiphoton dissociation (IRMPD) was performed on the +1 charge state ion

of leucine enkephalin (YGGFL) producing b-type, a-type, and rearrangement ions, as shown

in Figure 3.2.b. For this experiment, the helium bath gas pressure was decreased by an order

of magnitude to reduce collisional cooling of the ions which hampers the efficiency of

IRMPD [31]. Also, the rf voltage applied to the ECD_{LIT} was increased relative to the ECD

experiment to radially confine the ions in the center of the trap. Increased rf voltage was

required to compensate for the decreased collisional damping of the ion cloud to the center of

the trap resulting from the decreased bath gas pressure. Under these conditions, the

dissociation efficiency for IRMPD of leucine enkephalin was 21%, and the formation of

product ions typical to IRMPD confirms overlap of ions and photons in the ECD_{LIT}. These

experiments demonstrate the efficient overlap between ions, electrons, and photons in the
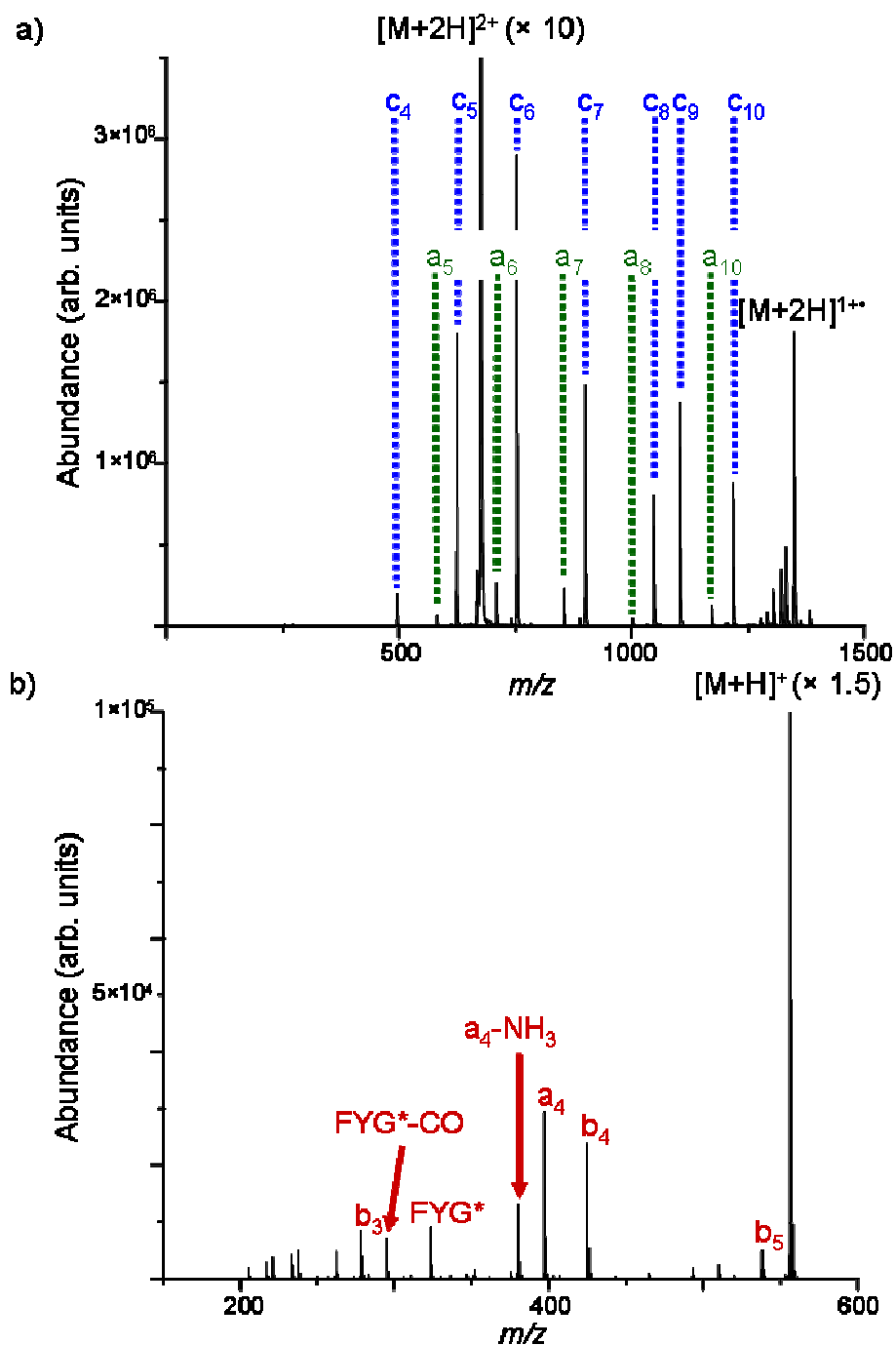
ECD_{LIT}.

Figure 3.2 a) ECD (25 ms) of the +2 charge state ion of substance P b) IRMPD (25 ms) of singly charged leucine enkephalin ion at reduced bath gas pressure. Rearrangement ions are indicated with an asterisk.

3.3.2 Sequential AI-ECD in a LIT-TOF

IR activation was applied sequentially to ECD using the +8 and +12 charge state ions of ubiquitin to demonstrate the behavior of different extents of noncovalent interactions. As will be discussed in Chapter 4, lower charge states have more extensive noncovalent interactions than higher charge states due to the difference in Coulombic repulsion between charge sites [32, 33]. For IR activation of the ions prior to ECD (IR/ECD), the IR irradiation was varied between 0 and 50 ms prior to an electron irradiation time of 5 ms. When using IR activation after ECD (ECD/IR), an electron irradiation time of 5 ms was followed by IR irradiation varied from 0 to 50 ms. No delay period was used in between the two activation steps resulting in a maximum activation time of 55 ms. The effects of IR activation on product ion formation and abundance from ECD for the +12 charge state of ubiquitin are shown in Figure 3.3. The plots on the left (a and c) correspond to IR activation prior to electron irradiation for 5 ms. The plots on the right (b and d) correspond to IR activation after electron irradiation for 5 ms. For each plot, the data were classified by which type of backbone bond was cleaved, thus dividing it into three categories: a-/x-, b-/y-, and c-/z-ions. The product ion abundance is the summed abundances of the product ions classified by which backbone bond was broken, e.g., all c'-type and $z^{\bullet}$-type abundances are summed because these product ions result from the dissociation of the N-C_{α} bond. As expected for ECD, the c'-/$z^{\bullet}$-type product ions occur in the highest numbers and abundance. It was observed that both IR/ECD and ECD/IR increased the formation and abundance of c'-/$z^{\bullet}$-type product ions.
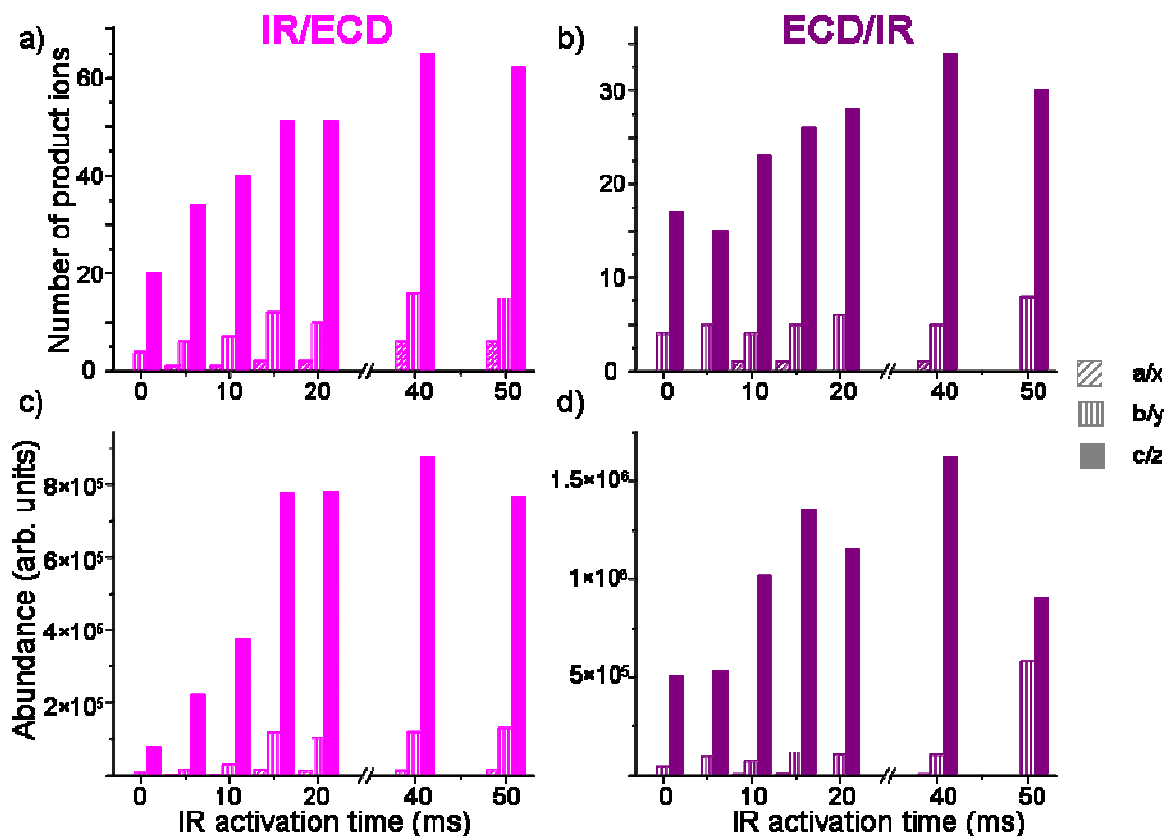
Figure 3.3 Sequential IR-ECD of the +12 charge state ion of ubiquitin. The top plots are the number of product ions formed from IR/ECD (a) and ECD/IR (b) as a function of IR activation time. The bottom plots are the product ion abundances formed from IR/ECD (c) and ECD/IR (d) as a function of IR activation time. IR activation was performed with an electron irradiation time of 5 ms. The number of ions formed and product ion abundances are classified by the type of backbone bond broken.

The increase in the formation of product ions led to an increase in sequence coverage, as shown in Figure 3.4. The sequence coverage for the +8 and +12 charge state ions of ubiquitin increased with the addition of IR activation prior to or after electron irradiation for 5 ms. Longer IR activation times led to greater sequence coverage for both charge states. The sequence coverage is lower for the +8 charge state compared with the +12 charge state of ubiquitin. The decreased sequence coverage for the lower charge state is due multiple reasons: the electron capture cross section is lower for ions with fewer charges [5, 13]; backbone dissociation is known to occur near charge sites, so fewer charge sites results in

less extensive backbone cleavage [34]; and higher charge states have decreased noncovalent

interactions due to the increased Coulombic repulsions between charge sites [35].
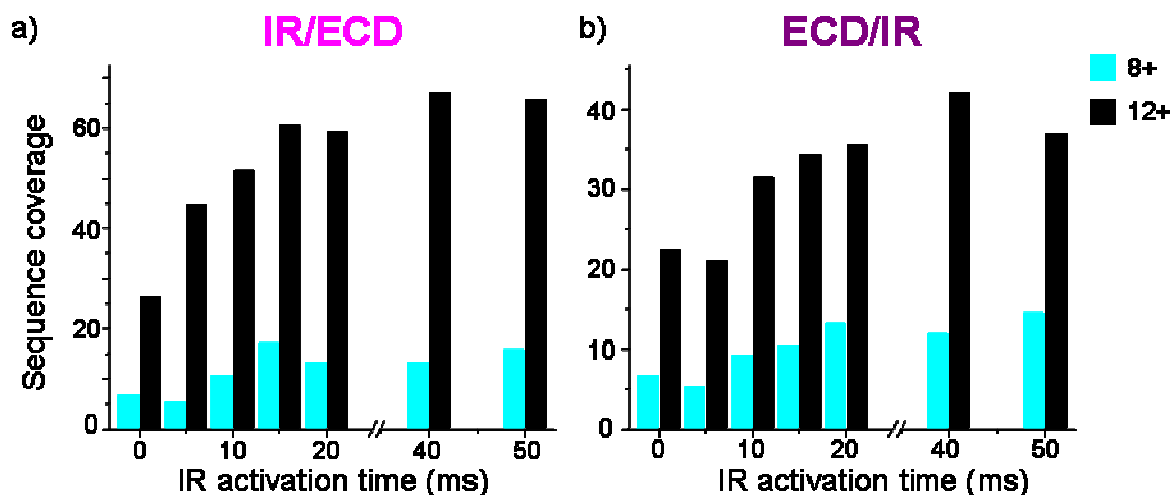
Figure 3.4 Sequence coverage of the +8 and +12 charge state ions of ubiquitin using (a) IR/ECD and (b) ECD/IR with electron irradiation for 5 ms.

Both of these methods resulted in newly observed backbone cleavage sites from those

product ions that were held together in the charge-reduced species, and these product ions led

to increases in sequence coverage. The summed product ion abundances increased for two

reasons: the formation of new ions and the increased abundance of previously observed ions.

Both of the reasons result from the disruption of noncovalent interactions. In these

experiments, the c'-type and $z^{\bullet}$-type product ions specific to ECD exhibited significant increases in abundance and formation as IR irradiation times were increased. The c'-/$z^{\bullet}$-type product ions exhibited these effects because IRMPD of ubiquitin was limited due to the high bath gas pressure so only product
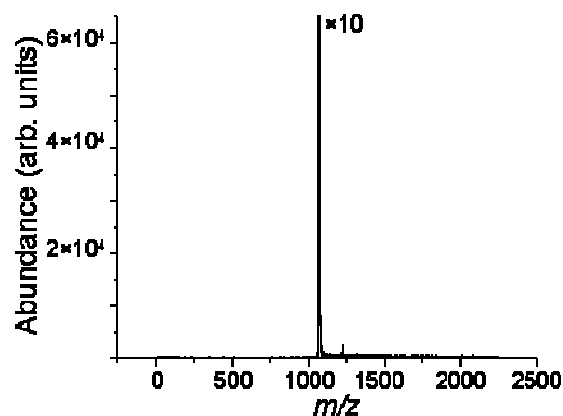
Figure 3.5 IR irradiation for 60 ms of the +8 charge state of ubiquitin.

55

ions from ECD were formed. The inefficacy of IRMPD at these pressures is shown in Figure

3.5 where the +8 charge state ion of ubiquitin was irradiated with IR photons for 60 ms and

yielded no product ions. These results show that the addition of IR activation sequential to

ECD increases the abundance and formation of c′-/z•-type product ions.

3.3.3 Simultaneous AI-ECD in a LIT-TOF

Simultaneous AI-ECD (ECD+IR) was performed on the +7 through +12 charge state

ions of ubiquitin for times varying from 5 to 30 ms. In Figure 3.6, MS/MS spectra from

ECD (left) and ECD+IR (right) for each charge state ion are shown. For a single charge state

ion, ECD+IR yields an increase in product ion abundance and formation resulting from the

decrease in the abundances of the parent ion and the charge-reduced species.
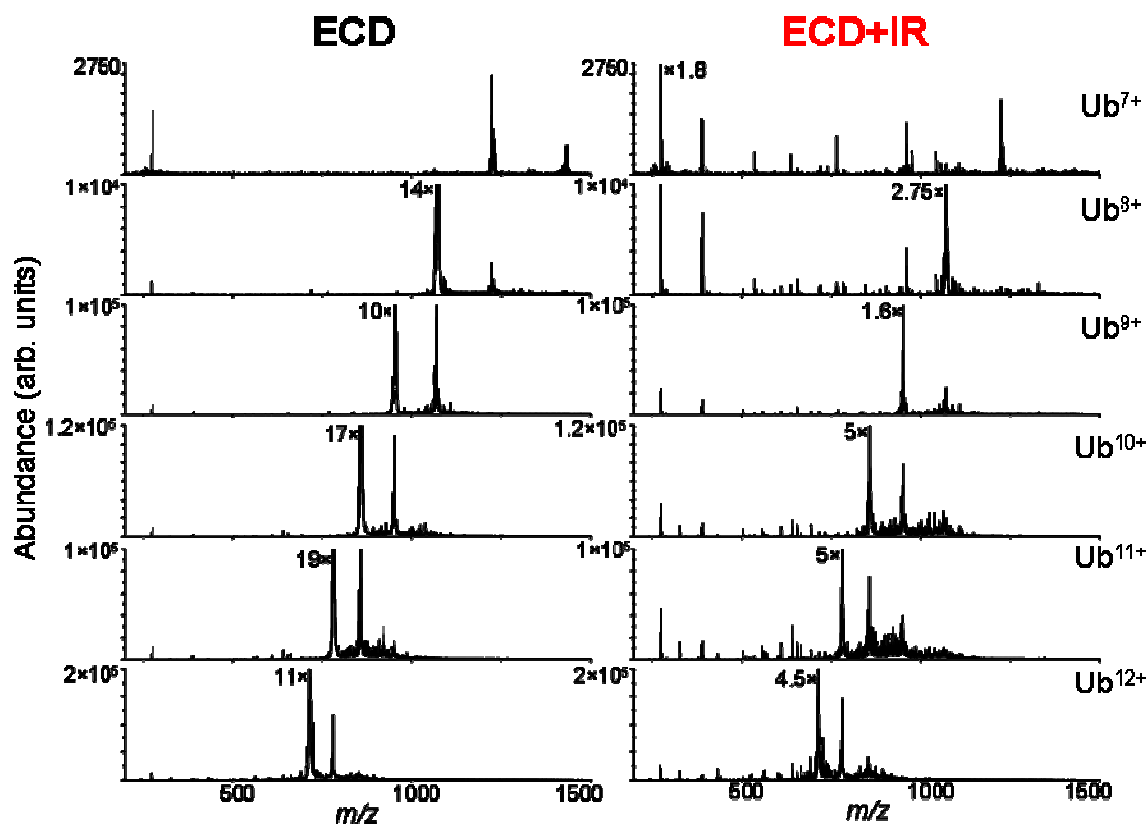
Figure 3.6 MS/MS spectra of each of the charge state ions of ubiquitin from +7 through +12
dissociated using ECD (left) or ECD+IR (right) for 20 ms.

It is also worth noting that the increase in product ion formation with the concomitant decrease in parent ion and charge-reduced species occurred for all activation times. In Figure 3.7, MS/MS spectra of the +8 charge state of ubiquitin formed using ECD and ECD+IR are shown for activation times ranging from 5 to 30 ms. As the activation time was increased, the abundance of the parent ion and charge-reduced species decreased. The decrease in the abundances of the parent ion and charge-reduced species was accompanied by an increase in product ion formation. For all activation times, the addition of IR activation decreased the abundance of the parent ion and charge-reduced species more than conventional ECD. Therefore, the product ion abundances were greater in the ECD+IR MS/MS spectra. The maximum effective activation time is limited by depletion of the parent ion. After parent ion depletion, large product ions are reduced to smaller product ions through secondary electron capture and backbone dissociation. Large product ions are affected more so than small product ions due to the increased charge state of the large product ions and therefore increased electron capture cross section [5, 13]. Activation of the large product ions can produce smaller product ions of the same type or lead to the formation of internal product ions. For example, dissociation of a c_{25}^{4+} product ion can dissociate between the ninth and tenth residue to form the c_9 ion and an internal ion that is a truncated $z^{\bullet}$-ion which encompasses residues 10 through 25. The reduction of large product ions to small ions decreases the amount of information in the MS/MS spectrum through the absence of large product ions and the formation of internal product ions which complicates ion identification.
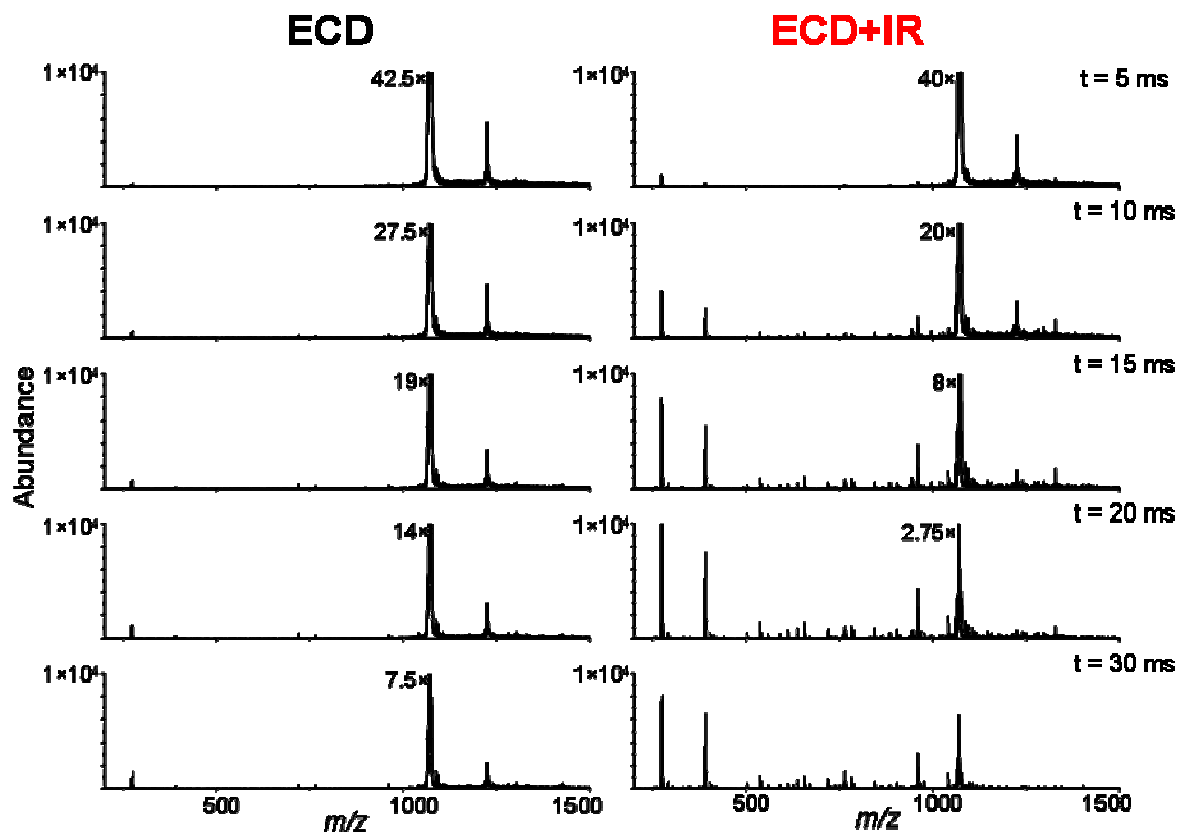
Figure 3.7 ECD and ECD+IR MS/MS spectra of the +8 charge state ion of ubiquitin at activation times ranging from 5 to 30 ms.

ECD+IR increased the number of product ions observed and the abundances of these product ions. Unlike sequential AI-ECD, ECD+IR increased the appearance and abundance of all three classes of product ions (Figure 3.8).
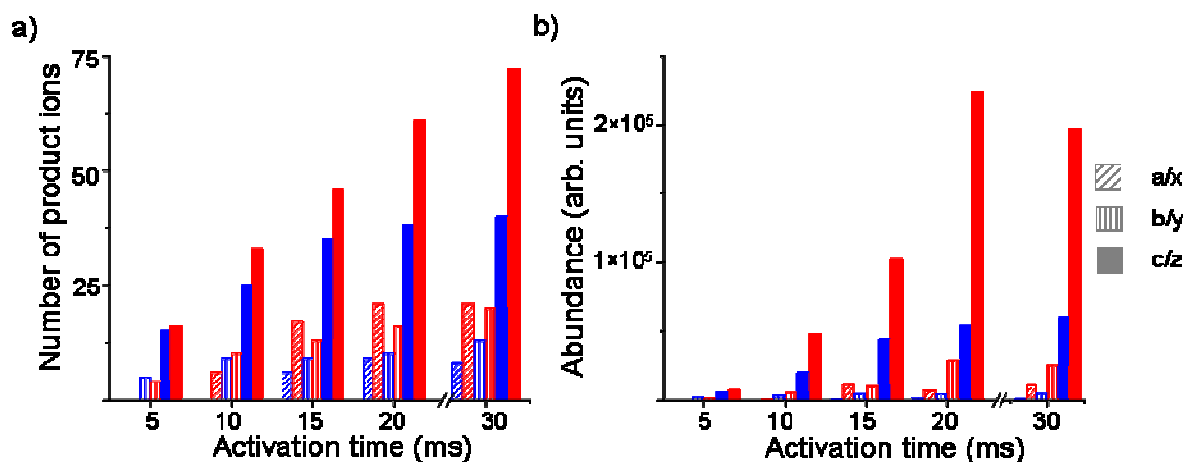
Figure 3.8 Product ion analysis for ECD (blue) and ECD+IR (red) of the +12 charge state ion of ubiquitin. The number of product ions formed (a) and the abundance of the product ions (b) were classified by the type of backbone bond cleaved and plotted as a function of activation time.

Further analysis of the types of product ions formed from ECD+IR revealed that the increase in the a-/x-type ions was predominantly due to new a-type ions, and the increase in the b-/y-type ions was due to an increase of y-type ions. The appearance of these ions was expected because a·- and y-type ions are known to result from a secondary dissociation mechanism following electron capture [36]. The prevalence of the a·- and y-type product ions increases with increase in parent ion kinetic energy [37]. Re-evaluation of the sequential AI-ECD data revealed that the formation of a·- and y-type ions was increased for IR/ECD and not for ECD/IR. The increased appearance of a·- and y-type ions for ECD+IR and IR/ECD confirms that increased parent ion internal energy results in a greater population of parent ions dissociating by the minor ECD pathway.

The increase in product ion formation and abundance led to an increase in sequence coverage for all charge states. As expected, longer activation times led to increased sequence coverage for both ECD and ECD+IR with the maximum in sequence coverage observed at either 20 or 30 ms for each charge state (Figure 3.9).
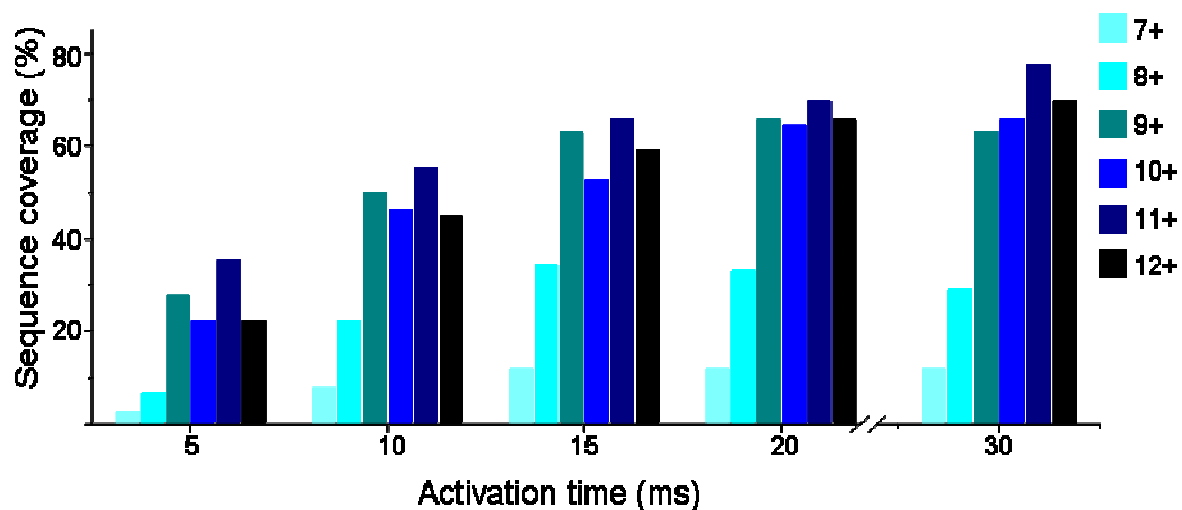
Figure 3.9 Sequence coverage for the +7 through the +12 charge state ions of ubiquitin from ECD+IR as a function of activation time.

The relative increase in sequence coverage due to the incorporation of IR activation was greatest for the lower charge states, with the sequence coverage for the +7 charge state increasing by 8-fold with the addition of IR activation, as seen in Figure 3.10. In this figure, the percent increase in sequence coverage using ECD+IR compared to conventional ECD is plotted for each of the charge state ions studied at each activation time used. The addition of IR activation simultaneously with ECD has a greater effect on the lower charge states than
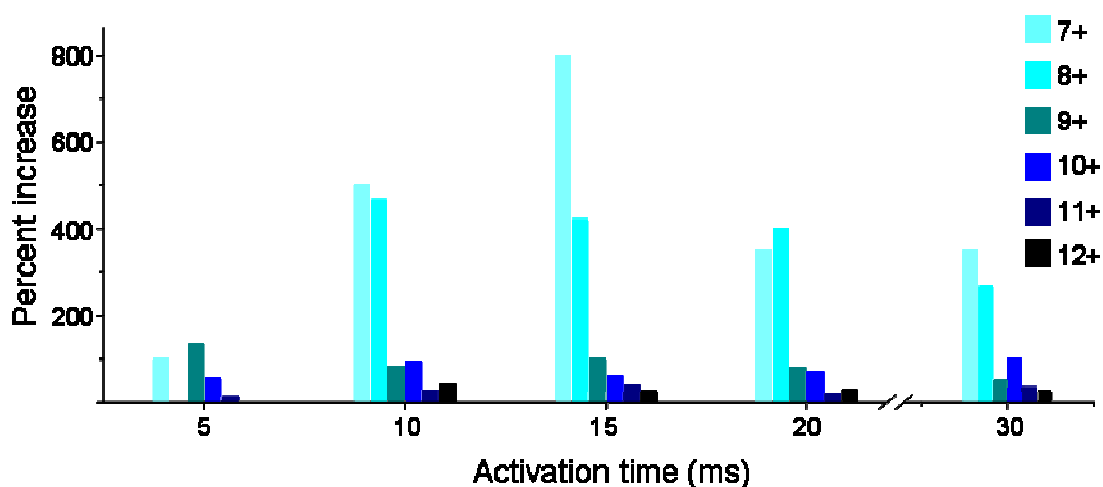
Figure 3.10 Percent increase in sequence coverage of each charge state ion of ubiquitin studied.

60

the higher charge states because of the increased prevalence of noncovalent interactions in the lower charge states. The +7 and +8 charge states showed the greatest response to the addition of IR activation. The +9 through +12 charge state ions of ubiquitin each showed significantly less response to IR activation. The drastic change in response between the lower and higher charge state ions of ubiquitin can be explained by differences in structure. The +7 and +8 charge state ions of ubiquitin have been shown to have smaller collision cross sections and multiple gas-phase conformations indicative of a more compact structure [38]. The +9 through the +13 charge state ions have been assigned an elongated structure based on ion mobility measurements and hydrogen-deuterium exchange [39]. High field asymmetric ion mobility spectrometry (FAIMS) has also shown that the +9 through the +12 charge state ions of ubiquitin have similar conformations [38].

ECD+IR was used to analyze the +4 charge state ion of melittin. Similar to what was observed with ubiquitin, there were increases in the number of c'-/$z^\bullet$-type product ions and the abundances of these ions which increased the sequence coverage of melittin, as seen in Figure 3.11. Different from ubiquitin, the addition of IR irradiation increased the abundance and formation of only the c'-/$z^\bullet$-type product ions. Also, the addition of IR activation did not have as great a relative increase in sequence coverage for melittin as was observed with ubiquitin. The difference in the increase of sequence coverage is most likely due
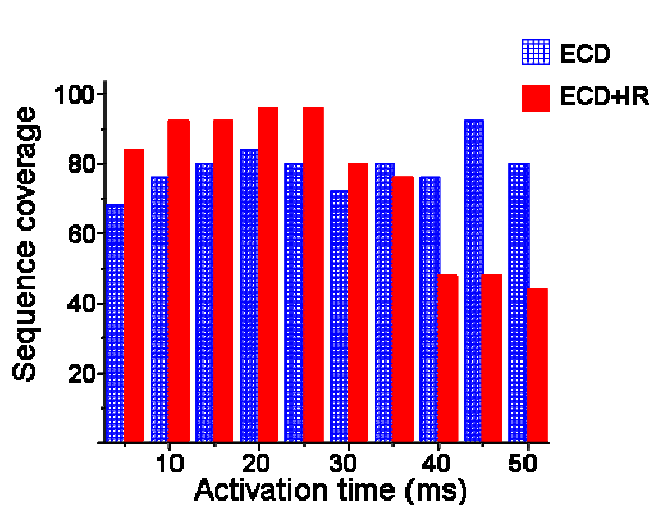
Figure 3.11 Sequence coverage of the +4 charge state ion of melittin using ECD and ECD+IR.

to the difference in size between melittin and ubiquitin, 26 residues compared to 76. The disparity in size inherently results in a difference in noncovalent interactions with there being fewer interactions in melittin compared to ubiquitin.

The extent of tertiary noncovalent interactions is related to the gas-phase structure. More extended structures, i.e., structures that are unfolded and relatively linear, have fewer tertiary noncovalent interactions. The ratio of charge state to dalton has been proposed as a way to measure the extent of unfolding in a gas-phase protein [40]. The +4 charge state of melittin has a charge/dalton ratio approximately equal to that of the +12 charge state of ubiquitin which indicates an unfolded structure with limited noncovalent interactions for both ions. However, it has been shown that both the +12 charge state of ubiquitin and melittin have extensive noncovalent interactions because they adopt helical structures in the gas phase [41, 42]. Both of these ions should behave similarly, but the smaller increase in sequence coverage for ECD+IR of the +4 charge state ion of melittin stems from the differences in size and the reduction of noncovalent interactions.

Aside from laser alignment configuration, another difference between AI-ECD using IR activation in a FTICR and the ECD_{LIT} is the presence of a helium bath gas. The bath gas pressure has been calculated to be on the order of 10^{-2} mbar in the ECD_{LIT} which is approximately eight orders of magnitude greater than required for high resolution in an ICR cell [43, 44]. The higher bath gas pressure results in faster collisional cooling rates in the ECD_{LIT} which decreases the effect of IR activation on the molecule [31]. Because of lower pressures, and therefore lower collisional cooling rates, IR activation is more effective in an ICR cell than in the ECD_{LIT}. However, this apparent advantage of ICR cells is negated by inefficient overlap between ions and photons in conventional AI-ECD instrumental

configurations [28]. IR activation, even at standard operating pressures in the ECD_{LIT}, is sufficient to disrupt noncovalent interactions in gas phase protein ions, as evidenced by the results from the use of ECD+IR.

ECD+IR has been shown to increase the formation and abundance of the c'-/$z^{\bullet}$-type product ions typical to ECD. Similar to sequential AI-ECD, the addition of IR irradiation disrupts the noncovalent interactions allowing product ions to separate and be observed but not enough activation to induce dissociation via IRMPD. The IR activation, though decreased by higher collisional cooling rates compared to FTICR mass spectrometers, is sufficient to enhance product ion detection when combined with ECD.

3.3.4 Comparison of AI-ECD techniques

Thus far, three AI-ECD methods utilizing IR activation have been shown to increase product ion formation and abundances compared to conventional ECD. A comparison of the three AI-ECD methods with conventional ECD is shown in Figure 3.12. The left plot is the sequence coverage, and the right plot is the summed abundance of the c'-/$z^{\bullet}$-type product ions as a function of activation time for the +8 charge state ion of ubiquitin. For the sequential methods, electron irradiation of 5 ms was used, and the period of IR activation is the total activation time less 5 ms.
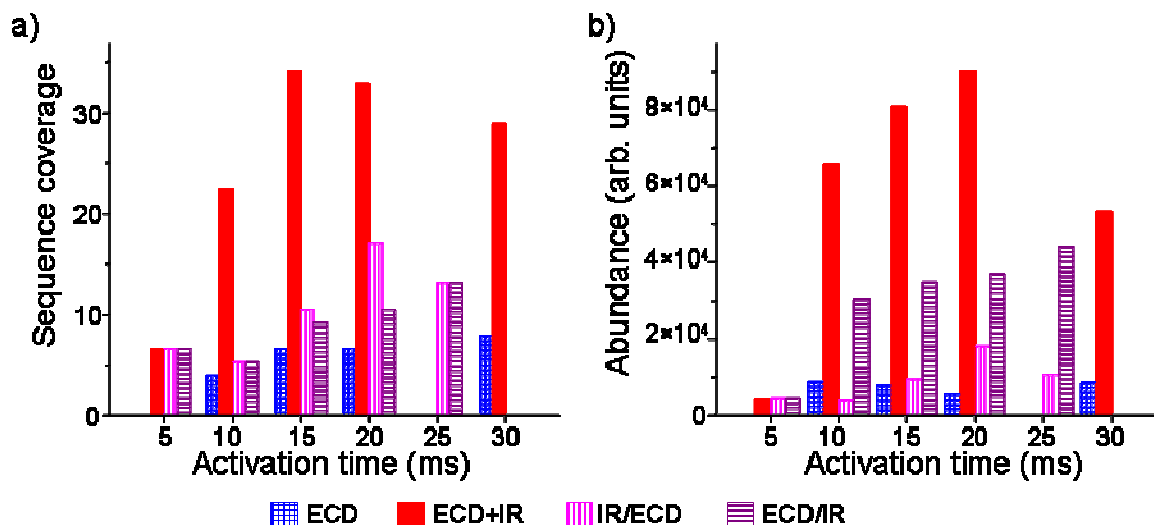
Figure 3.12 Comparison of ECD and AI-ECD results for the +8 charge state ion of ubiquitin. Sequential techniques used an electron irradiation time of 5 ms. a) Sequence coverage and b) product ion abundance plotted as a function of activation time

These data confirm that IR activation increases the information content of the MS/MS spectra formed using ECD; however it is evident that ECD+IR yielded the greatest improvement. The sequence coverage was improved with ECD+IR nearly over twice that of ECD, IR/ECD, and ECD/IR. It is also apparent that the length of activation need not be increased appreciably to observe improvements in product ion formation with a maximum observed around 15 to 20 ms. By effecting greater dissociation than ECD, ECD+IR could be combined with liquid chromatography in a high-throughput proteomics method where conventional ECD is currently used [2, 45]. At activation times greater than 5 ms, ECD+IR produced the greatest c'-/$z^\bullet$-type ion abundance indicating that ECD+IR is the most sensitive of the AI-ECD techniques. ECD+IR has implications of improved protein identification and analysis due to the greatest increase in sequence coverage and c'-/$z^\bullet$-type product ion abundance of the four techniques studied.

3.3.5 IR activation or increased electron flux?

Aside from ion activation, a second effect was observed during ECD+IR: an increase in the measured electron current through the ECD_{LIT}. Because the laser is aligned such that it is centered on the electron filament, the laser irradiation increases the temperature of the filament resulting in increased thermionic electron emission [8]. Electron kinetic energy was not affected because it is determined by the dc potential difference between the filament and the rods of the ECD_{LIT}, but the flux of electrons was increased during ECD+IR. The increase in formation of the c'- and $z^{\bullet}$-type product ions could be the result of both IR activation and increased electron flux. However, increased c'-/$z^{\bullet}$-type product ion formation resulting from sequential AI-ECD suggests that IR activation, not increased electron flux, causes the observed results. To determine the effect of IR activation, two experiments were performed to separate the results due to the increased electron flux and the IR activation.

In the first experiment, the laser was shifted to travel slightly off-axis through the ECD_{LIT}. Because the laser is focused along the central axis of the ECD_{LIT}, the focal point in the center of the cell should not shift, only the path that the laser travels. To perform this experiment, the mirror that reflects the laser to the lens was translated horizontally so that the laser traveled from the center to the edge of the aperture into the ECD_{LIT} (Figure 2.5), which resulted in a translation of approximately 2 mm (Figure 3.13). During this translation, IRMPD of leucine enkephalin was used to monitor ion-photon overlap.
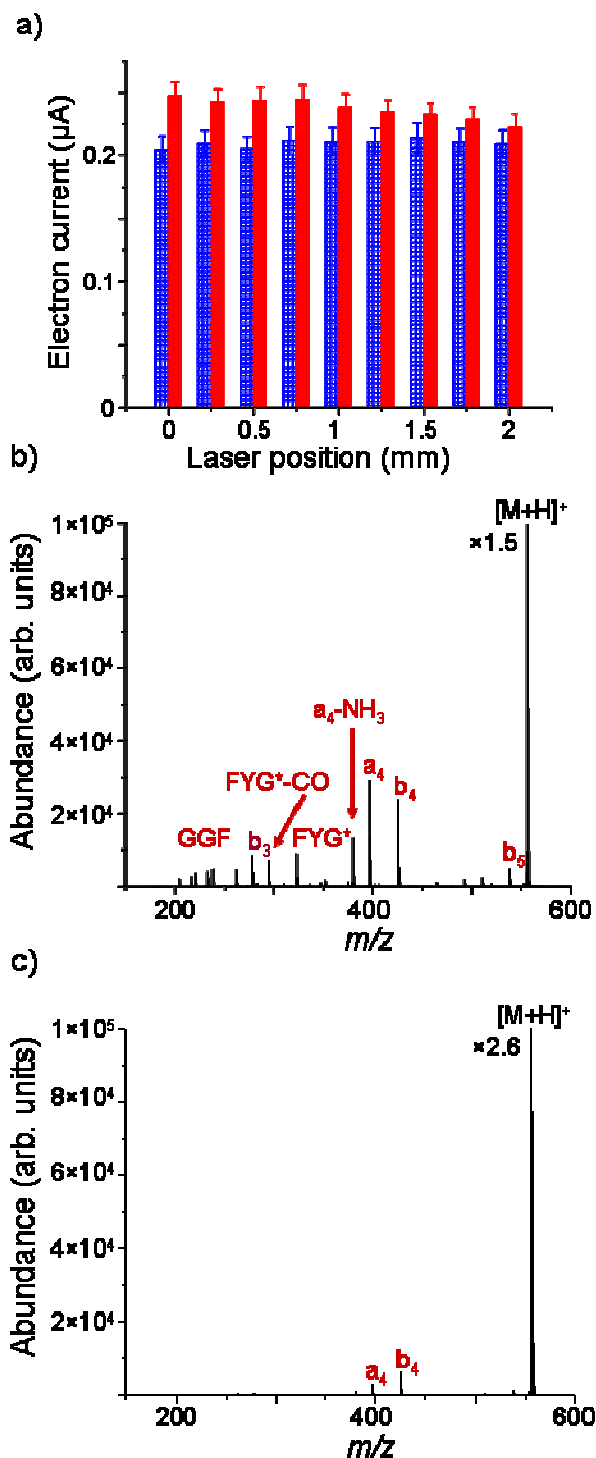
Figure 3.13 a) Electron current for ECD and ECD+IR at various laser positions. A position of 3 mm is centered b) IRMPD for 25 ms of YGGFL with the laser centered through the ECD_{LIT}. c) IRMPD for 25 ms of YGGFL with the laser 2 mm off-axis.

The electron flux through the ECD_{LIT} was measured for each of the laser positions (Figure 3.13.a). The electron flux was monitored by measuring the current on the ion guide. The electron current was measured, and the difference in electron current between ECD and ECD+IR decreased as the laser was translated away from center. Decreased current was expected because as the laser was moved off-axis, it would no longer hit the filament and cause increased electron emission. The abundance and formation of IRMPD products decreased substantially as the laser was translated away from the center (Figure 3.13.b) to the edge (Figure 3.13.c). At the most extreme position, very few product ions were formed, and there was a consequent increase in parent ion abundance. The decrease in IRMPD products highlights the importance of a centered laser position for ion-photon overlap in the ECD_{LIT}. The translation of

the laser was intended to maintain sufficient ion-photon overlap for IR activation and reduce filament heating thus eliminating the increased electron flux. However, laser translation resulted in the loss of efficient ion-photon overlap, so this experiment was unable to separate the effects of IR activation and increased electron flux.

To achieve efficient activation of the ions with IR photons, the laser must be centered through the ECD_{LIT}. In this configuration, the increase in electron emission due to increased filament temperature is inevitable. To test the extent of product ion formation and abundance as a result of IR activation with ECD compared to increased electron flux, the +4 charge state ion of melittin was studied (Figure 3.14). To monitor the dissociation due to increased electron flux, the power supplied to the filament was increased to match the electron current observed during ECD+IR (ECD_{hi}). Increasing the potential drop across the filament increased the electron flux without affecting the electron energy because the potential difference between the filament and the ECD_{LIT} was kept constant.
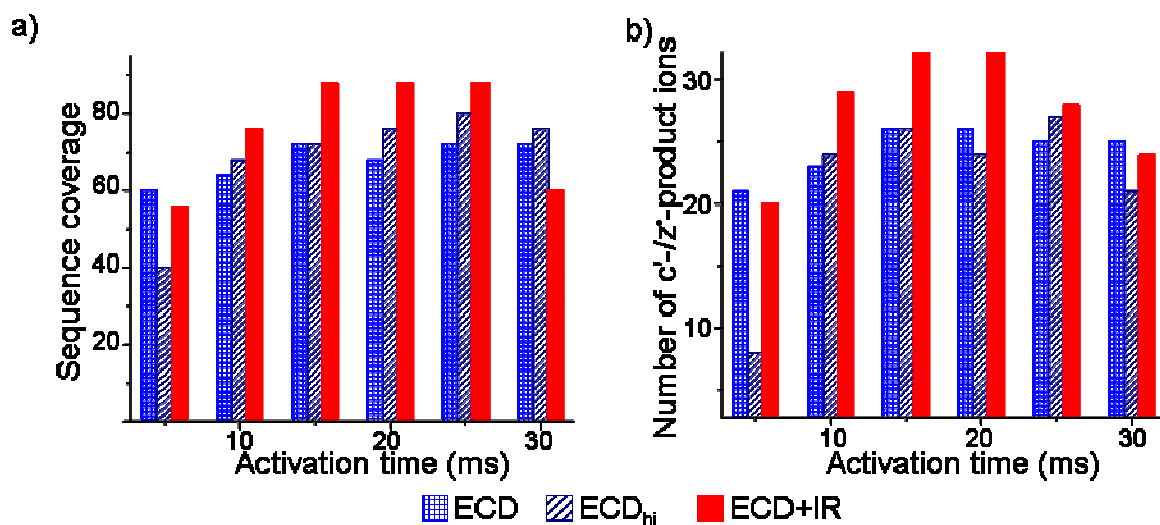
Figure 3.14 Comparison of sequence coverage (a) and c'-/$z^•$-product ion formation (b) from ECD, ECD+IR, and ECD at an electron current matched to ECD+IR (ECD_{hi}). The techniques were performed using the +4 charge state ion of melittin.

Sequence coverage was improved for both ECD+IR and ECD_{hi} (Figure 3.14.a), but IR activation resulted in higher sequence coverage for ECD+IR than ECD_{hi} at most activation times. Sequence coverage was decreased for the longest activation time (30 ms) due to the dissociation of large product ions to smaller product ions. The increase in sequence coverage for ECD_{hi} resulted from the formation of new y-type product ions. There was not much difference in the summed product ion abundance for c'-/$z^\bullet$-type product ions between ECD+IR and ECD_{hi}, but the number of c'-/$z^\bullet$-type product ions was increased for ECD+IR compared to ECD_{hi} (Figure 3.14.b). These results show that increased electron flux results in increased product ion abundance, but IR activation is necessary for the formation and observation of new c'-/$z^\bullet$-type product ions.

It is hypothesized that the IR activation disrupts the noncovalent interactions of the charge-reduced species allowing product ions to separate and be detected thus increasing sequence coverage and preventing multiple electron capture which complicates the spectrum. To test this hypothesis, the +4 charge state ion of melittin was dissociated using ECD, ECD+IR, and ECD_{hi}, and the abundances of the parent ion ($[M+4H]^{4+}$), the charge-reduced species ($[M+4H]^{3+\bullet}$), and the doubly charge-reduced species ($[M+4H]^{2+}$) were monitored (Figure 3.15).
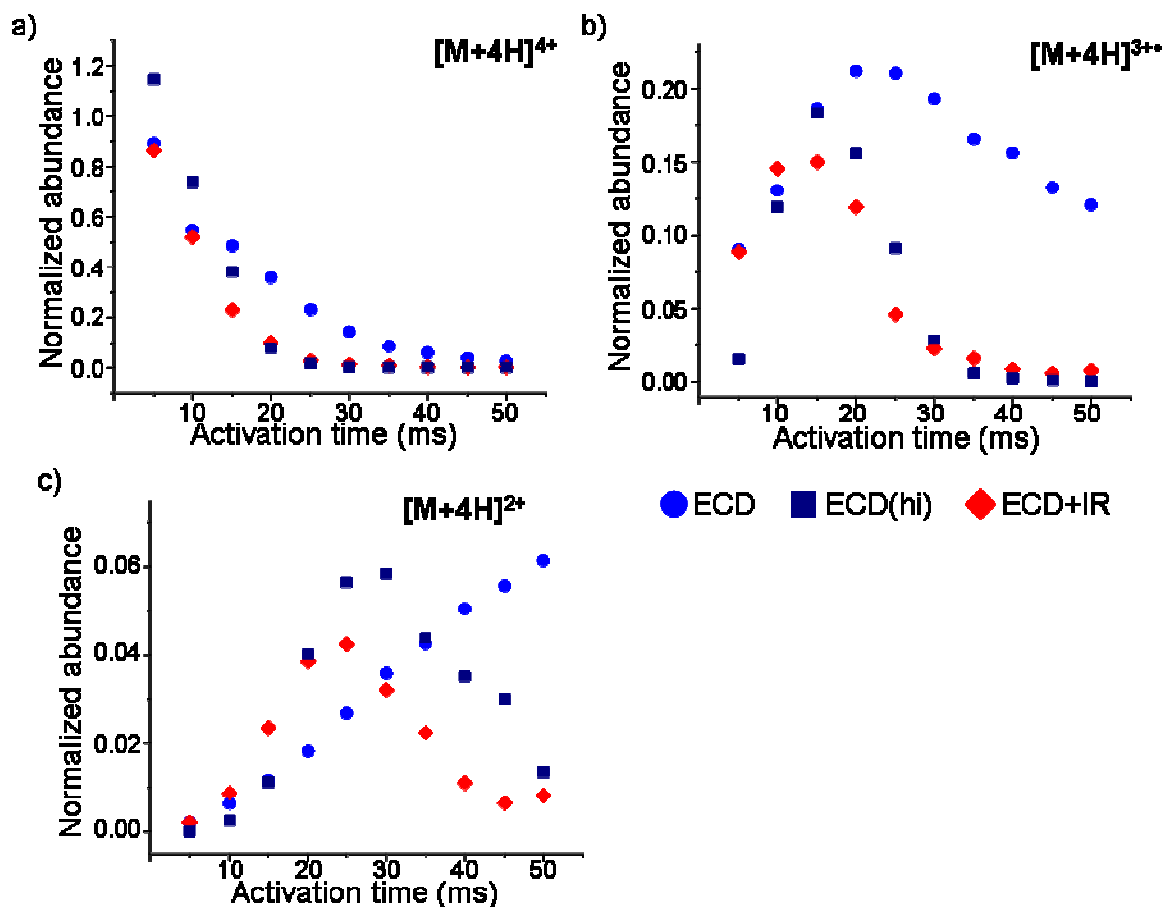
Figure 3.15 Normalized abundance of the parent ion (a), singly charge-reduced species (b), and the doubly charge-reduced species (c) as a function of activation time. The ions were normalized to the abundance of the inactivated parent ion, the +4 charge state of melittin.

The parent ion abundance for ECD+IR and ECD$_{hi}$ decreased at the same rate which was at a faster rate than observed for conventional ECD. The exponential decay of the parent ion abundance for ECD, ECD+IR, and ECD$_{hi}$ indicates that the rate of electron capture has a first-order dependence on the population of electrons. The decay of the abundances of the charge-reduced species and doubly charge-reduced species was faster for both ECD+IR and ECD$_{hi}$ compared with ECD. In ECD$_{hi}$, the abundances of the charge-reduced species and the doubly charge-reduced species were decreased due to dissociation into product ions and capture of additional electrons. The increased electron flux resulted in an increase in the electron population which in turn increased the probability of interaction between multiply

69

charged cations and electrons. As the rate of electron capture is dependent on the number of electrons, the increase in the number of electrons for ECD_{hi} results in increased electron capture rates for all species. The increase in the rate of decay indicates that while the electron capture cross section is dependent on the square of the charge [13], the rate of electron capture is dependent on the electron capture cross section and the electron flux.

IR activation decreased the abundances of the charge-reduced species and the doubly charged-reduced species through a combination of increased electron flux and the disruption of noncovalent interactions resulting in product ion separation. The effects of IR activation were noticeable in the abundances of the charge-reduced species and the doubly charge-reduced species. The general trend of a slight increase followed by a sharp decrease was observed for each technique, but the declines in the abundances required less activation time for the ions formed using ECD+IR. The faster decay of electron capture product ions for ECD+IR compared with ECD_{hi} shows that the increased electron flux is not solely responsible for the results observed during ECD+IR. IR activation reduces the probability of multiple electron capture by reducing the abundance of the charge-reduced species through the disruption of noncovalent interactions.

3.4 Summary and conclusions

AI-ECD using IR activation sequentially to and simultaneously with electron capture has been implemented on a recently developed LIT-TOF instrument. Efficient overlap of ions, electrons, and photons was confirmed, and the benefits of IR/ECD, ECD/IR, and ECD+IR were demonstrated using multiple charge state ions of the protein ubiquitin. Incorporation of IR activation in conjunction with ECD resulted in improved sequence coverage and the formation and abundance of c'-/$z^{\bullet}$-type product ions. Simultaneous IR

activation had greater effects for lower charge states than higher charge states due to the increase in intramolecular noncovalent interactions which prevent product for lower charge state ions. The dissociation of melittin was used to determine whether IR activation or increased electron flux was responsible for the increase in c'-/$z^{\bullet}$-type product ions. It was ascertained that IR activation was necessary for the formation of new c'-/$z^{\bullet}$-type product ions. ECD+IR was possible due to efficient overlap of ions, photons, and electrons, which was easily implemented in the ECD_{LIT}. The results from IR activation with ECD, increased c'-/$z^{\bullet}$-type product ion formation and increased product ion abundance leading to improved sequence coverage, have implications for improved protein identification.

3.5 References

1. Bakhtiar, R. and Z. Guan Electron Capture Dissociation Mass Spectrometry in Characterization of Peptides and Proteins. *Biotechnology Letters*. **2006,** *28,* 1047-1059.

2. Cooper, H.J., K. Hakansson, and A.G. Marshall The Role of Electron Capture Dissociation in Biomolecular Analysis. *Mass Spectrometry Reviews*. **2005,** *24,* 201 - 222.

3. Zubarev, R.A. Reactions of Polypeptide Ions with Electrons in the Gas Phase. *Mass Spectrometry Reviews*. **2003,** *22,* 57 - 77.

4. Zubarev, R.A., N.L. Kelleher, and F.W. McLafferty Electron Capture Dissociation of Multiply Charged Protein Cations. A Nonergodic Process. *J. Am. Chem. Soc.* **1998,** *120,* 3265-3266.

5. Zubarev, R.A., K.F. Haselmann, B. Budnik, F. Kjeldsen, and F. Jensen Towards an Understanding of the Mechanism of Electron-Capture Dissociation: A Historical Perspective and Modern Ideas. *European Journal of Mass Spectrometry*. **2002,** *8,* 337-349.

6. Horn, D.M., Y. Ge, and F.W. McLafferty Activated Ion Electron Capture Dissociation for Mass Spectral Sequencing of Larger (42 kDa) Proteins. *Anal. Chem.* **2000,** *72,* 4778-4784.

7. Oh, H.B. and F.W. McLafferty A Variety of Activation Methods Employed in "Activated-Ion" Electron Capture Dissociation Mass Spectrometry: A Test against Bovine Ubiquitin 7+ Ions. *Bulletin of the Korean Chemical Society*. **2006,** *27,* 389 - 394.

8. Bushey, J.M., *Improvements in Electrospray Ionization Source Design and Advances in Tandem Mass Spectrometry*, in *Chemistry*. 2008, University of North Carolina: Chapel Hill. p. 186.

9. Mihalca, R., Y.E.M. van der Burgt, L.A. McDonnell, M. Duursma, I. Cerjak, A.J.R. Heck, and R.M.A. Heeren Combined Infrared Multiphoton Dissociation and Electron-Capture Dissociation using Co-Linear and Overlapping Beams in Fourier Transform Ion Cyclotron Resonance Mass Spectrometry. *Rapid Commun. Mass Spectrom.* **2006,** *20,* 1838-1844.

10. Horn, D.M., K. Breuker, A.J. Frank, and F.W. McLafferty Kinetic Intermediates in the Folding of Gaseous Protein Ions Characterized by Electron Capture Dissociation Mass Spectrometry. *J. Am. Chem. Soc.* **2001,** *123,* 9792-9799.

11. Kruger, N.A., R.A. Zubarev, D.M. Horn, and F.W. McLafferty Electron Capture Dissociation of Multiply Charged Peptide Cations. *Int. J. Mass Spectrom.* **1999,** *185/186/187,* 787-793.

12.   Bushey, J.M., T. Baba, and G.L. Glish Simultaneous Collision Induced Dissociation of the Charge Reduced Parent Ion during Electron Capture Dissociation. *Anal. Chem.* **2009,** *81,* 6156-6164.

13.   Zubarev, R.A., D.M. Horn, E.K. Fridriksson, N.L. Kelleher, N.A. Kruger, M.A. Lewis, B.K. Carpenter, and F.W. McLafferty Electron Capture Dissociation for Stuctural Characterization of Multiply Charged Protein Cations. *Anal. Chem.* **2000,** *72,* 563-573.

14.   Tsybin, Y.O., H. He, M.R. Emmett, C.L. Hendrickson, and A.G. Marshall Ion activation in electron capture dissociation to distinguish between N-terminal and C-terminal productions. *Anal. Chem.* **2007,** *79,* 7596-7602.

15.   Savitski, M.M., F. Kjeldsen, M.L. Nielsen, and R.A. Zubarev Hydrogen Rearrangement to and from Radical z Fragments in Electron Capture Dissociation of Peptides. *J. Am. Soc. Mass Spectrom.* **2007,** *18,* 113 - 120.

16.   Ge, Y., B.G. Lawhorn, M. ElNaggar, E. Strauss, J.-H. Park, T.P. Begley, and F.W. McLafferty Top Down Characterization of Larger Proteins (45 kDa) by Electron Capture Dissociation Mass Spectrometry. *J. Am. Chem. Soc.* **2002,** *124,* 672-678.

17.   Shi, S.D.H., M.E. Hemling, S.A. Carr, D.M. Horn, I. Lindh, and F.W. McLafferty Phosphopeptide/Phosphoprotein Mapping Electron Capture Dissociation Mass Spectrometry. *Anal. Chem.* **2001,** *73,* 19-22.

18.   Breuker, K., H. Oh, D.M. Horn, B.A. Cerda, and F.W. McLafferty Detailed Unfolding and Folding of Gaseous Ubiquitin Ions Characterized by Electron Capture Dissociation. *J. Am. Chem. Soc.* **2002,** *124,* 6407-6420.

19.   Sze, S.K., Y. Ge, H. Oh, and F. McLafferty Top-down mass spectrometry of a 29 kDa protein for characterization of any posttranslational modification to within one residue. *PNAS*. **2002,** *99,* 1774-1779.

20.   Cooper, H.J., M.H. Tatham, E. Jaffray, J.K. Heath, T.T. Lam, A.G. Marshall, and R.T. Hay Fourier transform ion cyclotron resonance mass spectrometry for the analysis of small ubiquitin-like modifier (SUMO) modification: Identification of lysines in RanBP2 and SUMO targeted for modification during the E3 AutoSUMOylation reaction. *Anal. Chem.* **2005,** *77,* 6310-6319.

21.   Zabrouskov, V. and J.P. Whitelegge Increased coverage in the transmembrane domain with activated-ion electron capture dissociation for top-down Fourier-transform mass spectrometry of integral membrane proteins. *Journal of Proteome Research*. **2007,** *6,* 2205-2210.

22.   Lin, C., J.C. Cournoyer, and P.B. O'Connor Probing the Gas-Phase Folding Kinetics of Peptide Ions by IR Activated DR-ECD. *J. Am. Soc. Mass Spectrom.* **2008,** *19,* 780 - 789.

23. Cooper, H.J., J.K. Heath, E. Jaffray, R.T. Hay, T.T. Lam, and A.G. Marshall Identification of sites of ubiquitination in proteins: A Fourier transform ion cyclotron resonance mass spectrometry approach. *Anal. Chem.* **2004,** *76,* 6982-6988.

24. Laskin, J. and J.H. Futrell Activation of Large Ions in FT-ICR Mass Spectrometry. *Mass Spectrometry Reviews.* **2005,** *24,* 135-167.

25. Håkansson, K., M.J. Chalmers, J.P. Quinn, M.A. McFarland, C.L. Hendrickson, and A.G. Marshall Combined Electron Capture and Infrared Multiphoton Dissociation for Multistage MS/MS in a Fourier Transform Ion Cyclotron Resonance Mass Spectrometer. *Anal. Chem.* **2003,** *75,* 3256-3262.

26. Håkansson, K., M.J. Chalmers, J.P. Quinn, M.A. McFarland, C.L. Hendrickson, and A.G. Marshall Combined Electron Capture and Infrared Multiphoton Dissociation for Multistage MS/MS in a Fourier Transform Ion Cyclotron Resonance Mass Spectrometer. *Anal. Chem.* **2003,** *75,* 3256 - 3262.

27. Tsybin, Y.O., J.P. Quinn, O.Y. Tsybin, C.L. Hendrickson, and A.G. Marshall Electron Capture Dissociation Implementation Progress in Fourier Transform Ion Cyclotron Resonance Mass Spectrometry. *J. Am. Soc. Mass Spectrom.* **2008,** *19,* 762 - 771.

28. Mikhailov, V.A. and H.J. Cooper Activated Ion Electron Capture Dissociation (AI ECD) of Proteins: Synchronization of Infrared and Electron Irradiation with Ion Magnetron Motion. *J. Am. Soc. Mass Spectrom.* **2009,** *20,* 763-771.

29. Tsybin, Y.O., M. Witt, G. Baykut, F. Kjeldsen, and P. Hakansson Combined infrared multiphoton dissociation and electron capture dissociation with a hollow electron beam in Fourier transform ion cyclotron resonance mass spectrometry. *Rapid Commun. Mass Spectrom.* **2003,** *17,* 1759-1768.

30. Baba, T., Y. Hashimoto, H. Hasegawa, A. Hirabayashi, and I. Waki Electron Capture Dissociation in a Radio Frequency Ion Trap. *Anal. Chem.* **2004,** *76,* 4263-4266.

31. Black, D.M., A.H. Payne, and G.L. Glish Determination of Cooling Rates in a Quadrupole Ion Trap. *J. Am. Soc. Mass Spectrom.* **2006,** *17,* 932-938.

32. Badman, E.R.H.-H., C. S.; Clemmer, D. E. Monitoring Structural Changes of Proteins in an Ion Trap over 10 - 200 ms: Unfolding Transitions in Cytochrome *c* Ions. *Anal. Chem.* **2001,** *73,* 6000-6007.

33. Myung, S., E. Badman, Y. Lee, and D. Clemmer Structural transitions of electrosprayed ubiquitin ions stored in an ion trap over similar to 10 ms to 30 s. *J. Phys. Chem. A.* **2002,** *106,* 9976-9982.

34. Cerda, B.A., K. Breuker, D.M. Horn, and F.W. McLafferty Charge/Radical Site Initiation versus Coulombic Repulsion for Cleavage of Multiply Charged Ions.

Charge Solvation in Poly(alkene glycol) Ions. *J. Am. Soc. Mass Spectrom.* **2001,** *12,* 565-570.

35.   Budnik, B.A., M.L. Nielsen, J.V. Olsen, K.F. Haselmann, P. Horth, W. Haehnel, and R.A. Zubarev Can relative cleavage frequencies in peptides provide additional sequence information? *Int. J. Mass Spectrom.* **2002,** *219,* 283-294.

36.   Zubarev, R.A., N.A. Kruger, E.K. Fridriksson, M.A. Lewis, D.M. Horn, B.K. Carpenter, and F.W. McLafferty Electron Capture Dissociation of Gaseous Multiply-charged Proteins is Favored at Disulfide Bonds and Other Sites of High Hydrogen Atom Affinity. *J. Am. Chem. Soc.* **1999,** *121,* 2857-2862.

37.   Cooper, H.J., R.R. Hudgins, K. Hakansson, and A.G. Marshall Secondary fragmentation of linear peptides in electron capture dissociation. *Int. J. Mass Spectrom.* **2003,** *228,* 723-728.

38.   Robinson, E.W., R.D. Leib, and E.R. Williams The Role of Conformation on Electron Capture Dissociation of Ubiquitin. *J. Am. Soc. Mass Spectrom.* **2006,** *17,* 1470 - 1480.

39.   Freitas, M.A., C.L. Hendrickson, M.R. Emmett, and A.G. Marshall Gas-phase bovine ubiquitin cation conformations resolved by gas-phase hydrogen/deuterium exchange rate and extent. *Int. J. Mass Spectrom.* **1999,** *185/186/187,* 565-575.

40.   Breuker, K. and M. Tollinger. *Gas-Phase Structures of the Three Helix Bundle Protein KIX Probed by Electron Capture Dissociation.* in *The 58th ASMS Conference on Mass Spectrometry and Allied Topics.* 2010. Salt Lake City, UT.

41.   Oh, H., K. Breuker, S.K. Sze, Y. Ge, B.K. Carpenter, and F.W. McLafferty Secondary and tertiary structures of gaseous protein ions characterized by electron capture dissociation mass spectrometry and photofragment spectroscopy. *PNAS.* **2002,** *99,* 15863-15868.

42.   Kweon, H.K. and K. Hakansson Site-specific amide hydrogen exchange in melittin probed by electron capture dissociation Fourier transform ion cyclotron resonance mass spectrometry. *Analyst.* **2006,** *131,* 275-280.

43.   Hoffmann, E.d. and V. Stroobant, *Mass Spectrometry: Principles and Applications, 2 ed.* 2002, New York: John Wiley & Sons. 407.

44.   Amster, I.J. Fourier Transform Mass Spectrometry. *Journal of Mass Spectrometry.* **1996,** *31,* 1325-1337.

45.   Palmblad, M., Y.O. Tsybin, M. Ramstrom, J. Bergquist, and P. Hakansson Liquid Chromatography and electron-capture dissociation in fourier transform ion cyclon resonance mass spectrometry. *Rapid Commun. Mass Spectrom.* **2002,** *16,* 988-992.

Chapter 4

Activated-Ion Electron Capture Dissociation for Protein Structural Analysis

4.1 Introduction

There are many methods to probe protein higher-order structure, including nuclear

magnetic resonance (NMR) spectroscopy and x-ray crystallography. Mass spectrometry

entered the field of protein structure determination with the development of electrospray

ionization (ESI) and matrix-assisted laser desorption ionization (MALDI) in which large,

nonvolatile complexes can be transferred to the gas phase. In protein analysis, mass

spectrometry offers the advantages of using small amounts of sample at low concentrations

compared with NMR or x-ray crystallography [1, 2].

Tandem mass spectrometry (MS/MS) provides a quick method to analyze the primary

structure of a protein, but the study of higher-order structure remained elusive. The MS/MS

methods commonly used to determine the sequence, collision induced dissociation (CID) and

infrared multiphoton dissociation (IRMPD), are unable to probe secondary or tertiary

structure [3]. CID and IRMPD cause dissociation of ions through the increase of ion internal

energy via low kinetic energy collisions with a bath gas and absorption of multiple IR

photons, respectively. The added internal energy is then distributed throughout the molecule

inducing dissociation of the weakest bonds [4]. Noncovalent interactions, which define the

higher-order structure of the proteins, are typically the weakest bonds and are therefore

broken before backbone cleavage occurs. It has been noted that CID of different

conformations selected by ion mobility spectrometry (IMS) produces similar dissociation

patterns [3]. It was concluded that the different protein conformations convert to a common structure prior to backbone dissociation, indicating a loss of higher-order structure. Other methods utilizing the advantages of mass spectrometry were developed to study protein structure, such as hydrogen-deuterium exchange mass spectrometry (HDXMS) and IMS, as discussed in Chapter 1. Both of these methods provided insight into protein structure, but neither give a complete picture.

In electron capture dissociation (ECD), the noncovalent interactions that define protein structure remain intact after backbone dissociation. As discussed in Chapter 3, the retention of the noncovalent interactions limits the applicability of ECD in the sequence analysis of large proteins. However, due to this same retention of noncovalent interactions, ECD of protein ions can provide higher-order structural information through analysis of the product ion dissociation pattern. The c'-/$z^\bullet$-type product ion distribution formed during ECD has been used to study the structural protection throughout the protein. Product ions formed by backbone cleavage in regions with very little structure will readily separate and be detected. The regions of the protein that are stabilized by higher-order structure will be evidenced by the low abundance of c'-/$z^\bullet$-type product ions because these product ions will be held together by noncovalent interactions after backbone dissociation. ECD has been used to analyze the structural changes dependent on protein charge state [5, 6] as well as structural changes induced by a vibrational unfolding of the protein in the gas phase [5, 7].

Due to the Coulombic repulsion between charge sites and limited charge solvation in the gas phase, protein charge state has a strong influence on the stable gas-phase protein structure [8-10]. IMS studies have shown that the protein cross-section spans from a near-native compact cross-section for lower charge states to a fully extended cross-section

for higher charge states [11-14]. ECD has been used to monitor protein unfolding due to increased charge state. It was found that the relative yield of c'- and $z^{\bullet}$-ions from ECD of ubiquitin correlated well with ion cross-section determined by IMS [5]. Comparison of the dissociation pattern of different charge states was used to determine which noncovalent interactions were disrupted by the increase in protein charge. It was also found that comparison of the ECD product ion dissociation pattern could reveal helical unfolding in the gas-phase structure of the KIX bundle protein resulting from increased charge [6]. These studies show that ECD can be used to monitor the structural stability of a protein ion as a function of increasing charge state.

ECD has also been used to monitor induced unfolding of the protein gas-phase structure by vibrational excitation using IR absorption and thermal denaturation [5, 7]. The use of a vibrational technique to disrupt noncovalent interactions with ECD is termed activated-ion ECD (AI-ECD) [15]. ECD was used to study the kinetic intermediates formed by pulsed IR laser unfolding and refolding in the gas phase of the protein cytochrome c [7]. It was found that regions which underwent structural changes due to IR activation were detected by the increase in formation of c'-/$z^{\bullet}$-type product ions. ECD was also used to monitor the changes in protein structure as a function of thermal denaturation [5]. The ratio of the abundances of the c'-/$z^{\bullet}$-type product ions compared to the abundance of the charge-reduced species, which results from a folded structure, was used to calculate an equilibrium constant for a given temperature. The calculated equilibrium constants were used to derive the overall unfolding enthalpy of each charge state of ubiquitin. Vibrational excitation combined with ECD can be used to probe and manipulate protein structure to understand and characterize protein gas-phase structure. In this work, the gas-phase structure

of ubiquitin was probed using sequential and simultaneous AI-ECD methods in a hybrid

linear ion trap / time-of-flight (LIT-TOF) mass spectrometer. IR activation was used to

disrupt noncovalent interactions, and the structural stability of the protein was monitored

using ECD.

4.2 Experimental

4.2.1 Samples

To monitor protein unfolding in the gas phase, the well-studied protein ubiquitin was

used. Bovine ubiquitin was purchased from Sigma-Aldrich (St. Louis, MO) and used

without further purification. Solutions were prepared at a concentration of 5 μM in 50/50 v/v

acetonitrile/water with 1% acetic acid to aid in the electrospray process. ECD and

simultaneous AI-ECD (ECD+IR) were used to dissociate the +7 through the +12 charge state

ions of ubiquitin. IR activation prior to ECD (IR/ECD) was used to study the structure of the

+12 charge state ion.

4.2.2 Data analysis

Product ions were identified using the data analysis software described in Chapter 2.

To study the unfolding of these protein structures, the abundances of the c'-/$z^•$-type product

ions specific to ECD were monitored. The data were plotted as a function of cleavage site to

illustrate the dependence of product ion formation on location within the protein sequence.

4.3 Results and discussion

4.3.1 IR-induced protein unfolding

Sequential AI-ECD, specifically IR/ECD, increased the abundances and number of

c'-/$z^•$-type product ions via regional structural unfolding. Greater product ion abundance and

increased product ion formation resulted from longer IR activation times. Analysis of the

product ion abundances as a function of cleavage site revealed the regions of the protein that

became unfolded with the addition of IR activation (Figure 4.1)

Figure 4.1 Comparison of the dissociation pattern formed from IR/ECD of the +12 charge state ion of ubiquitin. IR activation times ranged from 0 to 50 ms prior to electron irradiation of 5 ms. The summed abundance of the c'-type ions is represented by the filled cyan bars, and the summed abundance of the $z^{\bullet}$-type ions is represented by the hollow blue bars.

The product ions from ECD increased in abundance and new product ions were

observed as IR activation was increased from 0 to 50 ms for an electron irradiation time of 5

ms. The short time for ECD accentuates the effect of IR activation on protein structure

because limited dissociation was observed with no IR activation. The majority of new

product ions formed were $z^{\bullet}$-type ions, and nearly complete C-terminal sequence coverage

was observed for the longest IR activation times. The appearance of new C-terminal product

ions indicated that IR activation induces unfolding of the C-terminus. The addition of IR

activation increased the formation of c'-ions but not to the same extent of new $z^{\bullet}$-ions. The

limited formation of N-terminal product ions showed increased protection of N-terminus compared with the C-terminus.

A second confirmation of C-terminal unfolding was evident from the product ion distribution formed during ECD+IR. The summed abundances of the c'-type and $z^{\bullet}$-type product ions at each cleavage site from ECD and ECD+IR of the +12 charge states ion of ubiquitin are shown in Figure 4.2.
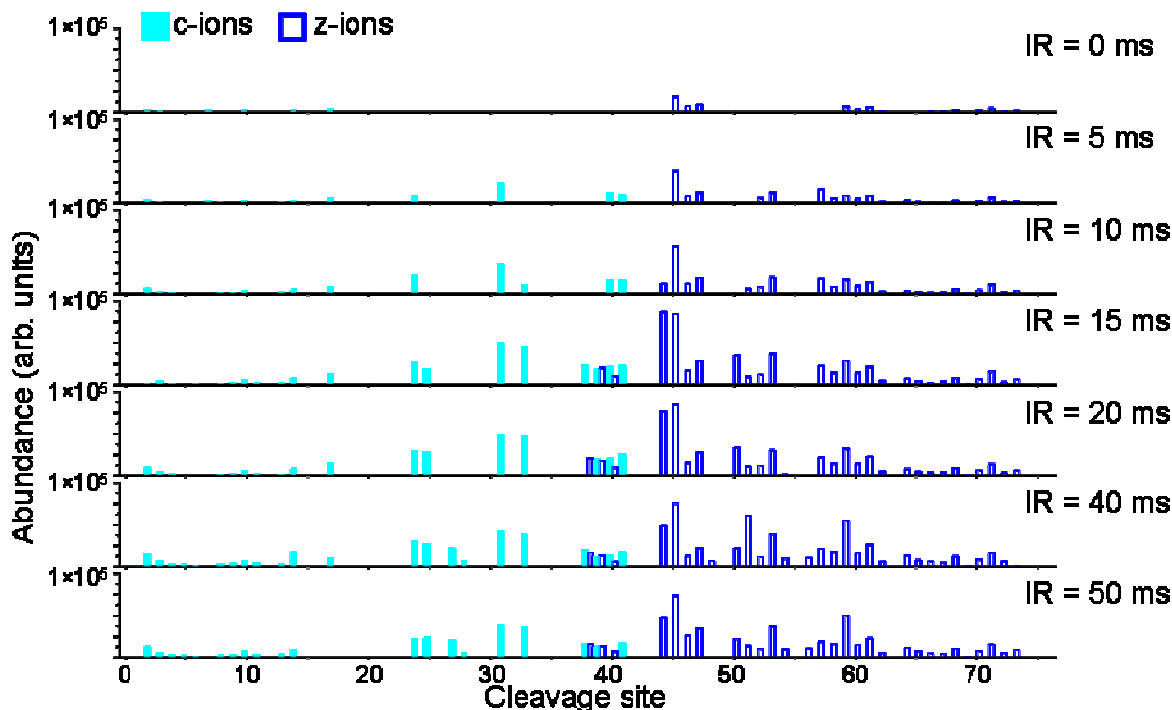

Figure 4.2 Comparison of dissociation pattern formed from ECD and ECD+IR of the +12 charge state ion of ubiquitin for activation times ranging from 5 to 20 ms. The summed abundance of the c'-type ions is represented by the filled cyan bars, and that of the $z^{\bullet}$-type ions is represented by the hollow blue bars.

The addition of IR activation simultaneously with ECD resulted in increase formation of c'- and $z^{\bullet}$-type product ions. The increase in C-terminal product ions confirmed the trend that was observed for IR/ECD and suggests that IR activation induces unfolding of the C-terminus. As can be seen in Figure 4.2, the unfolding of the C-terminus was observed for ECD at long electron irradiation times. However, the abundance of these newly formed

z•-ions was severely reduced to what was observed with ECD+IR. The increase in z•-type

product ion abundance indicates that the C-terminus is unfolding due to IR activation.

The unfolding of the C-terminus with IR activation was observed for multiple charge

state ions of ubiquitin. The summed abundances of the c′-type and z•-type product ions are

each cleavage site from ECD and ECD+IR of the +9 charge state ion of ubiquitin is shown in
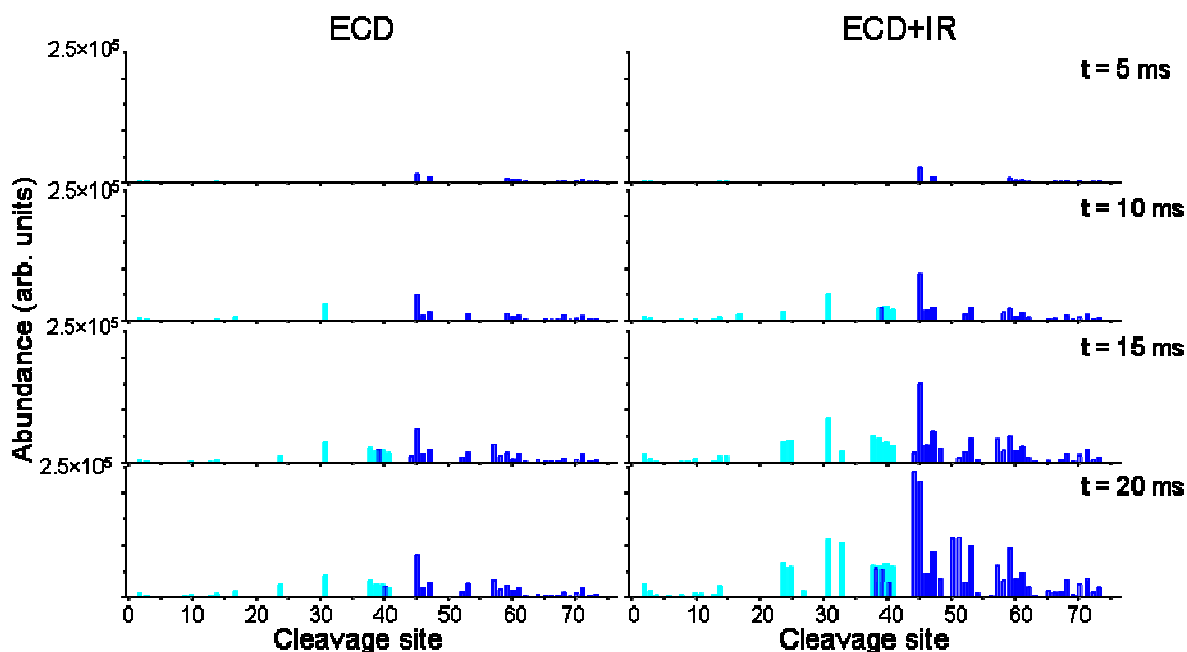
Figure 4.3.
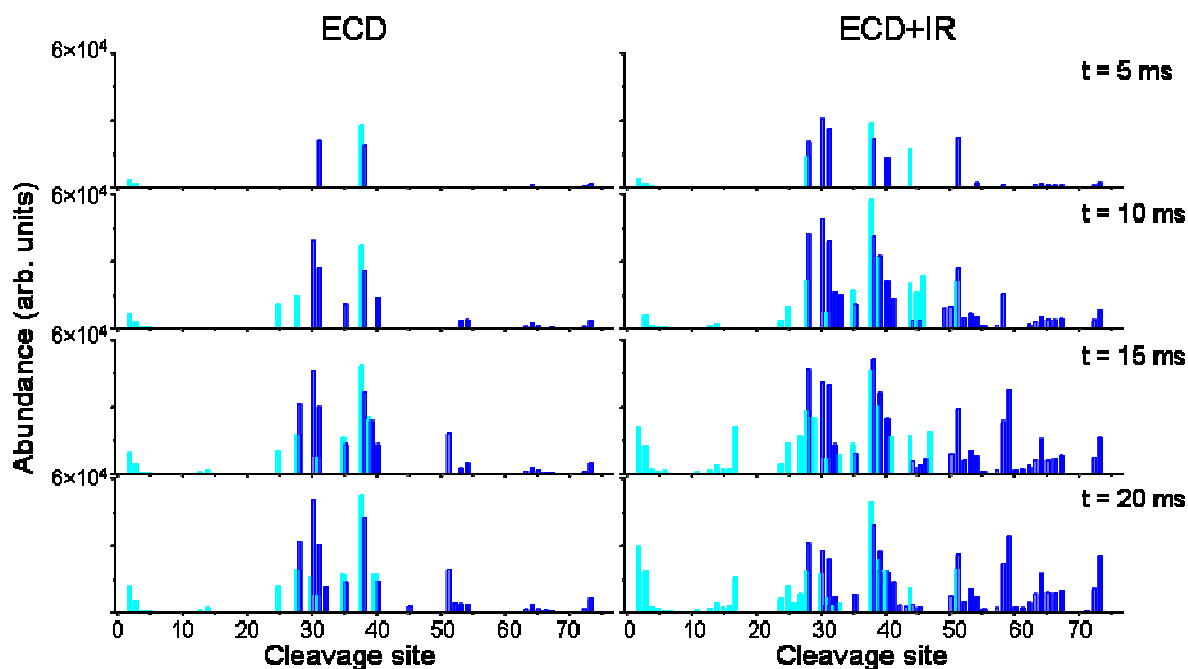
Figure 4.3 Comparison of dissociation pattern formed from ECD and ECD+IR of the +9 charge
state ion of ubiquitin for activation times ranging from 5 to 20 ms. The summed abundance of the
c′-type ions is represented by the filled cyan bars, and that of the z•-type ions is represented by the
hollow blue bars.

The data for ECD+IR of the +12 ubiquitin ion (Figure 4.2) and ECD+IR of the +9

ubiquitin ion (Figure 4.3) show that C-terminal unfolding occurred for multiple charge state

ions of ubiquitin. The similarity in structural unfolding for the +9 and +12 charge state ions

of ubiquitin indicates a common structural feature. Structural similarity for the +9 through

the +12 charge state ions has been shown by high field asymmetric ion mobility spectrometry

(FAIMS) which separates by shape-to-charge as opposed to mass-to-charge ratio used in

mass spectrometry. Using FAIMS, it has been concluded that the +9 through the +12 charge

state ions of ubiquitin have either a single conformation or a family of structures so similar

that it remains unresolved [16].

IR activation both sequentially to and simultaneously with ECD, has been shown to

increase the abundance and formation of c′-type and z$\cdot$-type product ions. IR activation of

the parent ions induces unfolding in the C-terminus as evidenced by the formation of new,

abundant z$\cdot$-ions and by the increase in the abundance of the these ions with increased IR

activation. Structural unfolding was observed for the N-terminus but to less of an extent than

the C-terminus. The termini became unfolded because of the disruption of noncovalent

interactions as a result of the absorption of IR photons.

4.3.2 Protonation site determination using ECD+IR

ECD+IR was performed on multiple charge state ions of ubiquitin resulting in

increased sequence coverage compared to ECD, as seen in Chapter 3. IR irradiation

simultaneously with ECD disrupted noncovalent interactions in both the parent and product

ions resulting in the greatest increases in c′-/z$\cdot$-ion formation and abundances. It has been

shown that ECD can be used to determine that charge sites in a protein from the product ion

distribution [5, 16]. Backbone cleavage in ECD has been shown to occur close to the

electron capture site [17], which is often at a charge site [18], so the distribution and charges

of the product ions from ECD can reveal charge sites. The addition of IR activation

enhances the application of ECD for charge site determination because the disruption of

noncovalent interactions increases the number of product ions detected. MS/MS spectra

produced by ECD+IR of the +9, +10, +11, and +12 charge state ions of ubiquitin were used

to determine the charge sites.

Ubiquitin has thirteen possible protonation sites with twelve basic residues and the N-terminus. The sequence of ubiquitin is shown in Figure 4.4 with the basic sites

MQIFV**K**TLTG **K**TITLEVEPS DTIENV**K**A**K**I
QD**K**EGIPPDQ Q**R**LIFAG**K**QL EDG**R**TLSDYN
IQ**K**ESTL**H**LV L**R**L**R**GG

Figure 4.4 Amino acid sequence of ubiquitin with the basic residues highlighted in orange.

highlighted in orange. The product ion distribution formed by ECD+IR of the +12 charge state ion of ubiquitin as a function of cleavage site is shown in Figure 4.5.
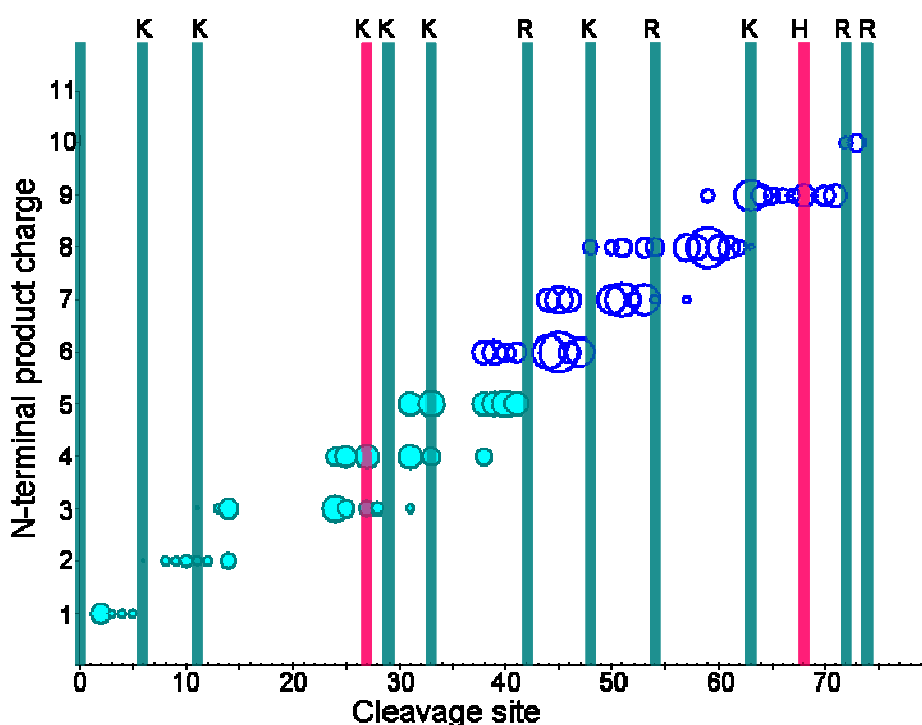
Figure 4.5 Product ion distribution resulting from ECD+IR (20 ms) of the +12 charge state ion of ubiquitin. The product ions are classified by the charge remaining on the N-terminus after backbone dissociation. Those N-terminal products assigned by the charge on the c′-ion are represented by filled cyan circles. The N-terminal products assigned by the charge on the complementary z•-ion are represented by the hollow blue circles. The relative sizes of the circles represent the abundance of the product ions formed. The bars represent the possible charge sites. The teal bars represent charged sites, and the pink bars represent the basic residues that are not charged.

For the product ion distribution plots, the product ions are organized by the charge remaining on the N-terminal product. For c'-ions, the charge on the N-terminal product was the charge of the c'-ion (filled cyan circles). To calculate the charge remaining on the N-terminus from $z^{\bullet}$-ion charge (hollow blue circles), Equation 4.1 was used.

$$\text{N-terminal ion charge} = \text{parent ion charge} - 1 - z^{\bullet}\text{-ion charge} \qquad \textbf{Equation 4.1}$$

The parent ion charge is reduced by one through electron capture, and this reduced charge is the amount of charge that was partitioned between the two product ions. The charge on the N-terminal product is the charge not located on the $z^{\bullet}$-, or C-terminal, ion. Hence the charge on the N-terminal product is the parent ion charge less one for electron capture and less the $z^{\bullet}$-ion charge. For example, the charge remaining on the N-terminal product formed by dissociation of the +12 parent ion resulting in the production of a $z^{3+\bullet}$ ion would be 12 - 1 - 3 = 8. The sizes of the circles represent the abundance of the product ions. The possible charge sites, i.e., arginine (R), histidine (H), lysine (K), and the N-terminus, are highlighted by the vertical bars.

The product ion distribution from ECD+IR was used to determine the charge sites of the protein ion. The number of charges on the N-terminal product was compared to the number of possible charge sites. If the number of charges equaled the number of charge sites, then each site was protonated. The presence of a non-protonated residue was determined when the number of charges was less than the number of charge sites. For example, the series of c'-ions ranging from c_2^+ to c_5^+ contains a single charge and a single possible charge site: the N-terminus. Therefore, the N-terminus must be protonated (teal bar). The comparison of the number of charges and the possible charge sites was continued to determine that K6 and K11 were also protonated. When product ions that included K27 and

K29 were examined, it was discovered that the addition of these two possible charge sites was associated with an increase of only one charge. The ions that include K27 and K29 had fewer charges than possible charge sites indicating that one of the two lysines was not protonated. Closer examination revealed that the addition of K27 had no associated increase in N-terminal product charge, and the addition of K29 did result in the increase of N-terminal product charge. The addition of the K27 basic site without a subsequent addition in N-terminal product charge led to the conclusion that K27 was not protonated in the +12 charge state of ubiquitin (pink bar).

Analysis of the rest of the potential charge sites showed that each addition of a charge site resulted in an increase in the charge state of the N-terminal product until H68 was included. The addition of H68 to the N-terminal product did not result in an increase in the charge state of that product. As with K27, the conclusion was that H68 was not protonated in the +12 charge state of ubiquitin. However, the +12 charge state of ubiquitin can only have one site that is not protonated because it has twelve charges to distribute among thirteen possible charge sites.

The solution to the inconsistency of two non-protonated sites in the +12 charge state of ubiquitin is found in the analysis by another method. HDXMS has shown that the +12 charge state of ubiquitin has two populations that exchange hydrogen for deuterium at different rates [8]. The presence of two populations defined by HDXMS led to the conclusion that there are two structures for the +12 charge state of ubiquitin. The duplicity of structures for the +12 charge state of ubiquitin explains the potential for two sites that were not protonated as evidenced by the ECD+IR product ion dissociation pattern.

The distribution of charges in the +12 charge state of ubiquitin results in either K27 or H68 uncharged. It is expected that the histidine would not be charged because histidine has been shown to have a lower proton affinity than arginine or lysine [19]. However, protonation of both K27 and K29 would result in strong Coulombic repulsion between these proximate sites resulting in a lower proton affinity for both lysines [20]. Thus, to reduce Coulombic repulsion, the K27 was also found to be uncharged. The observation of two possible uncharged basic sites implies that the gas-phase proton affinities of the two possible charge sites are similar.

The analysis of the N-terminal product charge was performed on the MS/MS spectra resulting from ECD+IR for the +11 (Figure 4.6), +10 (Figure 4.7), and +9 (Figure 4.8) charge state ions of ubiquitin. Teal bars represent the sites that are charged, pink bars indicate the sites that are not charged, and the orange bars represent the site that became uncharged upon reduction of charge state.
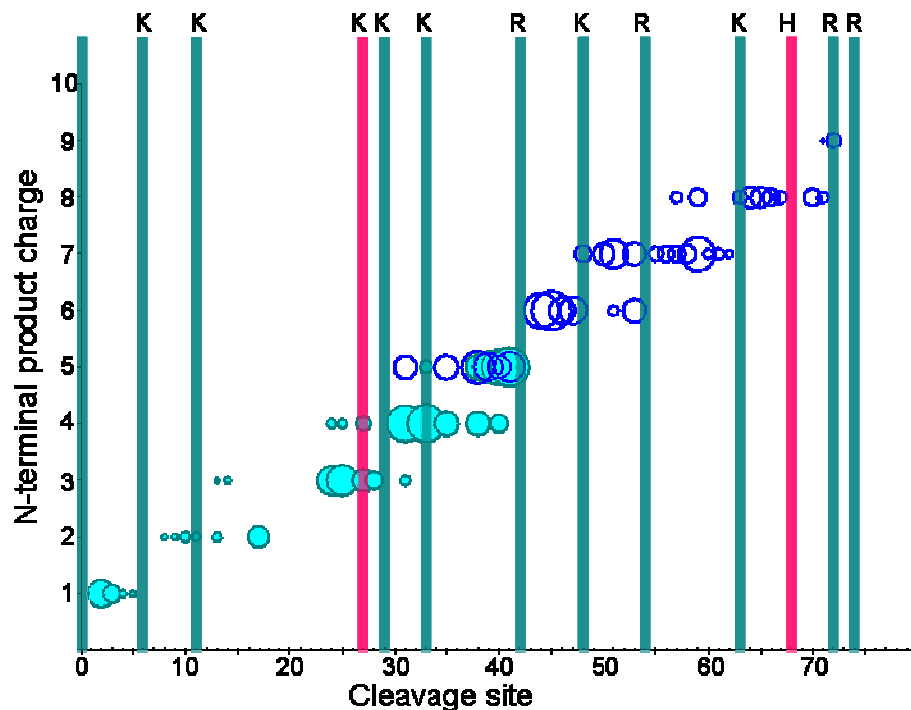
Figure 4.6 Product ion distribution resulting from ECD+IR (20 ms) of the +11 charge state ion of ubiquitin. Explanation of plot is provided in caption of Figure 4.4. There are no orange bars because both sites were predicted to be uncharged by the +12 ubiquitin ion.
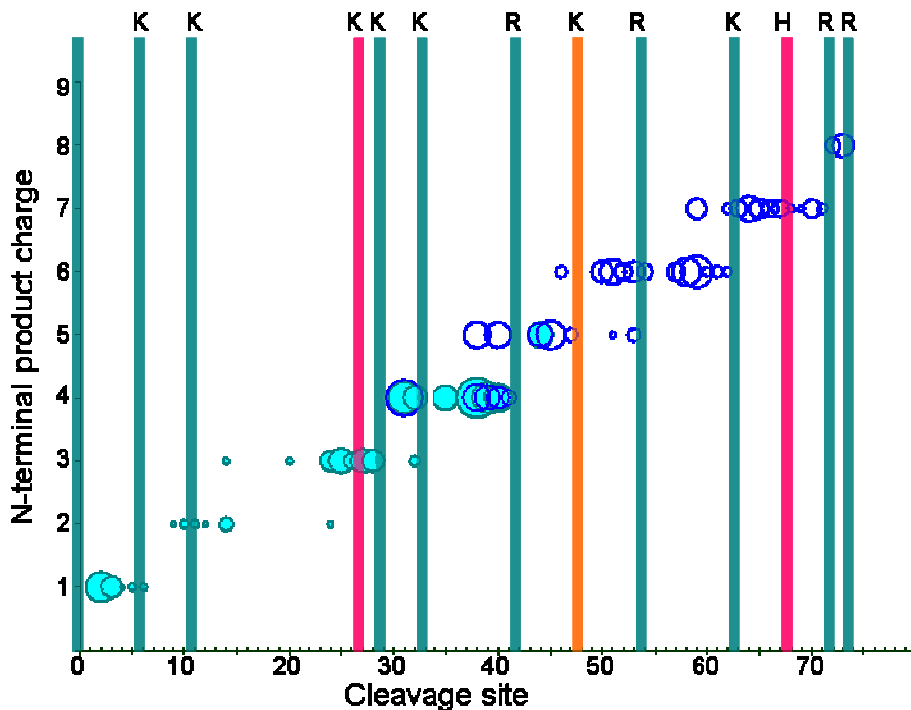
Figure 4.7 Product ion distribution resulting from ECD+IR (20 ms) of the +10 charge state ion of ubiquitin. Explanation of plot is provided in caption of Figure 4.4. New deprotonated sites are shown by the orange bar.
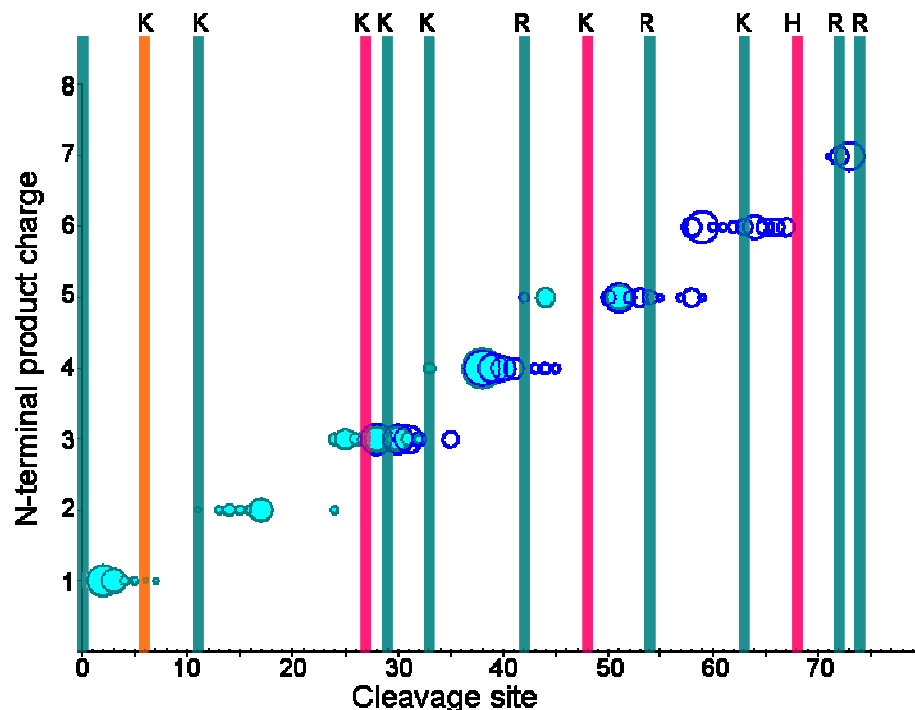
Figure 4.8 Product ion distribution resulting from ECD+IR (20 ms) of the +9 charge state ion of ubiquitin. Explanation of plot is provided in caption of Figure 4.4. New deprotonated site is shown by the orange bar.

In the analysis of lower charge states, it was assumed that the sites that were not protonated in the higher charge state were also not protonated in the lower charge state since charge location is dependent on proton affinity [20]. This assumption proved consistent with the data for the +9 through +12 charge state ions of ubiquitin. Analysis of dissociation pattern from the +11 charge state ion of ubiquitin revealed that both K27 and H68 were not charged. The +10 charge state ion was not charged at K27, K48, and H68. Loss of protonation at K6 was observed for the +9 charge state ion. The assignment of the protonation sites agrees with the proton affinities of the amino acid residues because arginine has the highest proton affinity followed by lysine then histidine [19]. Proton affinity is also dependent on the proximity of other charge sites [20]. Of the seven lysines in ubiquitin, the three lysines that became uncharged with decreasing charge state most likely had reduced proton affinities as a result of the nearby charge sites.

The decrease in the parent ion charge state helped and hindered the assignment of charge sites based on the N-terminal product charge. As the charge state of the parent ion decreased, analysis became more difficult due to the decrease product ion formation. The reduction in product ion formation is due to the decrease in potential electron capture sites and the increase in noncovalent interactions which can hold product ions together after backbone cleavage. The addition of IR activation decreased the influence of noncovalent interactions but did not eliminate it. The decrease in product ion formation was countered by the increase in information due to the overlap N-terminal product charge determined by c'- and $z^{\bullet}$-ions.

4.3.3 Electron capture locations

The analysis of the number of charges on the N-terminal products led to the assignment of charge sites for multiple charge state ions of ubiquitin. Analysis of the product ion distribution from ECD+IR can also be used to propose electron capture sites of the parent ion. To use the same example as before, the singly charged c'-ions, c_2^+ through c_5^+, were used to determine that the charge was located on the N-terminus. To form these small singly charged c'-ions, electron capture had to occur at a separate charged site. Product ions from ECD have been shown to cluster around the charge sites where electron capture occurs [17], so the electron capture site was most likely near where backbone cleavage occurred. Therefore, it is concluded that the protonated K6 was the electron capture site for the backbone cleavage that resulted in the formation of the c_2^+ through c_5^+ ions. While electron capture site cannot be determined for each product ion formed due to the possibility of radical migration during or after electronic relaxation through the Rydberg orbitals [21-23], the clustering of product ions around each of the charge sites indicates that electron capture

most likely occurred every protonation site instead of at a few. Also, contrary to what has

been published [5], the cluster of product ions around each charge state shows that backbone

cleavage occurs in both the N- and C-terminal directions from the electron capture site.

Preferential electron capture has been proposed to occur in multiply charged protein

ions. It is hypothesized that electron capture occurs at the less basic sites, i.e., sites with

lower proton affinities [24]. Preferential electron capture at charge sites would result in

higher product ion formation and abundance clustered around that charge site. While

preferential electron capture cannot be predicted currently, analysis of the product ion

abundances would provide insight to the proton affinity of the individual charge sites.

4.4 Summary and conclusions

ECD is a crucial dissociation technique in the analysis of protein structure because of

the retention of noncovalent interactions upon backbone cleavage. The addition of IR

activation followed by ECD showed that the increase in product ion formation was due to the

unraveling of the higher-order structure at the C-terminus of ubiquitin. C-terminal unfolding

was confirmed using ECD+IR, and it was shown that C-terminal unfolding is common for

multiple charge state ions of ubiquitin. The addition of IR activation increased the structural

disorder of the N-terminus but not to the same extent as the C-terminus. Finally, ECD+IR

was used to probe the sites of protonation in multiple charge state ions of ubiquitin. The

product ions were used to determine the charge remaining on the N-terminal product. The

comparison of the number of charges on the N-terminal product with the number of possible

charge sites was used to predict which basic sites were protonated. The clusters of product

ions around these charge sites indicated that each site was capable of electron capture and

that the radical could initiate backbone dissociation on either side of the charge site.

4.5 References

1.   Howard, G.C. and W.E. Brown, eds. *Modern Protein Chemistry: Practical Aspects.* 2002, CRC Press: Boca Raton. 257.

2.   Siuzdak, G., *The Expanding Role of Mass Spectrometry in Biotechnology.* 2003, San Diego: MRC Press.

3.   Badman, E.R., C.S. Hoaglund-Hyzer, and D.E. Clemmer Dissociation of Different Conformations of Ubiquitin Ions. *J. Am. Soc. Mass Spectrom.* **2002,** *13,* 719 - 723.

4.   Hoffmann, E.d. and V. Stroobant, *Mass Spectrometry: Principles and Applications, 2 ed.* 2002, New York: John Wiley & Sons. 407.

5.   Breuker, K., H. Oh, D.M. Horn, B.A. Cerda, and F.W. McLafferty Detailed Unfolding and Folding of Gaseous Ubiquitin Ions Characterized by Electron Capture Dissociation. *J. Am. Chem. Soc.* **2002,** *124,* 6407-6420.

6.   Breuker, K. and M. Tollinger. *Gas-Phase Structures of the Three Helix Bundle Protein KIX Probed by Electron Capture Dissociation.* in *The 58th ASMS Conference on Mass Spectrometry and Allied Topics.* 2010. Salt Lake City, UT.

7.   Horn, D.M., K. Breuker, A.J. Frank, and F.W. McLafferty Kinetic Intermediates in the Folding of Gaseous Protein Ions Characterized by Electron Capture Dissociation Mass Spectrometry. *J. Am. Chem. Soc.* **2001,** *123,* 9792-9799.

8.   Freitas, M.A., C.L. Hendrickson, M.R. Emmett, and A.G. Marshall Gas-phase bovine ubiquitin cation conformations resolved by gas-phase hydrogen/deuterium exchange rate and extent. *Int. J. Mass Spectrom.* **1999,** *185/186/187,* 565-575.

9.   Breuker, K. and F.W. McLafferty Stepwise evolution of protein native structure with electrospray into the gas phase, 10(-12) to 10(2) S. *PNAS.* **2008,** *105,* 18145-18152.

10.   Ly, T. and R.R. Julian Elucidating the Tertiary Structure of Protein Ions in Vacuo with Site Specific Photoinitiated Radical Reactions. *J. Am. Chem. Soc.* **2010,** *132,* 8602-8609.

11.   Koeniger, S.L. and D.E. Clemmer Resolution and Structural Transitions of Elongated States of Ubiquitin. *J. Am. Soc. Mass Spectrom.* **2007,** *18,* 322-331.

12.   Myung, S., E. Badman, Y. Lee, and D. Clemmer Structural transitions of electrosprayed ubiquitin ions stored in an ion trap over similar to 10 ms to 30 s. *J. Phys. Chem. A.* **2002,** *106,* 9976-9982.

13.   Badman, E.R.H.-H., C. S.; Clemmer, D. E. Monitoring Structural Changes of Proteins in an Ion Trap over 10 - 200 ms: Unfolding Transitions in Cytochrome *c* Ions. *Anal. Chem.* **2001,** *73,* 6000-6007.

14.   Shelimov, K.B., D.E. Clemmer, R.R. Hudgins, and M.F. Jarrold Protein Structure *in Vacuo*: Gas-Phase Conformations of BPTI and Cytochrome c. *J. Am. Chem. Soc.* **1997,** *119,* 2240-2248.

15.   Horn, D.M., Y. Ge, and F.W. McLafferty Activated Ion Electron Capture Dissociation for Mass Spectral Sequencing of Larger (42 kDa) Proteins. *Anal. Chem.* **2000,** *72,* 4778-4784.

16.   Robinson, E.W., R.D. Leib, and E.R. Williams The Role of Conformation on Electron Capture Dissociation of Ubiquitin. *J. Am. Soc. Mass Spectrom.* **2006,** *17,* 1470 - 1480.

17.   Cerda, B.A., K. Breuker, D.M. Horn, and F.W. McLafferty Charge/Radical Site Initiation versus Coulombic Repulsion for Cleavage of Multiply Charged Ions. Charge Solvation in Poly(alkene glycol) Ions. *J. Am. Soc. Mass Spectrom.* **2001,** *12,* 565-570.

18.   Neff, D. and J. Simons Analytical and Computational Studies of Intramolecular Electron Transfer Pertinent to Electron Transfer and Electron Capture Dissociation Mass Spectrometry. *J. Phys. Chem. A. 114,* 1309-1323.

19.   Gorman, G.S., J.P. Speir, C.A. Turner, and I.J. Amster Proton Affinities of the 20 common Amino Acids. *J. Am. Chem. Soc.* **1992,** *114,* 3986-3988.

20.   Schnier, P.D., D.S. Gross, and E.R. Williams On the Maximum Charge-State and Proton-Transfer Reactivity of Peptide and Protein Ions Formed by Electrospray-Ionization. *J. Am. Soc. Mass Spectrom.* **1995,** *6,* 1086-1097.

21.   Neff, D. and J. Simons Analytical and Computational Studies of Intramolecular Electron Transfer Pertinent to Electron Transfer and Electron Capture Dissociation Mass Spectrometry. *J. Phys. Chem. A.* **2010,** *114,* 1309-1323.

22.   Neff, D., M. Sobczyk, and J. Simons Through-space and through-bond electron transfer within positively charged peptides in the gas phase. *Int. J. Mass Spectrom.* **2008,** *276,* 91-101.

23.   Simons, J. Mechanisms for S-S and N-C-alpha bond cleavage in peptide ECD and ETD mass spectrometry. *Chem. Phys. Lett.* **2010,** *484,* 81-95.

24.   Kjeldsen, F., M.M. Savitski, C.M. Adams, and R.A. Zubarev Determination of the location of positive charges in gas-phase polypeptide polycations by tandem mass spectrometry. *Int. J. Mass Spectrom.* **2006,** *252,* 204-212.

Chapter 5

Ion-Molecule Reactions Probe Reactivity of z•-ions

5.1 Introduction

Electron capture dissociation (ECD) tandem mass spectrometry (MS/MS) is useful method for peptide sequencing due to efficient backbone cleavage which leads to near complete sequence coverage for peptides and smaller proteins [1-4]. These backbone cleavages form c′- and z•-type product ions from the dissociation of the N-C_α bond [1]. Differentiation of the c′- and z•-type product ions in the ECD MS/MS spectrum increases the likelihood of correct protein identification using database searching [5]. ECD product ions can be distinguished because the z•-type product ion have a fundamentally different chemistry from the c′-type ions.

Radical molecules are known to undergo different types of chemistry than even-electron molecules. One specific example is the spontaneous reaction of gaseous alkyl radicals with molecular oxygen in the upper atmosphere. In this reaction, oxygen acts as a radical scavenger and binds to the alkyl radical to form an alkylperoxy radical (Scheme 1) [6].

$$R^\bullet + O_2 \xrightarrow{M} RO_2{}^\bullet \qquad \textbf{Scheme 1}$$
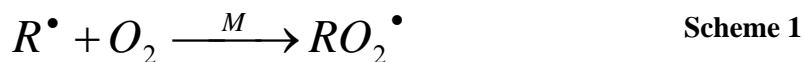
In the upper atmosphere, this reaction often requires a third reactant (M) that removes excess internal energy released during C-O bond formation. However, the necessity of the third reactant to remove excess internal energy decreases as the size of the alkyl radical increases because the bond formation energy can be distributed throughout the degrees of freedom of the alkyl radical. This reaction occurs at very high rates and is often considered spontaneous

because the formation of alkylperoxy radicals is the only fate observed for alkyl radicals in atmospheric chemistry [6].

The reaction between a radical ion formed from an electron capture event and molecular oxygen has been demonstrated using $z^{\bullet}$-type ions formed from a variety of techniques [7-9]. This reaction was first employed using oxygen as the bath gas in a linear ion trap (LIT) during electron transfer dissociation (ETD) [7]. The $z^{\bullet}$-ions readily reacted to form the oxygen-adduct as evidenced by a shift in the $z^{\bullet}$-ion mass by 32 daltons. Increases in the adduct internal energy via increased bath gas temperature or collisional activation resulted in loss of the oxygen-adduct. The formation of the oxygen-adduct led to facile classification of $z^{\bullet}$-ions which improved sequence identification [7]. Identification of $z^{\bullet}$-ions can also be used as a postsearch filter to improve protein identification from low quality ETD MS/MS spectra [5].

Molecular oxygen has also been used for the identification of radical product ions produced from ECD [8]. In these experiments, oxygen was leaked into the mass spectrometer in a region separate from the ECD reaction chamber. Because oxygen was not used as a bath gas, the use of the ion-molecule reaction for the identification of $z^{\bullet}$-ions was selective. Product ions that had reacted with oxygen were compared with those ions that had not to classify c'- and $z^{\bullet}$-type ions. The differentiation of c'-ions from $z^{\bullet}$-ions was utilized in a *de novo* sequencing algorithm. Backbone cleavage points were determined by the presence of a c'- or $z^{\bullet}$-ion. The *de novo* sequencing program used the overlap of a confirmed $z^{\bullet}$-ion with a c'-ion to increase the confidence of that cleavage point in the protein. Successful analysis relied on overlap of the c'- and $z^{\bullet}$-ion series and was therefore limited to peptides and small proteins which exhibit high sequence coverage. These two studies show how the

ion-molecule reaction between molecular oxygen and radical ions can be used for positive identification of z$^\bullet$-ions which aids in peptide sequencing.

The ion-molecule reaction between radical ions and oxygen has also been used to monitor through-space radical migration. In these experiments, the radical was generated by the homolytic cleavage of an iodo-carbon bond on an aromatic residue of a small polypeptide cation [9]. Reaction between this radical cation and molecular oxygen was used to determine the radical location. Through-space radical migration was used to explain the differences in fragmentation pattern based on the chemical environment of the radical. In this study, the ion-molecule reaction between molecular oxygen and radical ions was used to probe the location and chemical environment of the radical.

In the mechanism for backbone dissociation following electron capture, the radical is generated on the N-terminal alpha-carbon of the z$^\bullet$-ion [1]. To date, the radical on the z$^\bullet$-type product ion has been assumed to remain at this location [7, 10, 11]. The position of the radical on the N-terminal alpha-carbon has been assumed for each variation of ECD that has been presented, including activated-ion ECD (AI-ECD) and hot ECD (HECD). Due to the similarities in dissociation pattern, it has also been assumed that backbone dissociation occurs by the same mechanism for each electron capture technique and that the product ions have the same structures [2, 12]. However, it has been noted that the various electron capture techniques differ with respect to the excess ion internal energy after electron capture. The excess internal energy in the ion after electron capture is thought to arise from Coulombic potential energy between the charge sites prior to backbone cleavage [13] and the recombination energy released upon electron capture [2, 3, 14]. Therefore, the variations in excess ion internal energy for the assorted electron capture techniques are due to the

96

differences in the electron capture process by the multiply charged cation. For example, the radical cation formed during ETD is thought to have lower internal energy than the ion formed during ECD. In ETD, the electron is transferred to the polycation by a gaseous electron-donor anion as opposed to the capture of a free electron in ECD. Because the electron must be removed from the anion, the recombination energy released during electron transfer is reduced by the electron affinity of the anion [10, 14, 15]. AI-ECD and HECD form additional product ions due to the increased internal energy of the parent ions [3, 12]. The increased internal energy comes from the activation of the ions using vibrational excitation (AI-ECD) [16] or from the conversion of electron kinetic energy to ion internal energy prior to capture of the decelerated electron, as proposed in the mechanism for HECD [12]. The additional product ions resultant from the increased ion internal energy include increased prevalence of a$^{\bullet}$- and y-type ions from the minor radical dissociation channel as well as side-chain losses [2, 3]. The formation of a$^{\bullet}$- and y-ions requires the dissociation of two bonds and therefore is typically observed in parent ions with increased internal energy [2].

The excess internal energy of the ions after electron capture could lead to radical migration away from the site of formation on the N-terminal alpha-carbon. It has been shown that the radical can migrate through-space and along the backbone to other positions and induce dissociation away from the initial electron capture site [10, 13, 17]. This radical migration has been observed in the charge-reduced species and z$^{\bullet}$-type product ions formed using ECD without additional ion activation [9, 10, 17, 18]. Calculations have shown that the various alpha-carbon positions along the backbone do not differ greatly with respect to radical stability [13]. When internal energy through collisional activation is added to the

radical cation formed from ECD to induce further dissociation, it has been shown that the dissociation pattern follows a radical-driven dissociation pathway. New c′-/z•-type product ions along with side-chain losses confirm the possibility of radical migration [5, 19-21]. The work presented here uses the ion-molecule reaction between z•-type product ions and oxygen to probe the reactivity of the z•-ions with implications of the effects of ion internal energy on radical migration.

5.2 Experimental

5.2.1 Samples

To monitor the ion internal energy effects of various electron capture methods, the peptide neurotensin (pELYENKPRRPYIL) was analyzed. Neurotensin was purchased from Sigma-Aldrich (St. Louis, MO) and used without further purification. Solutions were prepared at a concentration of 5 μM in 50/50 v/v acetonitrile/water with 1% formic acid to aid in the electrospray process. The $z_{10}^{2+\bullet}$, $z_{11}^{2+\bullet}$, and the $z_{12}^{2+\bullet}$ product ions were formed using ECD, AI-ECD, and HECD of the +3 charge state ion of neurotensin. The z•-ions were then trapped in the LIT_{therm} for reaction with molecular oxygen to monitor the reactivity of the z•-ions. The $z_{12}^{2+\bullet}$ ion was collisionally activated in the ECD_{LIT} prior to reaction with oxygen to monitor the effects of product ion internal energy on reactivity with oxygen. Details of the different electron capture techniques and the instrument modifications necessary to implement the ion-molecule reaction can be found in Chapters 1 and 2.

5.2.2 Data analysis

Product ions were identified using the search program described in Chapter 2. A separate program was written using LabView code (National Instruments) to detect the formation of the oxygen adduct by searching for peaks at 32 Da/charge heavier. The

presence of the oxygen adduct was confirmed manually. The program output the abundance of the product ion and the oxygen adduct. The reactivity of the $z^\bullet$-ions was monitored in terms of reactivity with oxygen, called the O_2 reactivity. The O_2 reactivity represents the fraction of the $z^\bullet$-ion population that is reactive to oxygen. The O_2 reactivity is equal to the abundance of the reactive $z^\bullet$-ion divided by the summed abundance of the non-reactive and the reactive $z^\bullet$-ions (Equation 5.1).

$$O_2 \text{ reactivity} = \frac{[z^\bullet + O_2]^{n+}}{[z^\bullet]^{n+} + [z^\bullet + O_2]^{n+}} \qquad \textbf{Equation 5.1}$$

5.3 Results and discussion

5.3.1 Confirmation of $z^\bullet$-ion reactivity with oxygen

Oxygen was leaked into the LIT_{therm} during ECD MS/MS experiments to confirm the reactivity of $z^\bullet$-ions and the non-reactivity of c'-ions. The O_2 reactivities for selected $z^\bullet$- and c'-ions of neurotensin formed during ECD are shown in Figure 5.1. These reactivities are plotted as a function of the oxygen flow rate into the LIT_{therm}.
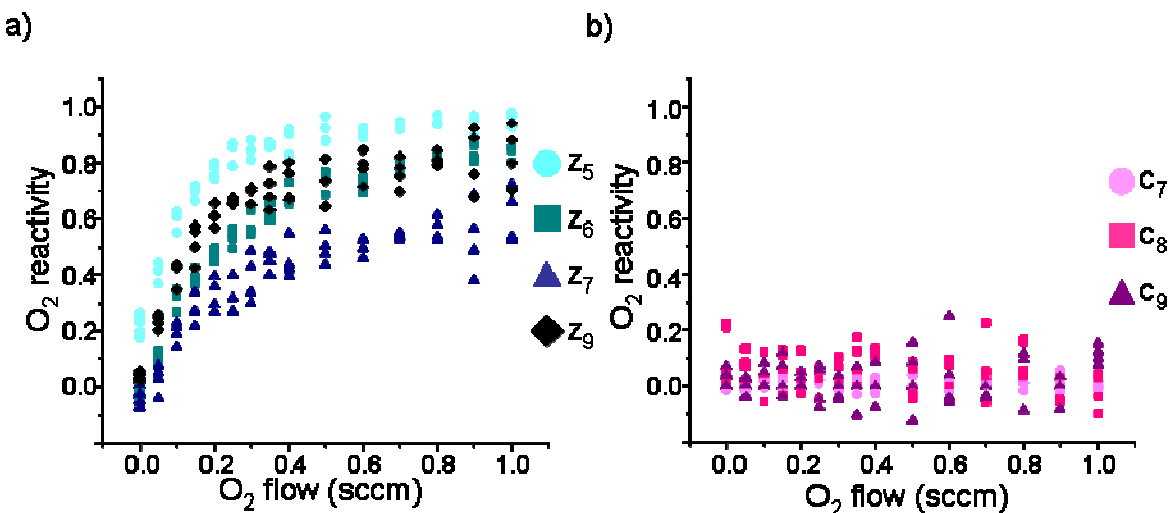

Figure 5.1 a) O_2 reactivity of $z^\bullet$-type product ions formed by ECD of neurotensin. b) O_2 reactivity of c'- type product ions formed by ECD of neurotensin. O_2 reactivity is plotted as a function of O_2 gas flow rate leaked into the LIT_{therm}. The trial was repeated four times.

The O$_2$ reactivity of each of the z$^{\bullet}$-type ions increased until stasis was reached, but the c$'$-type ions did not react with oxygen at all. The increase in O$_2$ reactivity with the increase in partial pressure of oxygen was expected from what is observed in atmospheric chemistry where the rate of reaction is dependent on oxygen concentration [6]. Leaking oxygen into the LIT$_{therm}$ was impractical because of the decreased lifetime of the electron filament due to oxidation [22]. Therefore, the second reaction instrumental configuration, described in Chapter 2, was adopted. Briefly, this second configuration used ambient oxygen from the nano-electrospray (nESI) source in the instrument, and the ion-molecule reaction was performed in the LIT$_{therm}$.

5.3.2 Electron kinetic energy and O$_2$ reactivity

When oxygen was added to z$^{\bullet}$-type ions formed during ETD, the reaction went to completion, and the entire population converted to the oxygen adduct form [7]. However, the z$^{\bullet}$-ions formed from ECD and HECD in the ECD$_{LIT}$ did not behave in the same manner (Figure 5.2).
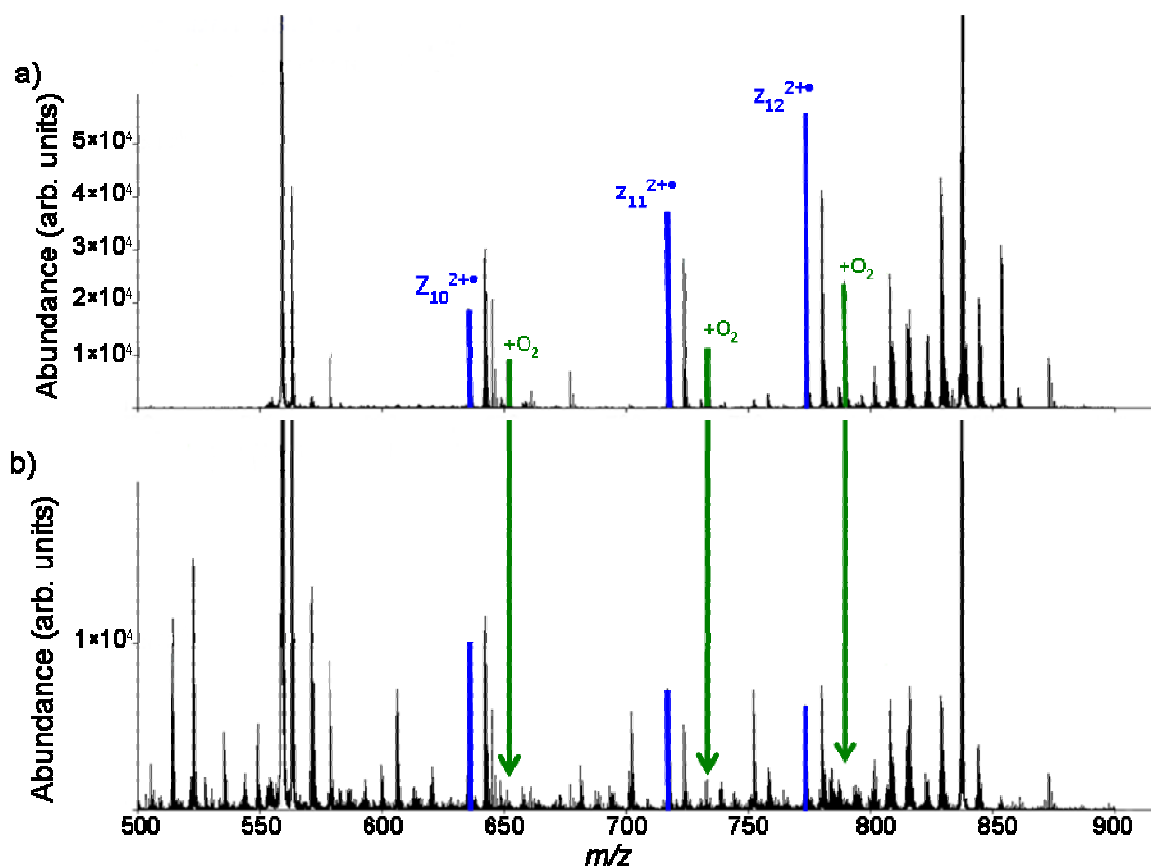
Figure 5.2 a) ECD MS/MS spectrum of the +3 charge state ion of neurotensin followed by reaction with oxygen. b) HECD (7 eV electrons) MS/MS spectrum of the +3 charge state ion of neurotensin followed by reaction with oxygen. The $z_{10}^{2+•}$, $z_{11}^{2+•}$, and $z_{12}^{2+•}$ product ions are highlighted in blue, and the oxygen adducts for these ions are highlighted in green.

In this figure, it is evident that the z$^•$-type ions formed during ECD (top spectrum) reacted with oxygen to form the oxygen adduct, but the z$^•$-ions formed during HECD do not, as seen in the bottom spectrum. The difference between these techniques is the electron kinetic energy, so the O_2 reactivity of selected z$^•$-ions was monitored as a function of electron kinetic energy (Figure 5.3).
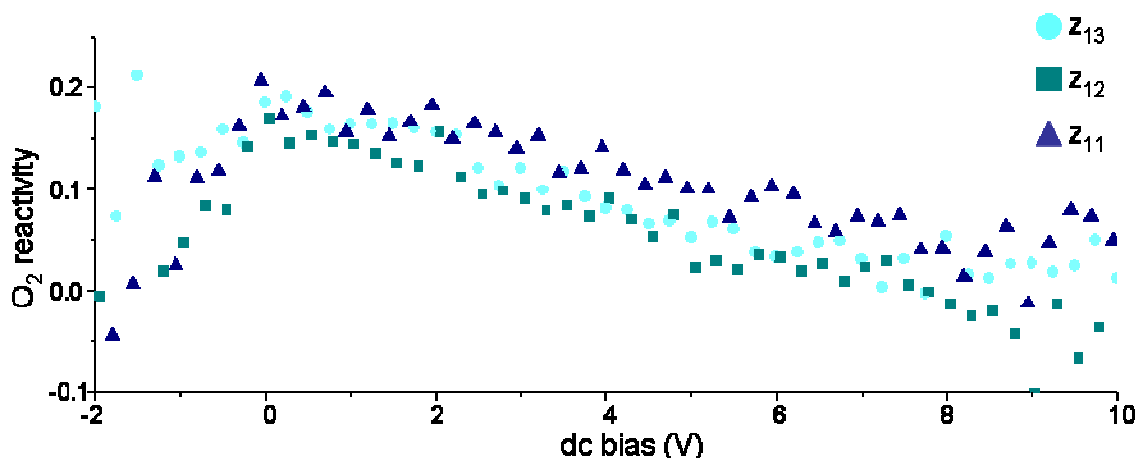
Figure 5.3 O_2 reactivity of the $z_{13}^{2+\bullet}$, $z_{12}^{2+\bullet}$, and $z_{11}^{2+\bullet}$ ions from neurotensin as a function of dc bias between the electron filament and the rods of the ECD_{LIT}. The electron kinetic energy is the dc bias +1.75 to compensate for the difference in work function involved in thermionic electron emission as described in Chapter 2.

The decrease in O_2 reactivity with increasing electron kinetic energy represents a decrease in the fraction of the population of the $z^\bullet$-ion that reacts to form the oxygen adduct. In this plot, some of the O_2 reactivity values are negative because the abundances of the $z^\bullet$-ions and the oxygen adducts were noise-subtracted before determination of the reactivity. For each $z^\bullet$-ion studied, the O_2 reactivity decreased as the electron kinetic energy was increased until no oxygen adduct formation was observed. The decrease in O_2 reactivity for $z^\bullet$-type ions as electron kinetic energy was increased implies there is a structural difference between $z^\bullet$-type ions formed from different electron capture techniques.

5.3.3 Ion internal energy manipulation

The O_2 reactivity for a given $z^\bullet$-ion changed depending on the electron capture technique used. The techniques used so far, ETD [7], ECD, and HECD, differ in ion internal energy after electron capture and are ranked as ETD < ECD < HECD. The internal energy of the radical ions formed during ETD is decreased because the recombination energy is reduced by the electron affinity of the anion donor [3, 12]. The radical ions formed during

HECD have increased ion internal energy due to the conversion of electron kinetic energy to ion internal energy prior to capture of the decelerated electron [12]. To further study the behavior of radical ions, manipulation of the ion internal energy was required. In the ECD_{LIT}, two ways were used to manipulate the ion internal energy: variation of the helium bath gas pressure and incorporation of IR activation of the ions.

The helium bath gas pressure affects ion internal energy through collisions that transfer internal energy between the ions and the helium atoms. Changes in pressure result in changes in collisional cooling rate due to differences in number density of the bath gas at different pressures [22, 23]. Higher collisional cooling rates ensure more rapid transfer of excess ion internal energy to the bath gas. Radical ions generated by electron capture techniques have an increased internal energy as a result of the recombination energy released in the formation of the radical. In the ECD_{LIT}, the pressure is such that excess internal energy is rapidly lost to the bath gas through collisions. By decreasing the helium bath gas pressure, the collisional cooling rate is decreased, and the ions maintain increased internal energy state for a longer lifetime. The O_2 reactivity of the $z_{12}^{2+\bullet}$ ion formed during ECD of neurotensin at a range of bath gas pressures varying from 0.004 mbar to 0.065 mbar is shown in Figure 5.4.
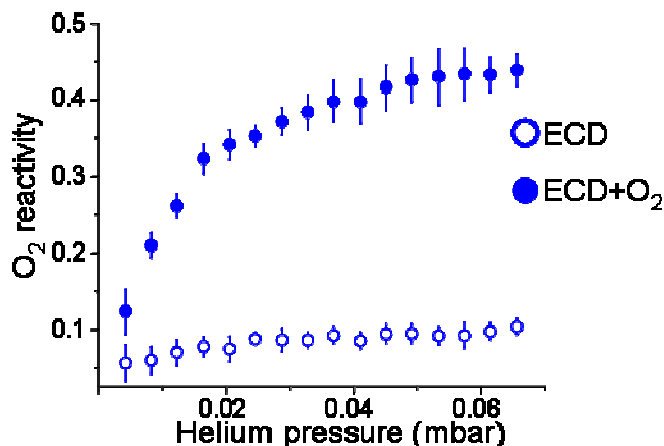
Figure 5.4 O_2 reactivity of the $z_{12}^{2+\bullet}$ ion of neurotensin formed during ECD (25 ms) as a function of helium bath gas pressure in the ECD_{LIT}. The hollow symbols represent those ions that were not trapped for reaction with oxygen; the filled symbols represent those ions that were trapped for reaction with oxygen. The error bars represent the uncertainty of the experimental isotopic abundances compared with theoretical isotopic abundances.

As discussed in Chapter 2, the pressure in the ECD_{LIT} was calculated using the measured temperature and the thin aperture conductance formula [24]. The pressure was observed to change with time as the filament heated the bath gas, and a steady-state bath gas temperature of 65°C was assumed to be the temperature during these experiments. The steady-state temperature was used to calculate the conductance through the ECD_{LIT} and therefore the pressure in the trapping region. The O_2 reactivity of the $z^\bullet$-ion that was not trapped for reaction with oxygen was monitored as a control to ensure that the helium bath gas pressure in the ECD_{LIT} did not affect ion behavior in the LIT_{therm}. The O_2 reactivity of the $z_{12}^{2+\bullet}$ ion increased with increasing helium bath gas pressure. At high bath gas pressures, the radical was reactive to oxygen, but the reactivity of the $z^\bullet$-ion was lost at low bath gas pressures. The loss of reactivity at lower bath gas pressures, and therefore lower collisional cooling rates, shows that when the ion has a longer lifetime with increased internal energy, the radical becomes non-reactive to oxygen. The dependence of O_2 reactivity on helium bath gas pressure implies that the ion has some extra internal energy after ECD, presumably from the recombination energy, which affects the reactivity of the $z^\bullet$-ions with oxygen.

To confirm that $z^\bullet$-type product ions formed during HECD are not reactive with oxygen, the O_2 reactivity of the $z_{12}^{2+\bullet}$ion with and without extended trapping in the LIT_{therm} for reaction with oxygen was monitored as a function of helium bath gas pressure in the ECD_{LIT} (Figure 5.5). The extended trapping time for reaction with oxygen did not result in a significant difference in O_2 reactivity for the $z_{12}^{2+\bullet}$ ion formed during HECD. Also, the $z^\bullet$-ion formed from HECD reacted with oxygen significantly less than the $z^\bullet$-ion formed from ECD at all bath gas pressures except the lowest pressures.

Figure 5.5 O_2 reactivity of the $z_{12}^{2+\bullet}$ ion of neurotensin formed during ECD (25 ms, blue circle) and HECD (15 ms, navy square) as a function of helium bath gas pressure. The hollow symbols represent ions that were not trapped for reaction with oxygen; the filled symbols represent ions that were trapped for reaction with oxygen.

The overlap in O_2 reactivity at the lowest bath gas pressures shows that the $z^\bullet$-type ions formed during ECD at low bath gas pressures are similar to the $z^\bullet$-type ions formed during HECD at any pressure.

The $z^\bullet$-ion formed during ECD at low helium bath gas pressures behaved like a $z^\bullet$-ion with high internal energy while the $z^\bullet$-ion formed during ECD at high bath gas pressures behaved like a $z^\bullet$-ion with low internal energy. The difference in behavior for the $z^\bullet$-ions formed during ECD is due to the difference in collisional cooling rates between high and low bath gas pressures. The $z^\bullet$-ions from ECD are formed with the same amount of released recombination energy, but the lifetime of this energetic ion is determined by the collisional

cooling rate. At low bath gas pressures, the lifetime of the excited ion is such that the reactivity of the radical ion changes. At high bath gas pressures, the excess internal energy of the ion is lost to the bath gas before the reactivity of the radical ion changes. The dependence of O_2 reactivity on helium bath gas pressure for $z^\bullet$-ions from ECD suggests that the lifetime of the excited ion determines the reactivity of the $z^\bullet$-ion with oxygen. The $z^\bullet$-ions formed during HECD exhibit no difference in O_2 reactivity with the changes in helium bath gas pressure. The independence of O_2 reactivity for the $z^\bullet$-ions formed during HECD from bath gas pressure implies that the mechanism of HECD is so energetic that the internal energy effects from the bath gas are relatively insignificant.

To establish whether ion internal energy determines the O_2 reactivity for this ion, the $z^\bullet$-ions were formed using simultaneous AI-ECD (ECD+IR) and then trapped for reaction with oxygen. The addition of IR activation, covered in Chapter 3, increases the ion internal energy through the absorption of IR photons. This internal energy is adequate for the disruption of noncovalent interactions but not sufficient to cleave the peptide backbone. In

Figure 5.6, the O_2 reactivity of the $z_{12}^{2+\bullet}$ formed from ECD, which has been shown to react extensively with oxygen at high bath gas pressures, HECD, which has been shown not to react with oxygen, and ECD+IR are shown. Like the $z^\bullet$-ions formed during ECD, the O_2
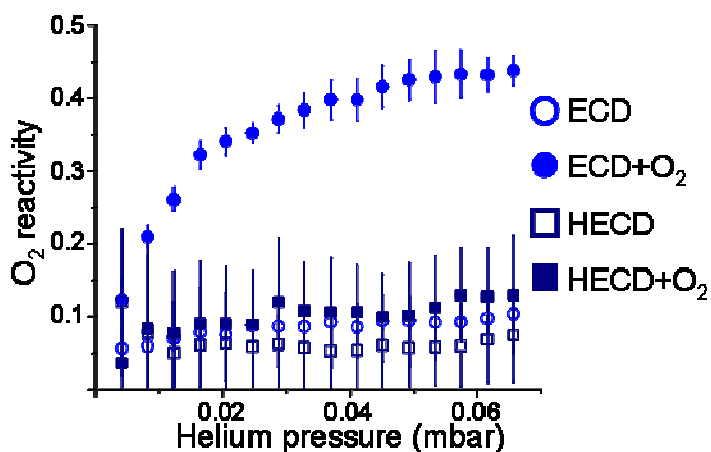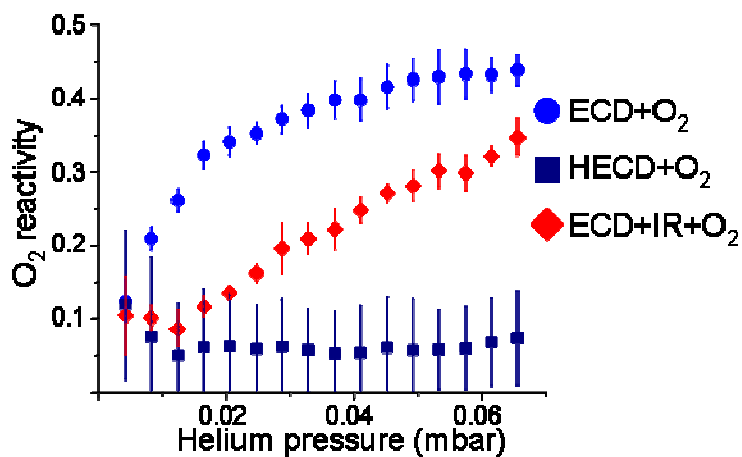
Figure 5.6 O_2 reactivity of the $z_{12}^{2+\bullet}$ ion of neurotensin formed during ECD (25 ms, blue circle), HECD (15 ms, navy square), and ECD+IR (25 ms, red diamond) and trapped for reaction with oxygen as a function of helium bath gas pressure in the ECD_{LIT}.

106

reactivity of the z$^\bullet$-ions formed during ECD+IR has a dependence on the helium bath gas pressure. As the bath gas pressure was increased, the O_2 reactivity increased due to the effect of collisional cooling with the helium bath gas on ion internal energy. However, the O_2 reactivity of the z$^\bullet$-ions formed during ECD+IR is decreased compared to the O_2 reactivity of the z$^\bullet$-ions formed during ECD at all bath gas pressures. The decrease in O_2 reactivity of the z$^\bullet$-ions formed during ECD+IR is due to the increase in ion internal energy from IR activation during product ion formation. From Figure 5.6, it can be concluded that ion internal energy increases from ECD to ECD+IR to HECD.

During ECD and HECD, excess internal energy of the parent ion is statistically distributed to the product ions [25, 26]. During ECD+IR, both the parent and product ions are activated by IR photons, so it is uncertain whether the O_2 reactivity is dependent on the parent ion or product ion internal energy. To determine the influence parent and product ion internal energy, sequential AI-ECD was used. IR activation prior to electron irradiation (IR/ECD) exclusively activates the parent ion. Exclusive activation of the product ions is achieved by IR activation after electron irradiation (ECD/IR). The O_2 reactivities for the $z_{12}^{2+\bullet}$ ion of neurotensin formed using the three AI-ECD techniques are shown in Figure 5.7.
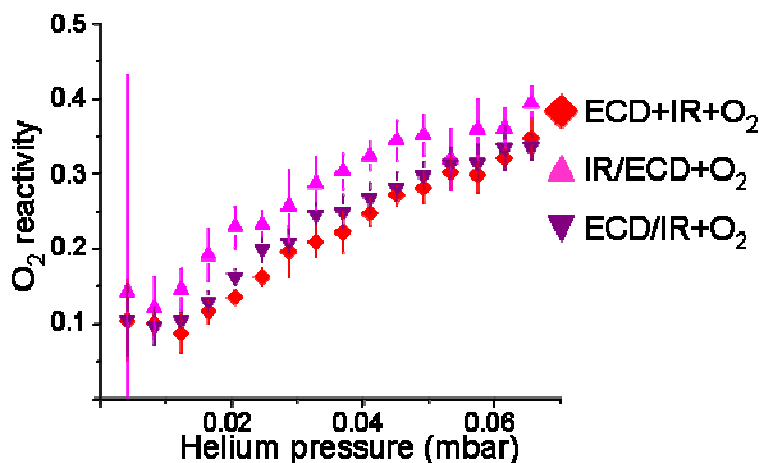
Figure 5.7 O_2 reactivity of the $z_{12}^{2+\bullet}$ ion of neurotensin formed during ECD+IR (25 ms, red diamonds), IR/ECD (20 ms IR irradiation, 5 ms electron irradiation, pink triangles), and ECD/IR (20 ms electron irradiation, 20 ms IR irradiation, purple triangles) and trapped for reaction with oxygen as a function of helium bath gas pressure in the ECD_{LIT}.

While the O_2 reactivity of the z$^\bullet$-ions was not statistically

different for ECD/IR and ECD+IR, the z$^\bullet$-ions formed during IR/ECD have a statistically higher O_2 reactivity at most bath gas pressures. The z$^\bullet$-ions formed using ECD/IR, i.e., increased product ion internal energy, had an O_2 reactivity most similar to the ions formed during ECD+IR. The z$^\bullet$-ions formed using IR/ECD, i.e., increased parent ion internal energy, had the highest O_2 reactivity of the three techniques. The O_2 reactivity for the z$^\bullet$-ions formed during IR/ECD is decreased from that of the ions formed during ECD. The activation of the parent ions increased ion internal energy prior to dissociation by ECD, and the excess internal energy was distributed to the product ions [25, 26]. However, the z$^\bullet$-ion internal energy is less from IR/ECD than ECD/IR due to loss of parent ion internal energy as a result of collisional cooling prior to backbone dissociation. Activation of the product ions caused a greater reduction in O_2 reactivity than activation of the parent ions. Because activation of the product ions decreased O_2 reactivity more than activation of the parent ion, it was concluded that product ion internal energy exerts more influence on the O_2 reactivity than the parent ion internal energy.

5.3.4 Reactive and non-reactive z$^\bullet$-type product ions

The use of various helium bath gas pressures and IR activation determined that ion internal energy affects the O_2 reactivity of z$^\bullet$-type product ions. Sequential AI-ECD showed that product ion internal energy has more influence on O_2 reactivity than parent ion internal energy. To confirm that product ion internal energy directly affects the O_2 reactivity, collisional activation was used to increase the z$^\bullet$-ion internal energy prior to reaction with oxygen. The results of this experiment are shown in Figure 5.8 for the $z_{12}^{2+\bullet}$ ion from neurotensin.
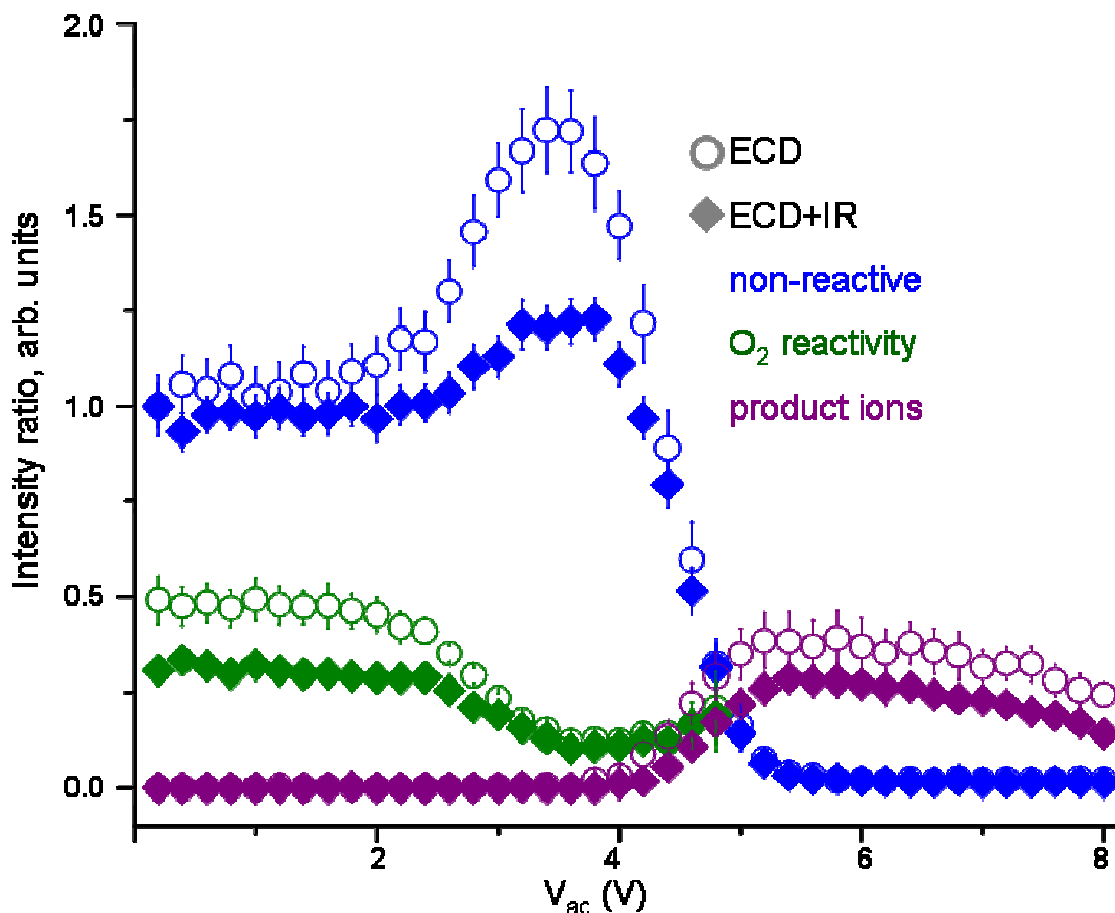
Figure 5.8 Effects of collisional activation on the non-reactive species, the O_2 reactivity, and product ion abundances of the $z_{12}^{2+\bullet}$ ion of neurotensin. The open circles represent the use of conventional ECD, and the filled diamonds represent the use of ECD+IR to form the $z_{12}^{2+\bullet}$ ion. The blue symbols represent the intensity of the non-reactive species normalized by the intensity with no collisional activation. The green symbols represent the O_2 reactivity. The purple symbols represent the intensity of the product ions formed from collisional activation normalized by the intensity of the non-reactive species with no collisional activation. These traces are plotted as a function of the supplemental ac amplitude used to collisionally activate the ion in the ECD$_{LIT}$.

The behavior of the $z_{12}^{2+\bullet}$ ion formed during ECD (hollow circles) and ECD+IR (filled diamonds) are plotted as a function of the supplemental ac voltage to induce collisional activation of the $z_{12}^{2+\bullet}$ ion. The blue symbols represent the intensities of the non-reactive z$^{\bullet}$-ion species normalized by the intensity of the non-reactive species prior to collisional activation. The intensity of the non-reactive species increased before the onset of dissociation, which occurred at approximately 4.5 V, for the $z_{12}^{2+\bullet}$ ion formed from ECD and

ECD+IR. The increase in the relative intensity of the non-reactive species was due to the decrease in the reactive species, as evidenced by the decrease in O_2 reactivity, represented by the green symbols. The O_2 reactivity for the $z_{12}^{2+\bullet}$ ion was higher when the $z_{12}^{2+\bullet}$ ion was formed during ECD compared to when it was formed during ECD+IR. This decrease in O_2 reactivity for $z^{\bullet}$-ions formed during ECD+IR was observed previously and is attributed to the increase in ion internal energy when ECD+IR was used. As the internal energy of the $z_{12}^{2+\bullet}$ ion was increased with collisional activation, the O_2 reactivity decreased for the $z_{12}^{2+\bullet}$ ion formed from both techniques, but the final O_2 reactivity was the same for each technique implying that the ions reached some common state. Because the decrease in O_2 reactivity led to an increase in the non-reactive species, it was concluded that the increase in product ion internal energy converted the $z_{12}^{2+\bullet}$ product ion from the reactive to the non-reactive species. The conversion in the relative populations of these two species was greater for the $z^{\bullet}$-ion formed during ECD because ECD produces a higher fraction of the $z^{\bullet}$-ion population as the reactive form, represented by the higher initial O_2 reactivity. The higher ion internal energy involved in ECD+IR decreased the population that is reactive to oxygen, so the addition of collisional activation had less of an effect in the conversion from the reactive to the non-reactive species. The behavior of the $z_{12}^{2+\bullet}$ product ion led to the conclusion that product ion internal energy affects the O_2 reactivity of the ions.

5.3.5 Reactive $z^{\bullet}$-ions and radical migration

The decrease in reactivity as the $z^{\bullet}$-ion internal energy was increased led to the hypothesis that radical migration to a more stable location along the peptide backbone was responsible for the decrease in O_2 reactivity. Radical migration has been shown to occur in $z^{\bullet}$-type product ions through hydrogen abstraction and often results in further backbone

cleavage [10, 13, 19]. Excess internal energy in z•-ions, provided by collisional activation, has been shown to induce radical migration resulting in the formation of smaller z•-ions [19]. It has been shown that z•-ions that are formed during ECD in a Fourier transform ion cyclotron resonance (FTICR) mass spectrometer have sufficient internal energy for radical migration [13, 17]. Due to the low operating pressures in a FTICR, there are fewer collisions between ions and neutral molecules to remove excess ion internal energy. In a LIT, the collisional cooling due to the high bath gas pressure removes the excess ion internal energy at a faster rate than radical migration. Additional internal energy provided through IR or collisional activation is sufficient for radical migration to a more stable position along the peptide backbone.

There are many possible locations in the z•-ion that would provide a more stable environment for the radical. An example of a more stable location is beta to an aromatic group where the radical can be stabilized through conjugation [27]. Another option is for the radical to migrate from the N-terminal alpha-carbon to a different alpha-carbon which is adjacent to an electron donating group (amide nitrogen) and electron withdrawing group (protonated carbonyl). The electron donating group and electron withdrawing group create stabilization through the captodative effect [27]. A third option is for the radical to migrate to a charge site where it is no longer reactive to oxygen because molecular oxygen reacts only with distonic radicals [9]. While the exact location of the stabilized radical in the z•-ion is unknown, the multiple alternative locations along the peptide backbone suggests that radical migration is responsible for the decrease of the reactivity of the z•-ions.

111

5.4 Summary and conclusions

In these experiments, the O_2 reactivity of z$^\bullet$-type product ions formed during different electron capture techniques was studied to determine reactivity of the z$^\bullet$-ion dependence on ion internal energy. A qualitative potential energy diagram was constructed to describe the ion internal energy for the different dissociation techniques used and to explain the dichotomous behavior of the z$^\bullet$-type ions (Figure 5.9). The data have shown that there are two types z$^\bullet$-ion structures which can be divided into the broad categories of reactive and non-reactive species. The two species of z$^\bullet$-ions are represented by the two potential wells in Figure 5.9. In these experiments, conversion between these two species was only observed from the reactive z$^\bullet$-ion to the non-reactive z$^\bullet$-ion. Thus, the non-reactive z$^\bullet$-ion is concluded to be energetically more stable than the reactive z$^\bullet$-ion. The conversion from the reactive z$^\bullet$-ion to the non-reactive z$^\bullet$-ion required collisional activation to increase the ion internal energy. Therefore, there must be an activation barrier limiting isomerization between these two species of z$^\bullet$-ions.

The O_2 reactivity was dependent on the dissociation technique used to produce z$^\bullet$-ions. The z$^\bullet$-ions formed during ECD were the most reactive to oxygen while the z$^\bullet$-ions formed from techniques with increased ion internal energy, ECD+IR and HECD, were less reactive to oxygen. The decrease in O_2 reactivity with the increase in ion internal energy suggested that the ion internal energy determined the relative populations of the two species of z$^\bullet$-ions. Dissociation techniques that increased the ion internal energy formed a higher population of the more stable non-reactive z$^\bullet$-ions. Therefore, the dissociation techniques were ranked by ion internal energy: ECD < AI-ECD < HECD.

Sequential AI-ECD showed that product ion internal energy had a larger effect on O_2 reactivity than parent ion internal energy. The addition of collisional activation of the $z_{12}^{2+\bullet}$ product ion induced conversion from the reactive species to the non-reactive species prior to the onset of dissociation. These two experiments established that product ion internal energy determines the relative populations of these two $z^\bullet$-ion structures. According the dissociation mechanism for ECD, cleavage of the $N-C_\alpha$ bond results in the formation of a $z^\bullet$-ion with the radical located on the N-terminal alpha-carbon. With little to no excess internal energy, the radical remains at this position and is reactive to oxygen. Excess internal energy of the product ion, provided by either the dissociation technique or supplemental activation, is sufficient for radical migration to a location of higher radical stability and therefore reduced reactivity.
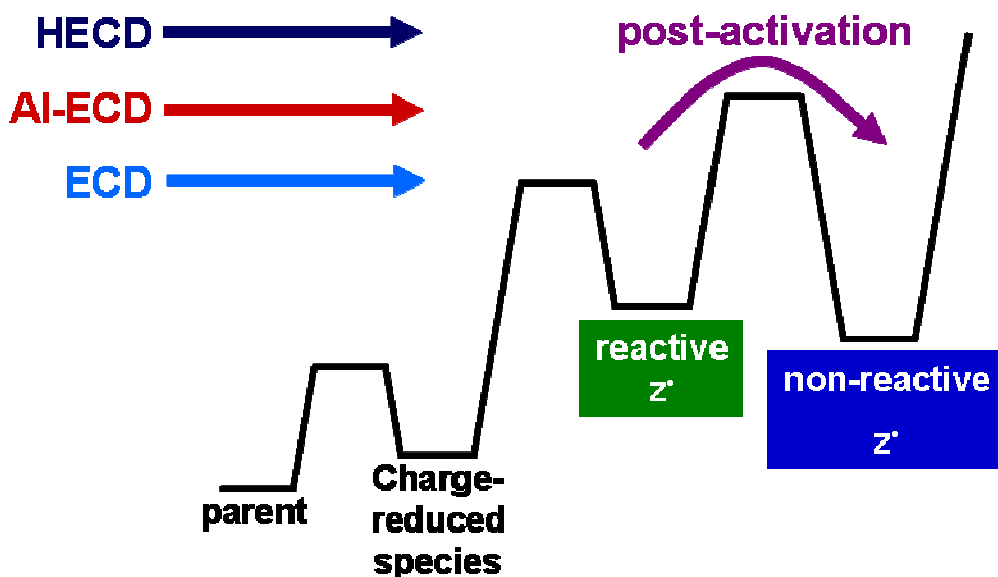

Figure 5.9 Qualitative potential energy diagram developed that in which it was observed that product ion internal energy affects O_2 reactivity of $z^\bullet$-ions.

5.5 References

1.   Zubarev, R.A., N.L. Kelleher, and F.W. McLafferty Electron Capture Dissociation of Multiply Charged Protein Cations. A Nonergodic Process. *J. Am. Chem. Soc.* **1998,** *120,* 3265-3266.

2.   Zubarev, R.A., K.F. Haselmann, B. Budnik, F. Kjeldsen, and F. Jensen Towards an Understanding of the Mechanism of Electron-Capture Dissociation: A Historical Perspective and Modern Ideas. *European Journal of Mass Spectrometry.* **2002,** *8,* 337-349.

3.   Zubarev, R.A. Reactions of Polypeptide Ions with Electrons in the Gas Phase. *Mass Spectrometry Reviews.* **2003,** *22,* 57 - 77.

4.   Cooper, H.J., K. Hakansson, and A.G. Marshall The Role of Electron Capture Dissociation in Biomolecular Analysis. *Mass Spectrometry Reviews.* **2005,** *24,* 201 - 222.

5.   Liu, J., X. Liang, and S.A. McLuckey On the Value of Knowing a z˙ Ion for What It Is. *Journal of Proteome Research.* **2008,** *7,* 130-137.

6.   Finlayson-Pitts, B.J. and J.N. Pitts Jr., *Atmospheric Chemistry: Fundamentals and Experimental Techniques.* 1986: Wiley & Sons.

7.   Xia, Y., P.A. Chrisman, S.J. Pitteri, D.E. Erickson, and S.A. McLuckey Ion/Molecule Reactions of Cation Radicals Formed from Protonated Polypeptides via Gas-Phase Ion/Ion Electron Transfer. *J. Am. Chem. Soc.* **2006,** *128,* 11792-11798.

8.   Baba, T., T. Greene, and G.L. Glish. *Electron Capture Dissociation de novo sequencing by C- and Z- terminal fragment discrimination using neutral-radical reaction.* in *57th ASMS Conference on Mass Spectrometry and Allied Topics.* 2009. Philadelphia, Pa.

9.   Moore, B.N., S.J. Blanksby, and R.R. Julian Ion-molecule reactions reveal facile radical migration in peptides. *Chem. Commun.* **2009,** 5015-5017.

10.   Li, X.J., C. Lin, L. Han, C.E. Costello, and P.B. O'Connor Charge Remote Fragmentation in Electron Capture and Electron Transfer Dissociation. *J. Am. Soc. Mass Spectrom.* **2010,** *21,* 646-656.

11.   Zhang, L.Y. and J.P. Reilly Radical-Driven Dissociation of Odd-Electron Peptide Radical Ions Produced in 157 nm Photodissociation. *J. Am. Soc. Mass Spectrom.* **2009,** *20,* 1378-1390.

12.   Kjeldsen, F., K.F. Haselmann, B.A. Budnik, F. Jensen, and R.A. Zubarev Dissociative capture of hot (3-13 eV) electrons by polypeptide polycations: an efficient process accompanied by secondary fragmentation. *Chem. Phys. Lett.* **2002,** *356,* 201-206.

13.   Leymarie, N., C.E. Costello, and P.B. O'Connor Electron Capture Dissociation
        Initiates a Free Radical Reaction Cascade. *J. Am. Chem. Soc.* **2003,** *125,* 8949 - 8958.

14.   Simons, J. Mechanisms for S-S and N-C-alpha bond cleavage in peptide ECD and
        ETD mass spectrometry. *Chem. Phys. Lett.* **2010,** *484,* 81-95.

15.   Sohn, C.H., C.K. Chung, S. Yin, P. Ramachandran, J.A. Loo, and J.L. Beauchamp
        Probing the Mechanism of Electron Capture and Electron Transfer Dissociation
        Using Tags with Variable Electron Affinity. *J. Am. Chem. Soc.* **2009,** *131,* 5444-5459.

16.   Horn, D.M., Y. Ge, and F.W. McLafferty Activated Ion Electron Capture
        Dissociation for Mass Spectral Sequencing of Larger (42 kDa) Proteins. *Anal. Chem.*
        2000, *72,* 4778-4784.

17.   O'Connor, P.B., C. Lin, J.J. Cournoyer, J.L. Pittman, M. Belyayev, and B.A. Budnik
        Long-Lived Electron Capture Dissociation Product Ions Experience Radical
        Migration via Hydrogen Abstraction. *J. Am. Soc. Mass Spectrom.* **2006,** *17,* 576 - 585.

18.   Li, X.J., J.J. Cournoyer, C. Lin, and P.B. O'Connor The Effect of Fixed Charge
        Modifications on Electron Capture Dissociation. *J. Am. Soc. Mass Spectrom.* **2008,**
        19, 1514-1526.

19.   Han, H.L., Y. Xia, and S.A. McLuckey Ion trap collisional activation of c and
        z(center dot) ions formed via gas-phase ion/ion electron-transfer dissociation. *Journal
        of Proteome Research.* **2007,** *6,* 3062-3069.

20.   Ly, T. and R.R. Julian Elucidating the Tertiary Structure of Protein Ions in Vacuo
        with Site Specific Photoinitiated Radical Reactions. *J. Am. Chem. Soc.* **2010,** *132,*
        8602-8609.

21.   Kruger, N.A., R.A. Zubarev, D.M. Horn, and F.W. McLafferty Electron Capture
        Dissociation of Multiply Charged Peptide Cations. *Int. J. Mass Spectrom.* **1999,**
        185/186/187, 787-793.

22.   Satake, H., H. Hasegawa, A. Hirabayashi, Y. Hashimoto, and T. Baba Fast Multiple
        Electron Capture Dissociation in a Linear Radio Frequency Quadrupole Ion Trap.
        Anal. Chem. **2007,** *79,* 8755-8761.

23.   Black, D.M., A.H. Payne, and G.L. Glish Determination of Cooling Rates in a
        Quadrupole Ion Trap. *J. Am. Soc. Mass Spectrom.* **2006,** *17,* 932-938.

24.   Moore, J.H., C.C. Davis, and M.A. Coplan, *Building Scientific Apparatus, 4 ed*, ed.
        A.B. Progam. 2009, Boulder, Co: Westview Press.

25.   Cooks, R.G., J.H. Beynon, R.M. Caprioli, and G.R. Lester, *Metastable Ions*. 1973,
        Amsterdam: Elsevier Scientific Publishing Company.

26.   Drahos, L. and K. Vekey MassKinetics: a theoretical model of mass spectra incorporating physical processes, reaction kinetics and mathematical descriptions. *Journal of Mass Spectrometry*. **2001,** *36,* 237-263.

27.   Hopkinson, A.C. Radical Cations of Amino Acids and Peptides: Structures and Stabilities. *Mass Spectrometry Reviews*. **2009,** *28,* 655-671.

Chapter 6

Conclusions and Future Directions

6.1 Summary and conclusions

The work presented in this dissertation demonstrates the applicability of activated-ion

electron capture dissociation (AI-ECD) for the analysis of gas-phase protein structure.

AI-ECD was used to study the primary, secondary, and tertiary structure of ubiquitin. It was

shown that the incorporation of IR activation both sequentially to and simultaneously with

electron capture dissociation (ECD) increased the formation of the c'-type and $z^\bullet$-type

product ions typical to ECD. Simultaneous AI-ECD (ECD+IR) proved to be the most

efficient use of IR activation yielding the greatest increase in sequence coverage compared

with ECD. ECD+IR also proved useful in the determination of charge sites along the protein

backbone. The c'-/$z^\bullet$-type product ion distribution was used to determine charge sites of

multiple charge state ions of ubiquitin and also to predict the sites of electron capture.

Sequential AI-ECD, in particular the use of IR activation prior to electron irradiation

(IR/ECD), was used to explain the increases in product ion formation that were observed

with AI-ECD. IR/ECD revealed that the incorporation of IR activation induced structural

unfolding of the C-terminus of ubiquitin.

Finally, ECD, AI-ECD, and hot electron capture dissociation (HECD) were used to

study the $z^\bullet$-type product ions typical to each of these techniques. Ion activation by the

electron capture techniques was used in conjunction with the ion-molecule reaction between

radical ions and molecular oxygen to probe the reactivity of $z^\bullet$-ions. It was discovered that

the reactivity of the z$^\bullet$-ions was dependent on product ion internal energy which led to the hypothesis that increased product ion internal energy was sufficient for radical migration to a position of higher stability.

6.2 Future LIT-TOF Modifications

The work presented in this dissertation utilized a hybrid linear ion trap / time-of-flight (LIT-TOF) mass spectrometer. The LIT-TOF was modified to incorporate many different ion activation techniques, including collision induced dissociation (CID), infrared multiphoton dissociation (IRMPD), ECD, HECD, and AI-ECD. The assortment of ion activation methods makes the LIT-TOF a unique instrument for direct comparison between different ion activation techniques.

6.2.1 Temperature and pressure measurements in the ECD$_{LIT}$

As discussed in Chapter 2, the exact temperature and pressure of the LIT used for ion activation (ECD$_{LIT}$) are unknown and have been found to vary during an experiment. It was initially assumed that the temperature of the ECD$_{LIT}$ was 20°C. From this temperature, the conductance through the ECD$_{LIT}$ was calculated, and the conductance was used to determine the pressure. However, the electron source, a resistively heated filament, was shown to increase the temperature of the ECD$_{LIT}$ over a span of several hours.

The temperature of the ECD$_{LIT}$ was measured through the placement of a thermocouple at the approximate center of the ECD$_{LIT}$. The placement of the thermocouple prevented the application of the voltages used to manipulate the ions, so simultaneous protein analysis and temperature measurement cannot be performed in the ECD$_{LIT}$. Also, the pressure in the ECD$_{LIT}$ is still calculated using the conductance formula and the measured temperature. The incorporation of a permanent thermocouple and pressure gauge would

118

allow direct measurements of temperature and pressure during an experiment. Due to spatial restrictions and aluminum vacuum housing, the configuration for constant temperature and pressure measurements has not yet been implemented.

6.2.2 Comparison of ion activation methods: ETD and ECD

In the literature, ECD and electron transfer dissociation (ETD) are often compared and considered to dissociate by the same mechanism with similar energetics [1-3]. However, there has been no direct comparison between ECD and ETD using the same instrument. The lack of direct comparison between ECD and ETD is a result of the instruments typically used to carry out these experiments: ECD is commonly performed in a Fourier transform ion cyclotron resonance (FTICR) mass spectrometer; ETD was developed for use in ion traps. Modification of the LIT-TOF to include ETD as an ion activation method would yield the first instrument that can provide direct comparison between ETD and ECD.

To effect ETD in the LIT-TOF, a number of modifications must be implemented. The ECD_{LIT} must be modified to trap ions of opposite polarities at the same time for the electron transfer reaction. To trap both positive and negative ions, a low amplitude rf voltage is applied to the end lenses of the ECD_{LIT}. As electrons are not used in ETD, the addition of a rf voltage along the z-axis of the ECD_{LIT}, which would result in increased electron kinetic energy in ECD, is not an issue. A negative ion source for the production of the reagent anions must be added to the source region of the LIT-TOF. A negative chemical ion source is commonly used, but negative mode electrospray ionization can also be used. As positive and negative ions are generated from the same source region, the ion optics that guide the ions to the ECD_{LIT} need to be able to switch between positive and negative ion transmission.

With these modifications, the LIT-TOF can be used for the first direct comparison between each of the electron capture techniques.

6.3 Activated-ion electron capture dissociation

The incorporation of IR activation sequentially to and simultaneously with ECD was shown to increase the sequence coverage of the protein ubiquitin. The collinear alignment of the IR photon and electron beams along the central axis of the ECD_{LIT} ensured efficient overlap between ions, electrons, and photons. The alignment of the IR and electron beams resulted in an increase in electron flux due to heating of the tungsten filament by the IR laser. The benefits of ECD+IR were shown to be the result of IR-induced protein unfolding and not increased electron flux.

6.3.1 Large protein analysis

AI-ECD was developed for the analysis of large proteins with extensive noncovalent interaction networks [4-6]. For the work in this dissertation, AI-ECD was used to analyze ubiquitin ions of multiple charge states. Ubiquitin was chosen because of its extensive characterization by ECD and AI-ECD in FTICR mass spectrometers [7-11]. However, ubiquitin is a relatively small protein (~8.6 kDa) and may not provide the best model for AI-ECD. The analysis of larger proteins, such as cytochrome *c* and carbonic anhydrase, by AI-ECD would be beneficial to provide comparison between AI-ECD in the LIT-TOF and a FTICR. The effects of IR activation would be expected to be greater for the larger proteins due to the increase in noncovalent interactions, as ECD of these proteins provides little sequence information [4, 12].

Aside from the analysis of larger proteins, the structure of the protein must be considered. Thus far, proteins have been sampled from solutions with high organic content

(~50 %) which has been shown to induce unfolding to a helical state in solution. The

denatured helical structure is due to the destabilization of tertiary structure and the

stabilization of helices in alcoholic solutions [13]. As an alternative, an aqueous ammonium

acetate buffer at physiological pH has been shown to preserve noncovalent interactions of

large macromolecular complexes upon desolvation implying retention of a more native-like

conformation [14]. It has also been shown that the addition of ammonium acetate salt to the

spraying solution does not increase the charge state distribution of protein ions, which is an

indicator of structural unfolding, compared with purely aqueous solution [15]. It is expected

that IR activation in AI-ECD of protein ions formed from aqueous ammonium acetate buffer

solutions would have a greater effect in product ion formation. The protein ions from

aqueous solutions with more native conformations have more extensive noncovalent

interactions. Therefore, conventional ECD would be less effective, and the disruption of

noncovalent interactions by IR activation would be of higher importance in sequencing these

proteins.

6.3.2 Incorporation with liquid chromatography

ECD+IR has been shown to increase the formation of product ions compared to ECD

without a subsequent increase in activation time. Thus, ECD+IR can be implemented in lieu

of ECD with liquid chromatography (LC) for protein digest analysis [16, 17]. It is expected

that the method for protein digestion would need to be studied. Typically, the enzyme

trypsin is used for protein digestion followed by LC-MS/MS analysis. Trypsin, which

cleaves C-terminal to the basic residues lysine and arginine, forms small (average 9.6

residues [18]) peptides which are typically dications in the gas phase (charge located on the

C-terminal basic residue and the N-terminus). While ECD can be used in the analysis of

dications, it is much more effective for highly charged ions. ECD of highly charged ions

(n>3) often results in charges on both product ions which aids in product ion separation after

backbone cleavage [19]. The advantages of ECD of highly charged ions implies that a

digestion method that yields longer multiply charged peptides, such as microwave

D-cleavage [18] or protein digestion by the enzyme Asp-N [20], would be more appropriate

for AI-ECD analysis of protein digests.

6.4 Gas-phase protein unfolding

The increase in product ion formation with the incorporation of IR activation with

ECD was explained by the unfolding of the C-terminus of ubiquitin. Analysis of the product

ion distribution from IR/ECD at various IR activation times revealed the structural unfolding

of ubiquitin due to the disruption of noncovalent interactions. The gas-phase structure of

ubiquitin was also analyzed by ECD+IR. The charge state and distribution of the product

ions allowed determination of the charge sites in multiple ubiquitin ions and led to the

prediction that electron capture occurred at each charge site.

6.4.1 Gas-phase unfolding and refolding

As mentioned previously, the protein solutions used in these experiments contained

high amount of organic solvent which is known to induce protein unfolding. The use of

aqueous ammonium acetate buffer as the protein solvent would result in a more native-like

gas-phase protein structure. IR/ECD of protein ions produced from these physiological

solvent conditions would provide insight into solution- and gas-phase protein structure.

IR activation prior to electron irradiation was used to monitor protein unfolding in the

gas phase. For these experiments, the sequential AI-ECD experiments were performed

without a delay period in between the two activation steps. The incorporation of a delay

period between IR and electron irradiation would result in collisional cooling of the protein with the bath gas resulting in a loss of the protein ion excess internal energy. A consequence of the decrease in ion internal energy is refolding of the gas-phase protein. Pulsed IR-delay-ECD experiments have shown that gas-phase refolding occurs on the millisecond timescale [7, 12, 21]. An extensive study with various IR activation and delay times would provide kinetic information on the gas-phase unfolding and refolding of proteins. Also, analysis of the product ion distribution for the folded and refolded structures could reveal structural differences that occur upon gas-phase annealing.

6.4.2 Prediction of electron capture sites

In Chapter 4, the sites of electron capture were predicted based on the clusters of product ions near charge sites. It was previously shown that the protein backbone is preferentially cleaved N-terminal to the electron capture site [7]. The ECD+IR results showed clusters of ions on either side of the predicted electron capture site. Also, not every product ion could be explained by electron capture at a nearby charge site indicating that through-space radical migration may have occurred. To confirm electron capture locations, it would be best to initially study small peptides, for example tryptic peptides, prior to full protein analysis. Using smaller peptides with fewer charge states would make it easier to evaluate electron capture. A previous study revealed that electron capture preferentially occurred at the N-terminus of tryptic peptides [22]. The observation of the preferential electron capture site led to the conclusion that electron capture is more likely to occur at charged sites with the lowest proton affinity. The results from ECD+IR showed that electron capture occurs at all charge sites with no indication of preference for a single charge site over

others. A systematic study of peptides with increasing charge would confirm or deny the concept of preferential electron capture.

6.5 Investigation of the z$^\bullet$-ion

The radical reactivity of the z$^\bullet$-ion was probed by reaction with molecular oxygen. It was found that the radical ion reactivity varied with the electron capture technique used (ECD > AI-ECD > HECD). It was determined that product ion internal energy was the strongest influence on radical reactivity. The inverse correlation between product ion internal energy and radical reactivity led to the hypothesis of radical migration due to excess product ion internal energy. The radical is hypothesized to migrate to a more stable location along the peptide backbone which decreases the reactivity for oxygen adduct formation.

6.5.1 ETD+O$_2$

In this study, the z$^\bullet$-ions formed during ECD, AI-ECD, and HECD were analyzed. The analysis of z$^\bullet$-ions formed during ETD would increase the understanding of the energetics of electron capture techniques. The internal energy of ions after electron transfer is predicted to be lower than that for electron capture because of the electron affinity of the anion donor [2, 3, 23]. Also, z$^\bullet$-ions formed during ETD have been shown to be very reactive with molecular oxygen [24]. Based on the relative decrease in ion internal energy and previous analysis of ETD+O$_2$, it is expected that the z$^\bullet$-ions formed during ETD would have high O$_2$ reactivity.

6.5.2 Model peptides for radical stabilization

It has been shown that the radical reactivity decreases with increased product ion internal energy, and it is hypothesized that radical migration to a more stable location causes the decrease in reactivity. However, the position of the stabilized radical is still unknown. It

has been shown that the alpha-carbons along the peptide backbone are equivalent in terms of radical stability [25]. Radical stabilization can also come from conjugation with an aromatic group [26]. The $z_{12}^{2+\bullet}$ ion from the peptide neurotensin (pELYENKPRRPYIL) was used in this study. As can be inferred from the sequence, there is a tyrosine located two residues away from the site of radical formation. It is hypothesized that radical stability is achieved via stabilization with the aromatic side-chain of tyrosine (Y). To test this hypothesis, the peptides AAR, YAR, and AYR were synthesized but have not been studied. Comparison of the O_2 reactivity of the $z_2^{+\bullet}$ ions would reveal if the radical is stabilized by migration to the beta position of the aromatic side-chain.

6.5.3 Theoretical evidence for radical migration and stabilization

The addition of structural calculations of radical cations would bolster the hypothesis of radical migration and stabilization. We currently have a collaboration with Dr. Takeuchi at Nara Women's University to carry out these calculations. It is predicted that the radical from backbone cleavage is stabilized by conjugation with the carbonyl double bond. Calculations have shown that radical stability is enhanced by positioning between an electron donating and electron withdrawing group [26]. Based on stabilization of the radical by both an electron donating and electron withdrawing group, radical migration away from the N-terminal alpha-carbon is expected.

6.6 References

1.   Mentinova, M., D.M. Crizer, T. Baba, W.M. McGee, G.L. Glish, and S.A. McLuckey Investigating the Role of Cation Recombination Energy/Coulomb Repulsion in ETD/ECD. *in preparation*.

2.   Li, X.J., C. Lin, L. Han, C.E. Costello, and P.B. O'Connor Charge Remote Fragmentation in Electron Capture and Electron Transfer Dissociation. *J. Am. Soc. Mass Spectrom.* **2010,** *21,* 646-656.

3.   Sohn, C.H., C.K. Chung, S. Yin, P. Ramachandran, J.A. Loo, and J.L. Beauchamp Probing the Mechanism of Electron Capture and Electron Transfer Dissociation Using Tags with Variable Electron Affinity. *J. Am. Chem. Soc.* **2009,** *131,* 5444-5459.

4.   Horn, D.M., Y. Ge, and F.W. McLafferty Activated Ion Electron Capture Dissociation for Mass Spectral Sequencing of Larger (42 kDa) Proteins. *Anal. Chem.* **2000,** *72,* 4778-4784.

5.   Sze, S.K., Y. Ge, H. Oh, and F. McLafferty Top-down mass spectrometry of a 29 kDa protein for characterization of any posttranslational modification to within one residue. *PNAS*. **2002,** *99,* 1774-1779.

6.   Sze, S.K., Y. Ge, H.B. Oh, and F.W. McLafferty Plasma Electron Capture Dissociation for the Characterization of Large Proteins by Top Down Mass Spectrometry. *Anal. Chem.* **2003,** *75,* 1599 - 1603.

7.   Breuker, K., H. Oh, D.M. Horn, B.A. Cerda, and F.W. McLafferty Detailed Unfolding and Folding of Gaseous Ubiquitin Ions Characterized by Electron Capture Dissociation. *J. Am. Chem. Soc.* **2002,** *124,* 6407-6420.

8.   Oh, H., K. Breuker, S.K. Sze, Y. Ge, B.K. Carpenter, and F.W. McLafferty Secondary and tertiary structures of gaseous protein ions characterized by electron capture dissociation mass spectrometry and photofragment spectroscopy. *PNAS*. **2002,** *99,* 15863-15868.

9.   Breuker, K., H. Oh, C. Lin, B.K. Carpenter, and F.W. McLafferty Nonergodic and Conformational Control of the Electron Capture Dissociation of Protein Cations. *PNAS*. **2004,** *101,* 14011-14016.

10.   Robinson, E.W., R.D. Leib, and E.R. Williams The Role of Conformation on Electron Capture Dissociation of Ubiquitin. *J. Am. Soc. Mass Spectrom.* **2006,** *17,* 1470 - 1480.

11.   Pan, J., J. Han, C.H. Borchers, and L. Konermann Electron Capture Dissociation of Electrosprayed Protein Ions for Spatially Resolved Hydrogen Exchange Measurements. *J. Am. Chem. Soc.* **2008,** *130,* 11574-11575.

12. Horn, D.M., K. Breuker, A.J. Frank, and F.W. McLafferty Kinetic Intermediates in the Folding of Gaseous Protein Ions Characterized by Electron Capture Dissociation Mass Spectrometry. *J. Am. Chem. Soc.* **2001,** *123,* 9792-9799.

13. Babu, K.R., A. Moradian, and D.J. Douglas The Methanol-Induced Conformational Transitions of B-lactoglobulin, Cytochrome C, and Ubiquitin at Low pH: A Study by Electrospray Ionization Mass Spectrometry. *J. Am. Soc. Mass Spectrom.* **2001,** *12,* 317-328.

14. Heck, A.J.R. and R.H.H. van den Heuvel Investigation of intact protein complexes by mass spectrometry. *Mass Spectrometry Reviews.* **2004,** *23,* 368-389.

15. Prakash, H., B.T. Kansara, and S. Mazumdar Effects of salts on the charge-state distribution and the structural basis of the most-intense charge-state of the gaseous protein ions produced by electrospray ionization. *Int. J. Mass Spectrom.* **2010,** *289,* 84-91.

16. Cooper, H.J., K. Hakansson, and A.G. Marshall The Role of Electron Capture Dissociation in Biomolecular Analysis. *Mass Spectrometry Reviews.* **2005,** *24,* 201 - 222.

17. Palmblad, M., Y.O. Tsybin, M. Ramstrom, J. Bergquist, and P. Hakansson Liquid Chromatography and electron-capture dissociation in fourier transform ion cyclon resonance mass spectrometry. *Rapid Commun. Mass Spectrom.* **2002,** *16,* 988-992.

18. Hauser, N.J., H.L. Han, S.A. McLuckey, and F. Basile Electron transfer dissociation of peptides generated by microwave D-cleavage digestion of proteins. *Journal of Proteome Research.* **2008,** *7,* 1867-1872.

19. Rand, K.D., C.M. Adams, R.A. Zubarev, and T.J.D. Jorgensen Electron Capture Dissociation Proceeds with a Low Degree of Intramolecular Migration of Peptide Amide Hydrogens. *J. Am. Chem. Soc.* **2008,** *130,* 1341 - 1349.

20. Kellner, R., F. Lottspeich, and H.E. Meyer, *Microcharacterization of Proteins, Second edition ed.* 1999, Weinheim: Wiley-VCH.

21. Bushey, J.M., *Improvements in Electrospray Ionization Source Design and Advances in Tandem Mass Spectrometry*, in *Chemistry*. 2008, University of North Carolina: Chapel Hill. p. 186.

22. Kjeldsen, F., M.M. Savitski, C.M. Adams, and R.A. Zubarev Determination of the location of positive charges in gas-phase polypeptide polycations by tandem mass spectrometry. *Int. J. Mass Spectrom.* **2006,** *252,* 204-212.

23. Simons, J. Mechanisms for S-S and N-C-alpha bond cleavage in peptide ECD and ETD mass spectrometry. *Chem. Phys. Lett.* **2010,** *484,* 81-95.

24.   Xia, Y., P.A. Chrisman, S.J. Pitteri, D.E. Erickson, and S.A. McLuckey Ion/Molecule Reactions of Cation Radicals Formed from Protonated Polypeptides via Gas-Phase Ion/Ion Electron Transfer. *J. Am. Chem. Soc.* **2006,** *128,* 11792-11798.

25.   Leymarie, N., C.E. Costello, and P.B. O'Connor Electron Capture Dissociation Initiates a Free Radical Reaction Cascade. *J. Am. Chem. Soc.* **2003,** *125,* 8949 - 8958.

26.   Hopkinson, A.C. Radical Cations of Amino Acids and Peptides: Structures and Stabilities. *Mass Spectrometry Reviews.* **2009,** *28,* 655-671.